Design, Fabrication and Characterization of Metamaterials for Slow Wave Devices in the MHz and GHz regimes

Ioannis Spanos

St. Edmund Hall College



A thesis submitted for the degree of Doctor of Philosophy

University of Oxford

Department of Engineering Science

Supervisors:

Prof. Chris Stevens and Prof. Ekaterina Shamonina

Abstract

This thesis investigates the coupling mechanisms and dispersion characteristics of discrete and coalesced resonators operating in the MHz and GHz regimes. We employ an analytic model taking into account both magnetic and electric couplings between resonators, aiming to develop novel ways of dispersion control. The study places particular emphasis on the fabrication aspect, with the development of a novel method based on liquid metal injection which was used for the realization of 3D resonant structures. The resonators studied can communicate using their magnetic fields via the law of induction; a time-varying current in one, induces a current in another. In an array of resonators, the induced currents propagate along the line like waves. These waves have been named magnetoinductive waves due to the magnetic coupling between elements.

The coupling mechanisms are analyzed in two planar scenarios; a discrete arrangement, where the resonators are in close proximity but not in contact, and a coalesced arrangement, where the resonators are touching and sharing one side. While arrangements of discrete resonators have been extensively studied, configurations of coalesced resonators have been overlooked in the literature. Arrays of resonators with one, three and four gaps are considered. While the resonators are not in contact (discrete case), it is found that the number of gaps has no effect on the total coupling coefficient, which is negative. The main contribution comes from the magnetic coupling while the electric coupling coefficient is near zero. When the resonators are connected so that they share one side (coalesced case), it is shown that the coupling coefficient can change drastically depending on the number of gaps. In particular, when the shared side is capacitively loaded, the total coupling coefficient switches to positive values, allowing for forward waves to propagate on the structure. This change is due to the electric coupling increasing in magnitude, as shown from the analytic model used to extract the magnetic and electric coupling coefficients. Based on these findings, an optimisation procedure for setting up numerical simulations to match the experimental data is proposed. This approach aims to reduce computational resource requirements while ensuring the reliability of the simulations. The simulations provided significant insight on the electric coupling's be-

haviour, which was crucial in the development of a tunable capacitor metamaterial array for dispersion control.

Despite recent advances in additive manufacturing, the fabrication of truly 3D conductive structures still remains a challenge. To address this issue, a novel method based on liquid metal injection is proposed. During the process, dielectric moulds with hollow paths are created using a 3D printer. Subsequently, the paths are injected with liquid Field's metal, a metal alloy which solidifies at room temperature. The metal fills the paths and conforms to their shape, allowing for the realisation of 3D conductive structures inside a dielectric medium. The method shows great potential to be incorporated into standard 3D printing setups, as the filling process can be performed using a custom-made Field's metal filament loaded on a commercially available 3D pen. Initial characterization of the method involves determining the minimum feature size of paths that can be achieved on our setup and conducting resistance measurements of filled tracks. The value of 3.6 MS/m is, to the best of our knowledge, the most reliable measurement for Field's metal conductivity in the literature. Using this method, square and spiral resonators are fabricated. Even though the square resonators exhibit higher losses compared to similar geometries made with conventional methods such as printed circuit board, the spiral resonators demonstrate exceptionally high quality factors. It is shown that the operating frequency and quality factor of the spirals can be tuned by adjusting the number of turns. After testing various dielectric materials for their suitability and electromagnetic properties, the study reveals that the most favourable material for use in Field's metal fabrication is high impact polystyrene. Using the spiral resonators, a 3D metamaterial cube is constructed and the different couplings present in the structure are investigated. Field's metal fabrication paves the path for the creation of 3D circuits, allowing the miniaturization of devices. This is demonstrated with the fabrication of a thermometer circuit.

The work presented in this thesis further explores the physics behind coupled resonators and wave propagation of magnetoinductive waves, while carrying important technological implications with the development of a novel method for 3D conductive structures.

Acknowledgements

I would like to express my gratitude to a number of people:

My supervisors, Prof. Chris Stevens and Prof. Ekaterina Shamonina for their continuous guidance throughout my DPhil. Chris' resourcefulness was a key factor in troubleshooting many obstacles I encountered. Our brainstorming sessions provided with the thought process on how to connect my scientific results with real world applications. Katya's methodical mindset taught me how to approach problems as a scientist. She helped me cultivate a structured thought process as my research was evolving. I feel grateful to both of them for their immense support throughout the COVID pandemic which plagued my DPhil.

Members of our "Metamaterials" group such as Dr. Andrea Vallecchi and Dr. Anya Radkovskaya who helped me get familiarised with setting up experiments and numerical simulations. Prof. Laszlo Solymar provided helpful insights in the results of my work. My fellow DPhil students Kailun Xu, Joshua Feis and Georgiana Dima who were willing to offer their assistance whenever a problem presented itself.

Dr. Maria Farsari and the "Nonlinear Lithography" group in IESL, FORTH, who welcomed me in their group, allowing me to use their lab facilities when I was in Greece during COVID. They also allowed me to use their office space when I moved out of Oxford which made writing my thesis a very pleasant experience.

Other members of the department such as Grahame Faulkner who was an immense help in pretty much anything, including safety matters and equipment orders. Dr. James Farmer and Dr. Andy Schreier for their willingness to offer their help to any issues that emerged.

Our collaborators in Loughborough University. Prof. Yiannis Vardaxoglou and Prof. William Whittow for the many fruitful discussions. Dr. Jack McGhee, Dr. Thanos Goulas and Dr. Thomas Whittaker who provided with expert advice on all 3D printing matters.

My majestic housemates, Aleksei, Lucy, Lizzy, Marie-Claire and Thijs, whose mere presence made the Oxford experience worthwhile. You made a simple house our warm home and I will never forget the times we shared. The only problem is that you raised the bar to unrealistic standards for any future housemates and I am already missing the home-baked cake on

my birthday.

Finally my parents, Stella and Lefteris, who supported me any way they could. Even though this DPhil was a personal pursuit, I hope it makes you proud as well.

Some of the work presented in this thesis also forms part of the following publications:

Journals

- C. J. Stevens, I. Spanos, A. Vallechi, J. McGhee, W. Whittow, "3D printing of functional metal and dielectric composite meta-atoms", *Small*, vol. 18, p. 2105368, (2022).
- I. Spanos, C. J. Stevens, L. Solymar, E. Shamonina, "Tailoring the dispersion characteristics in planar arrays of discrete and coalesced split ring resonators", *Sci. Rep.*, vol. 13, p. 19981, (2023).
- I. Spanos, C. J. Stevens, L. Solymar, E. Shamonina, "Tunable capacitor arrays of coalesced resonators for dispersion control", *EPJ AM*, (accepted, 2023).

Conferences

- I. Spanos, C. J. Stevens, A. Vallechi, J. McGhee, W. Whittow, "Fabricating 3D metamaterials via Field's metal injection", *21st Microwave Mediterranean Symposium (MMS)*, Pizzo Calabro, Italy, p. 1, (2022, oral).
- I. Spanos, C. J. Stevens, A. Vallechi, J. McGhee, W. Whittow, "2D magnetoinductive waveguide fabricated using molten Field's metal", *16th International Congress on Artificial Materials for Novel Wave Phenomena (Metamaterials)*, Siena, Italy, p. X-419, (2022, oral).
- I. Spanos, C. J. Stevens, L. Solymar, E. Shamonina, "Tunable dispersion in planar arrays of coalesced resonators", *17th International Congress on Artificial Materials for Novel Wave Phenomena (Metamaterials)*, Chania, Greece, (2023, oral).
- I. Spanos, C. J. Stevens, "Additive manufacturing of 3D electromagnetic metamaterials and chips via liquid metal injection", *10th International Conference on Micro-Nanoelectronics, Micro-Nanosciences & Nanotechnologies*, Athens, Greece, (2023, poster).

In addition, the following publications were published during my DPhil but lie outside the scope my thesis:

- Z. Vangelatos, K. Komvopoulos, I. Spanos, M. Farsari, C. Grigoropoulos, "Anisotropic and curved lattice members enhance the structural integrity and mechanical performance of architected metamaterials", *Int. J. Solids Struct.*, vol. 193, p. 287, (2020).

- G. Flamourakis, I. Spanos, Z. Vangelatos, P. Manganas, L. Papadimitriou, C. Grigoropoulos, A. Ranella, M. Farsari, "Laser-made 3D auxetic metamaterial scaffolds for tissue engineering applications", *Macromol. Mater. Eng.*, vol. 305, p. 2000238, (2020).

- I. Spanos, Z. Vangelatos, C. Grigoropoulos, M. Farsari, "Design and characterization of microscale auxetic and anisotropic structures fabricated by multiphoton lithography", *Nanomater.*, vol. 11, p. 446, (2021).

- I. Katsantonis, M. Manousidaki, A. D. Koulouklidis, C. Daskalaki, I. Spanos, C. Kerantzopoulos, A. C. Tasolamprou, C. M. Soukoulis, E. N. Economou, S. Tzortzakis, M. Farsari, M. Kafesaki, " Strong and broadband pure optical activity in 3D printed THz chiral metamaterials", *Adv. Optical Mater.*, vol. 11, p. 2300238, (2023).

- A. D. Koulouklidis, I. Katsantonis, M. Manousidaki, A. C. Tasolamprou, C. Daskalaki, C. Kerantzopoulos, I. Spanos, S. Tzortzakis, M. Farsari, M. Kafesaki, "Achieving large and broadband THz optical activity via 3D chiral metamaterials", *The European Conference on Lasers and Electro-Optics (CLEO)*, Munich, Germany, (2023).

Contents

1 Introduction **1**

2 Circuit theory description of split ring resonators **11**

2.1 Single resonator 12

2.2 Two resonators 12

2.3 Array of resonators 18

2.4 Impedance matrix 20

3 Numerical setup **23**

3.1 Replicating the experimental setup 24

3.2 Simulation parameters 31

4 Discrete and coalesced resonators **35**

4.1 Experimental methods and sample preparation 36

4.2 100 pF resonators 37

4.2.1 Unit cells 37

4.2.2 Dimers 39

4.2.3 Arrays 45

4.2.4 Variable capacitors 48

4.3 Higher frequencies 51

4.3.1 Unit cells 52

4.3.2 Dimers 55

4.3.3 Arrays 57

5 Field's metal fabrication **63**

5.1 Materials 64

5.2 Fabrication methods 66

5.2.1 3D printer 66

5.2.2 Heated water bath approach 66

5.2.3 3D pen approach 67
5.3 Fabrication characterization 69
5.3.1 Fabrication resolution 69
5.3.2 Electrical isolation 71
5.3.3 Resistance and conductivity 72
5.4 Coalesced SRRs 75
5.5 Spiral resonators 77
5.5.1 Tunability of the resonance 78
5.5.2 Coupling coefficients 82
5.5.3 Spiral cube 86
5.6 3D circuits 93

6 Conclusions and future work **99**

Appendix A: Higher frequencies results **107**

Bibliography

Chapter 1
Introduction

The first part of Chapter 1 provides an introduction to metamaterials, leading to an overview of magnetoinductive waves, the main topic of this thesis. Magnetoinductive waves are slow waves that can propagate on arrays of split ring resonators due to the magnetic coupling between them. Even though split ring resonators have been studied in various arrangements, limited reports exist when the resonators are in direct contact with each other. Investigating these structures and understanding their coupling mechanisms, will allow for novel ways of dispersion control. In the second part of Chapter 1, the challenge of fabricating 3D conductive structures is explored. Various emerging technologies are discussed, with an emphasis on fused deposition modelling. A novel method based on liquid metal injection of Field's metal inside 3D printed moulds is presented. While the primary focus of Chapter 1 is to present an overview on the research areas relevant to this thesis, it also highlights the sections of the literature that each of the following chapters will be addressing.

Metamaterials is a term used to describe artificial materials with unique properties not commonly found in nature [1], [2]. These properties are not the result of chemical composition but of material architecture. Instead of having atoms or molecules composing a solid, meta-atoms are the building blocks, which are reproduced in space to create a metamaterial. These properties can be mechanical, such as negative Poisson's ratio [3], [4], vanishing shear modulus [5], [6], negative compressibility [7], [8] and negative thermal expansion [9], [10], or electromagnetic, such as negative permittivity [11], [12], negative permeability [13], [14], negative refractive index [15], [16], perfect absorbers [17], [18] and optical cloaking [19], [20].

Even though the concept of metamaterials did not exist until much later, early works can be traced back to the 20^{th} century. Analytical investigations showed that the phase and group velocities of a wave could be anti-parallel, leading to the emergence of backward waves [21], [22]. In the second half of the century, the concepts of negative permittivity, negative permeability and their implications to refraction were studied [23], [24]. In 1968, Veselago presented the idea of "left-handed media" exhibiting negative refractive index by having both permittivity and permeability negative at the same time [25].

At that point in time, it was a well known fact that metals can have a negative permittivity, as the Drude model predicted negative values below their plasma frequency. As demonstrated in [26], [27], periodic lattices of thin wires can have a plasma frequency in the GHz range. Negative permeability on the contrary, was elusive to scientists. Even though negative permeability could be demonstrated in ferrites during their ferromagnetic resonance, it required a constant external magnetic field [28]. A more practical approach to negative permeability came with the the introduction of the split ring resonator (SRR), whose effective magnetic permeability can be tuned to have negative values [29]. By combining metallic rods with SRRs, a composite medium with simultaneous negative permittivity and permeability was demonstrated experimentally [15]. This led to a surge of research interest towards metamaterials, which saw immense growth in the coming years.

In a single SRR, a circulating current will create a magnetic field normal to the plane of the resonator. Two SRRs positioned close enough can communicate with their magnetic fields; a

time-varying current in one induces a current in the second via the law of induction. In an array of SRRs, the induced currents will propagate along the line like waves. Since the resonators are magnetically coupled to each other, these waves have been given the name magnetoinductive (MI) waves [30], [31]. MI waves have found applications in imaging [32], [33], sensing [34], [35], conductivity detection [36], wireless power transfer [37], [38] and waveguides [39], [40], among others. If the elements are electrically coupled, a similar behaviour is observed. In this case the waves are called electroinductive (EI) waves [41]–[43].

A SRR can be modelled by a circuit equivalent, having a self-inductance from the conductive part and a capacitance due to the gap [44]. The shape of the SRR can differ, but the response remains similar [45]–[47]. The element's resonance can then be described by this circuit. This approximation is quite effective when the size of the SRR is smaller than the wavelength at resonance [15], [48], [49]. Hence, a medium made of coupled SRRs can be modelled analytically [30]. Both backward and forward MI waves can be controlled via the coupling between the elements. Typically, axial arrays result in forward-wave propagation because the elements have a positive coupling coefficient, while planar arrays show backward-wave propagation because the elements have a negative coupling coefficient. In Chapter 2, the analytic circuit theory description of SRRs and MI waves is presented.

MI waves can interact with electromagnetic waves. Using an analytical model based on the periodically loaded transmission line, the interaction between electromagnetic and MI waves is presented in the form of a coupled dispersion equation [50]. The model predicts the formation of stopbands due to the waves interaction and passbands that can support both forward and backward travelling waves. These results are expanded in 2D by including effective-medium theory to the analytical model [51], showing that a periodic medium of SRRs is capable of supporting the propagation of surface waves.

The relative orientation between SRRs can affect the coupling mechanisms. Depending on how close the gaps of neighbouring SRRs are, the electric coupling can increase in magnitude [52], [53]. For the same reason, it can be expected that the number of gaps will also affect the coupling [54]. The coupling is affected by the frequency as well. In the THz regime, the

magnetic coupling weakens significantly, resulting in the electric coupling being dominant [55], [56]. At the same time, the coupling coefficients can become complex, altering the shape of the band due to retardation effects [40], [57]. For these reasons, it is crucial that the coupling coefficients can be reliably measured.

A common method of conducting measurements on arrangements of SRRs in the MHz and GHz regimes is by using two magnetic loop antennas connected to a vector network analyzer (VNA) [58]. A magnetic loop antenna excites the SRR while a second loop is used to detect the magnetic field. This method is non-destructive and does not require any additional preparation of the samples prior to measurement. It should be noted however, that the presence of the metal antennas creates eddy currents in the SRR, which changes the self inductance of the resonator to a complex value, slightly altering its resonance frequency and quality factor [53], [59].

An analytical method of measuring the complex magnetic and electric coupling coefficients from experimental or numerical data was proposed in [60]. This method builds on the work of Tatartschuk et al. [55], by fitting a line to the experimental or numerical measurements of two SRRs, whose intercept and slope allow for the extraction of the magnetic and electric coupling coefficients respectively. It also introduces two correction factors accounting for the unwanted interactions between the magnetic loop antennas and the resonators, which make the model more accurate. This analytical method is introduced in Chapter 2, and subsequently applied in Chapters 4 and 5 to extract the coupling coefficients.

Even though the magnetic and electric couplings between discrete elements has been extensively studied [61]–[63], reports on coalesced resonators have been limited. There are a few examples where coalesced SRRs for applications at optical frequencies are investigated [64]–[66]; however, the effect on the total coupling is not yet understood. The term conductive coupling was coined to describe the change in coupling due to the elements touching. In Chapter 4, it will be shown that the magnetic and electric couplings are sufficient to describe the behaviour of coalesced resonators, without the need to introduce additional coupling mechanisms.

Coalesced elements could lead to some interesting results. It has been observed that a planar array can support the propagation of forward waves if the SRRs are joined [67]. In this case, the coupling between elements appears to turn positive when the SRRs are coalesced. Using the analytic model presented in Chapter 2 and the numerical setup described in Chapter 3, this behaviour is investigated in Chapter 4.

A similar effect can be observed when the SRRs are connected via capacitive links, forming alternating major and minor loops [68], [69]. This essentially creates a diatomic chain of resonators, making it possible to tailor the dispersion depending on the capacitance between the two types of loops. Diatomic metamaterial structures have an inter-element coupling, allowing for further dispersion control, as shown in [70]. The inter-element coupling can be tuned by the orientation and relative positions of the two SRRs [71]. The large variety of potential coupling arrangements allows for the tailoring of the dispersion for particular requirements.

In two dimensions, the term "metasurface" is often used to describe a structure consisting of a single or a few layers of meta-atoms [72]. A metasurface can consist of subwavelength holes or slits [73]–[76]. Such structures demonstrate unusually high transmission of power for wavelengths larger than the period of the unit cells. In [77] the resonators of a metasurface are carefully optimized so that their electric and magnetic responses are balanced. The metasurface is shown to be capable of manipulating transmitted wave fronts while exhibiting high transparency over a broad range of frequencies. Metasurfaces of SRRs can support the propagation of magnetoinductive waves [30], which can be used for data and power transfer applications [78].

In three dimensions, 3D resonators are of particular interest. Cubic resonators have a degree of degeneration to their eigenvalues, defined by the symmetries and orientation of the SRRs it is comprised of [79], [80]. Their response can be tailored to be isotropic depending on the symmetries of the constituent SRRs. Even though 3D resonators are interesting on their own right, they can also be used as meta-atoms to construct intricate metasurfaces or metamaterials [81]. For example, in [82] isotropic cubic resonators are employed in an angle-

independent frequency selective surface. In Chapter 5, a 3D cube consisting of spiral resonators is investigated.

When it comes to realizing metamaterials there is the challenge of fabricating 3D conductive structures. Fused deposition modelling (FDM) has become a standard method for rapid prototyping, with a plethora of low cost machines widely available [83]. During this process, a thermoplastic filament is pushed in the back of a heated nozzle, which brings the material to its melting point. By moving the nozzle in space as the material is extruded, 3D structures can be realised in a layer-by-layer approach. The printed structure does not need to be solid and can be partially hollow [84].

FDM competes with Vat Polymerization (VP) which uses photosetting resins to form high resolution structures from a vat of liquid resin [85]. VP has very good resolution but a much smaller palette of materials whose average dielectric losses are higher. The loss tangent $\tan\delta$ of resins used in VP is in the order of 10^{-2} [86], [87], which is not optimal as will be shown in Chapter 5. A similar option to FDM is Direct Ink Writing (DIW), where, instead of a filament, functional inks are used [88]. DIW is heavily dependent on the material's viscosity, as the ink flow greatly affects the precision and resolution of the structure, and also determines if a supplementary curing system needs to be used. InkJet (IJ) printing is a method that uses drops of liquid inks to form conductive patterns on surfaces [89], [90]. Related to IJ is Aerosol Jet (AJ) printing, which also utilizes ink droplets [91]. However, AJ can achieve higher resolution because the ink does not come into direct contact with the nozzle walls. Additionally, the distance between the print head and the substrate can be adjusted, allowing printing on non-flat substrates. Even though both IJ and AJ are capable of creating multi-layered structures, 3D unit cells are beyond their scope.

In general, FDM works well with many common thermoplastics including acetonitrile butandiene styrene (ABS), poly-lactic acid (PLA), polyproylene (PP) and high impact polystyrene (HIPS) [92], [93]. Whilst these are all useful structural materials they are not electrically conductive and therefore do not immediately lend themselves to the fabrication of antennas and waveguides for instance. Furthermore, not all these materials are good choices for high fre-

quency electronics as they have rather more dielectric loss than is generally preferred. For example, many thermoplastic filaments have a loss tangent $\tan\delta$ that is greater than 10^{-3}. This will be discussed more in Chapter 5. There are reports of solely dielectric resonator antennas produced using FDM [94], [95], however the permittivity of these thermoplastics can be low. This can be address by loading the filament with fillers that can raise their dielectric constant [96].

In order to construct useful radio frequency (RF) devices, such as filters [97] and antennas [98], conductors are essential to couple feeds, create antennas and form resonant structures. Many examples of conductive filaments have been demonstrated using thermoplastics loaded with particles, including carbon fibre, copper and silver [99]–[101]. There are a number of issues faced when using these loaded filaments, from inherent drawbacks, such as relatively low conductivity ($\sim 10^4\,\mathrm{S/m}$) and sensitivity to moisture, to technical shortcomings, including particles damaging or clogging extrusion nozzles. Whilst lower conductivity is not a barrier to their use, it does generally limit the performance of RF devices which require low loss. An extra complication arises when printing successive layers of conductive materials, resulting in a lower conductivity along the vertical direction (due to the reduced vertical contact between the extruded cylindrical filaments) [102]. This anisotropic conductivity makes true three dimensional fabrication quite difficult and limited in scope.

One way to avoid these problems is to use conductors that have higher conductivities and deposit them in such a way as to ensure the vertical and horizontal conductance are identical. Wu et al. [103] and Bharambe et al. [104] used acrylate based materials combined with liquid conductors to demonstrate 3D printed LC circuits and antennas. Whilst successful, there were some limitations imposed by the need to remove the paint solvents during drying.

An alternative approach is to use 3D printing to fabricate dielectric moulds rather than the conductive parts directly. In fact, 3D printing of microchannels for use in various fields is not a new concept [105]–[107]. The conductive material or the electronic parts can be added on a second step, as shown by Goh et al. [108]. It should be noted that FDM produces porous structures. The pore size and the porosity of the produced structures are affected by

the fabrication conditions such as the nozzle size, infill parameter and layer height [109]. If the structure is printed too 'thinly', leaks could form inside the microchannels.

The next natural step is to fill the microchannels with a conductive material. Simulations have shown that operational microwave devices, such as waveguides and antennas, can be fabricated by filling the microchannels with liquid metal conductors [110]. A good example that highlights this is the work of Yu et al. [111], where liquid Gallium-Indium alloy was injected in the microchannels of a 3D printed mould to form a functional electronics circuit. More advanced methods include that of Bharambe et al. [112], where, using a process called vacuum-filling, liquid Gallium alloy is injected inside the cavities of the 3D printed mould to create RF antennas. The method is shown to be capable of rapid prototyping 3D structures.

Alternatively, liquid conductors could be incorporated in the 3D printing process itself, by turning them into a paste filament [113] or extruding them simultaneously with thermoplastic [114]. Both of these methods allow for the direct, one-step printing of liquid conductive parts and show great potential in stretchable electronics, where the liquid conductor could change its shape in response to a mechanical load and maintain electric contact between all parts. Gallium-based conductors were employed, due to the low melting point that is even lower than room temperature in some alloys. This requires the conductive parts to be fully enclosed inside the dielectric, which could be less ideal for some applications. Alternatively, if the conductor is not completely enclosed, these structures are quite fragile having a single layer of Gallium oxide surrounding a liquid core which does not solidify at room temperature [115].

Field's metal is an alloy consisting of 32.5% bismuth, 51% indium and 16.5% tin with a melting point at around 65^oC [116], [117]. It is an eutectic alloy, meaning that all its constituents melt at the same temperature. Its melting temperature is lower than the point where many thermoplastics start heat deforming, making Field's metal heat compatible with a range of FDM filaments [118]. Its bulk conductivity of 1.97×10^6 S/m is comparable to that of many silver-based paints, gallium alloys and conductive inks. A more detailed comparison is presented in Chapter 5. By injecting liquid Field's metal inside the printed moulds, 3D conductive structures inside a dielectric medium can be fabricated.

In this thesis, Chapter 2 formulates an analytic model based on the circuit theory description of SRRs and MI waves. The presented equations are fundamental in extracting the coupling coefficients and dispersion graphs of the studied structures. Chapter 3 outlines the setup for numerical simulations and details the procedure for fitting the simulations to experimental data. Chapter 4 explores the coupling and dispersion of SRRs in discrete and coalesced arrangements, using the analytic model and numerical setup from the previous chapters. The numerical simulations enable understanding of the electric coupling's behaviour, which allows for novel ways of dispersion control. Chapter 5 starts by investigating a range of dielectric and conductive materials for use in liquid metal injection, leading to the introduction of the Field's metal fabrication method. Following various technical characterizations, the method is used to fabricate 3D resonators. The chapter ends with a promising application of Field's metal in creating 3D circuits. Finally, Chapter 6 provides conclusions on the findings of the thesis and suggests potential future work to build upon the results.

Chapter 2
Circuit theory description of split ring resonators

Chapter 2 formulates the circuit theory description of SRRs and MI waves, a well-established model for studying such metamaterial structures. Starting from one element, the resonance of a single SRR is expressed in terms of circuit parameters. In a two-element system (dimer), both magnetic and electric couplings between elements are taken into account. Kirchoff's equations are applied to retrieve the currents and calculate the coupling coefficients. This is expanded on a periodic chain of resonators, where the dispersion is calculated both analytically and experimentally. In this formulation, there is no distinction between discrete and coalesced SRRs.

2.1 Single resonator

At its simplest form a SRR consists of a conductive loop with a slit as shown in Fig. 2.1(a). It can be viewed as a LCR circuit, where L is the self-inductance of the resonator, C is the capacitance at the gap and R is the resistance, see Fig. 2.1(b). The resonance frequency and quality factor of the element can be expressed as

$$f_0 = \frac{\omega_0}{2\pi} = \frac{1}{2\pi}\sqrt{\frac{1}{LC}} \qquad \text{and} \qquad Q = \frac{\omega_0 L}{R}\,. \tag{2.1}$$

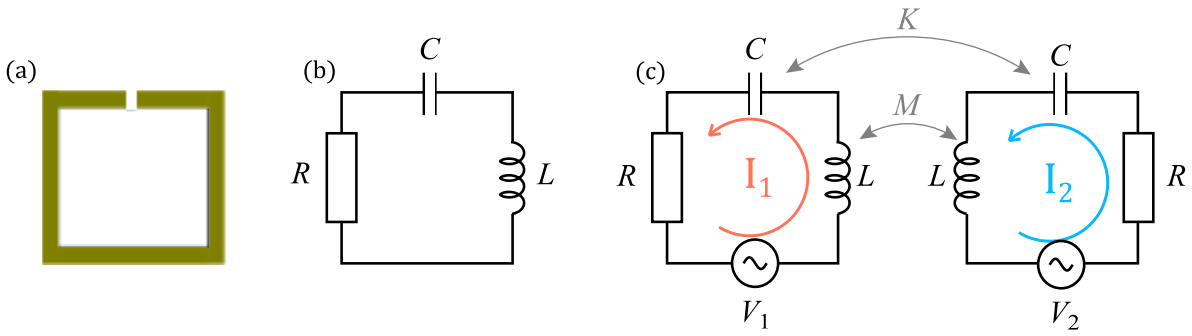


Figure 2.1: (a) A square SRR with a gap, (b) Circuit equivalent of a single SRR with self-inductance L, capacitance C and resistance R, and (c) Equivalent circuit model for a two-element system. There is a mutual inductance M and mutual capacitance K assumed between the two elements. $I_{1,2}$ are the currents of elements 1 and 2, while $V_{1,2}$ are the applied voltages to elements 1 and 2.

2.2 Two resonators

A two-element system where the SRRs are both magnetically and electrically coupled, as shown in Fig. 2.1(c), can be described as [55]

$$\begin{aligned} Z_0 I_1 + Z_M I_2 &= V_1 \\ Z_0 I_2 + Z_M I_1 &= V_2\,. \end{aligned} \tag{2.2}$$

Here, $I_{1,2}$ are the currents of elements 1 and 2, while $V_{1,2}$ are the applied voltages to elements 1 and 2 respectively. The self-impedance of a single resonator is

$$Z_0 = R + j\omega L + \frac{1}{j\omega C} = j\omega L\left(1 - \frac{\omega_0^2}{\omega^2} - j\frac{\omega_0}{Q\omega}\right), \tag{2.3}$$

where ω is the angular frequency. The mutual impedance including the magnetic and electric coupling terms is

$$Z_M = j\omega M + \frac{1}{j\omega K}, \tag{2.4}$$

where M and K are the mutual inductance and capacitance.

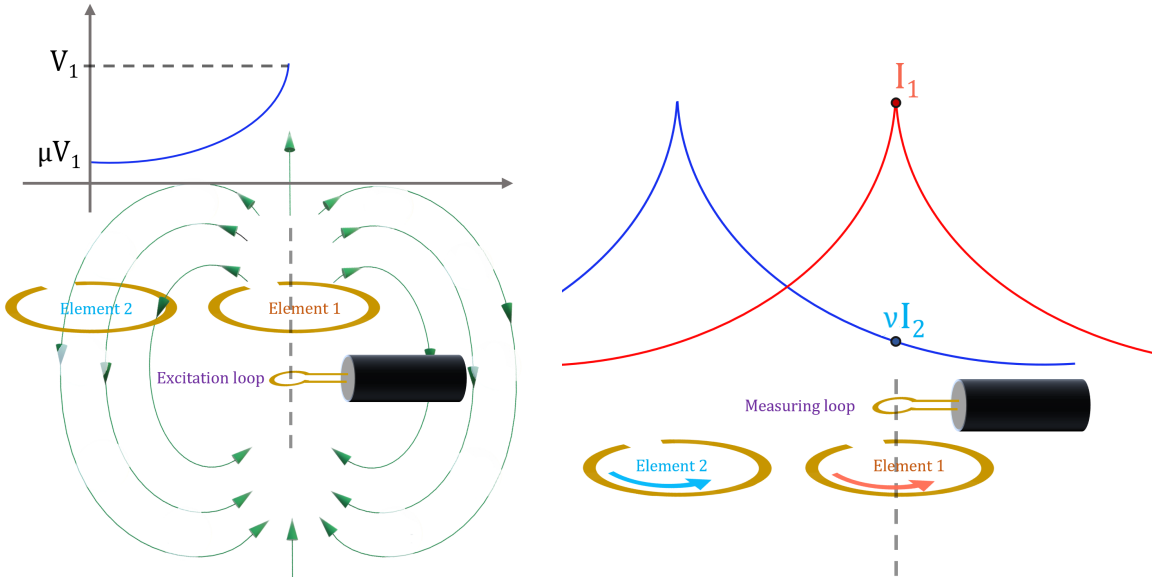


Figure 2.2: Additional interaction between the excitation/measuring loop antennas and the SRRs. (a) Correction factor μ due to the excitation loop's magnetic field reaching element 2, and (b) Correction factor ν due to the measuring loop picking the magnetic field of element 2.

In the case that only element 1 is excited, V_2 should be set to zero in Eq. 2.2. However, when a magnetic loop antenna is used to induce a voltage on element 1, some of its magnetic field will also reach element 2, as shown in Fig. 2.2(a), resulting in $V_2 \neq 0$ so that

$$V_2 = \mu V_1 . \tag{2.5}$$

At the same time, a magnetic loop antenna placed above element 1, H_1, will mainly record the magnetic field produced by the current of element 1 but will also pick up some of the magnetic field due to the current of element 2 and vice versa, see Fig. 2.2(b), so that

$$\begin{aligned} H_1 &= I_1 + \nu I_2 \\ H_2 &= \nu I_1 + I_2 \,. \end{aligned} \tag{2.6}$$

Here, μ and ν are corrections factors accounting for the unwanted interaction of the loops and the SRRs [60]. The correction factors can be calculated by removing one of the two SRRs from the setup. In the following, superscript F symbolizes that only the first element was present during the measurement and superscript S shows that only the second element was present during the measurement, so that

$$\mu = \frac{H_2^{\mathrm{S}}}{H_1^{\mathrm{F}}} \qquad \text{and} \qquad \nu = \frac{H_1^{\mathrm{S}}}{H_2^{\mathrm{S}}} = \frac{H_2^{\mathrm{F}}}{H_1^{\mathrm{F}}} \,. \tag{2.7}$$

The actual currents $I_{1,2}$ can be calculated by rearranging Eq. (2.6)

$$\begin{aligned} I_1 &= H_1 - \nu I_2 \\ I_2 &= H_2 - \nu I_1 \,, \end{aligned} \tag{2.8}$$

where I_2 can be substituted in,

$$I_1 = H_1 - \nu(H_2 - \nu I_1) = H_1 - \nu H_2 + \nu^2 I_1 \,, \tag{2.9}$$

allowing for I_1 to be determined

$$I_1 = \frac{H_1 - \nu H_2}{1 - \nu^2} \,. \tag{2.10}$$

Substituting Eq. (2.10) into Eq. (2.8) yields

$$I_2 = H_2 - \nu \frac{H_1 - \nu H_2}{1 - \nu^2} = \frac{H_2 - \nu^2 H_2 - \nu H_1 + \nu^2 H_2}{1 - \nu^2} \,, \tag{2.11}$$

which allows for I_2 to be determined as well

$$I_2 = \frac{H_2 - \nu H_1}{1 - \nu^2} \,. \tag{2.12}$$

The ratio of currents can then be calculated as:

$$\frac{I_2}{I_1} = \frac{H_2 - \nu H_1}{H_1 - \nu H_2} = \frac{\nu H_1 - H_2}{\nu H_2 - H_1} \,. \tag{2.13}$$

Equation (2.2) for the two element system can be rewritten as

$$\begin{aligned} I_1 &= \frac{V_1 - Z_M I_2}{Z_0} \\ Z_0 I_2 &= \mu V_1 - Z_M I_1 \,. \end{aligned} \tag{2.14}$$

Substituting I_1 in Eq. (2.14) leads to

$$Z_0 I_2 = \mu V_1 - Z_M \frac{V_1 - Z_M I_2}{Z_0} = \frac{\mu V_1 Z_0 - Z_M V_1 + Z_M^2 I_2}{Z_0} \,, \tag{2.15}$$

which can be rearranged as

$$(Z_0^2 - Z_M^2) I_2 = (\mu Z_0 - Z_M) V_1 \,, \tag{2.16}$$

to solve for I_2

$$I_2 = \frac{\mu Z_0 - Z_M}{Z_0^2 - Z_M^2} V_1 \,. \tag{2.17}$$

Substituting Eq. (2.17) into Eq. (2.2) yields

$$Z_0 I_1 = V_1 - Z_M \frac{\mu Z_0 - Z_M}{Z_0^2 - Z_M^2} V_1 = \frac{Z_0^2 - Z_M^2 - \mu Z_0 Z_M + Z_M^2}{Z_0^2 - Z_M^2} V_1 \,, \tag{2.18}$$

which, with a bit of mathematics

$$(Z_0^2 - Z_M^2) I_1 = (Z_0 - \mu Z_M) V_1 \,, \tag{2.19}$$

allows for current I_1 to be determined as

$$I_1 = \frac{Z_0 - \mu Z_M}{Z_0^2 - Z_M^2} V_1 \,. \tag{2.20}$$

The ratio of currents is

$$\frac{I_2}{I_1} = \frac{\mu Z_0 - Z_M}{Z_0 - \mu Z_M} \,, \tag{2.21}$$

which by substituting Z_0 and Z_M from Eq. (2.3) and Eq. (2.4) turns to

$$\frac{I_2}{I_1} = \frac{\mu j\omega L \left(1 - \frac{\omega_0^2}{\omega^2} - j\frac{\omega_0}{Q\omega}\right) - j\omega M - \frac{1}{j\omega K}}{j\omega L \left(1 - \frac{\omega_0^2}{\omega^2} - j\frac{\omega_0}{Q\omega}\right) - \mu j\omega L - \frac{\mu}{j\omega K}} \,. \tag{2.22}$$

Using the magnetic and electric coupling coefficients

$$\kappa_H = \frac{2M}{L} \qquad \text{and} \qquad \kappa_E = \frac{2C}{K} \,, \tag{2.23}$$

and dividing with $j\omega L$, Eq. (2.22) becomes

$$\frac{I_2}{I_1}\left[2\left(1 - \frac{\omega_0^2}{\omega^2} - j\frac{\omega_0}{Q\omega}\right) - \mu\kappa_H + \mu\frac{\omega_0^2}{\omega^2}\kappa_E\right] = 2\mu\left(1 - \frac{\omega_0^2}{\omega^2} - j\frac{\omega_0}{Q\omega}\right) - \kappa_H + \frac{\omega_0^2}{\omega^2}\kappa_E \,, \tag{2.24}$$

which can be rearranged to

$$2\left(1 - \frac{\omega_0^2}{\omega^2} - j\frac{\omega_0}{Q\omega}\right)\left(\frac{I_2}{I_1} - \mu\right) = \kappa_H\left(\mu\frac{I_2}{I_1} - 1\right) - \frac{\omega_0^2}{\omega^2}\kappa_E\left(\mu\frac{I_2}{I_1} - 1\right) \,. \tag{2.25}$$

Finally, the coupling coefficients can be shown to be equal to

$$Re\left[\kappa_H - \frac{f_0^2}{f^2}\kappa_E\right] = -2\frac{\frac{I_2}{I_1} - \mu}{1 - \mu\frac{I_2}{I_1}}\left(1 - \frac{f_0^2}{f^2} - j\frac{f_0}{fQ}\right) \,. \tag{2.26}$$

If the right side of Eq. (2.26) is calculated and plotted versus ω_0^2/ω^2 (or f_0^2/f^2) the graph should be of a line, whose intercept and slope are equal to κ_H and $-\kappa_E$ respectively. Furthermore,

the real and imaginary parts of the coupling coefficients can be calculated separately, which is important in the presence of retardation.

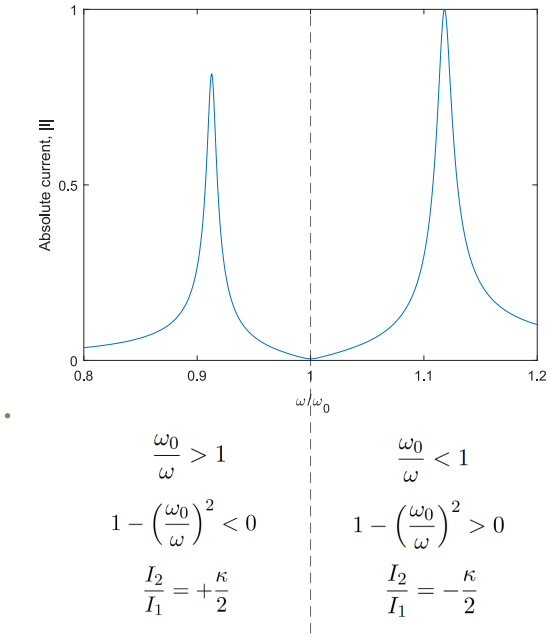


Figure 2.3: The normalised absolute current of element 1. The angle of I_2/I_1 can reveal the sign of the total coupling coefficient κ_{tot}.

In the absence of losses and disregarding the correction factors, Eq. (2.26) becomes

$$\kappa_H - \frac{\omega_0^2}{\omega^2}\kappa_E = -2\frac{I_2}{I_1}\left(1 - \frac{\omega_0^2}{\omega^2}\right) . \tag{2.27}$$

If the total coupling coefficient is

$$\kappa_{\text{tot}} = \kappa_H - \frac{\omega_0^2}{\omega^2}\kappa_E \, , \tag{2.28}$$

then the ratio of currents can be written as

$$\frac{I_2}{I_1} = -\frac{1}{2}\frac{\kappa_{\text{tot}}}{1 - \dfrac{\omega_0^2}{\omega^2}} . \tag{2.29}$$

If the current of any of the two resonators is plotted, a resonance split will appear as shown in

Fig. 2.3. For the lower resonance peak, $\omega < \omega_0$ and the denominator in Eq. (2.29) is negative. If $\kappa_{\text{tot}} < 0$, then the currents of the two resonators at the lower mode are not in phase and the mode is antisymmetric. On the other hand, the higher mode would be symmetric. If $\kappa_{\text{tot}} > 0$ the situation is reversed. Looking at the angle of I_2/I_1 can reveal the sign of the total coupling coefficient.

2.3 Array of resonators

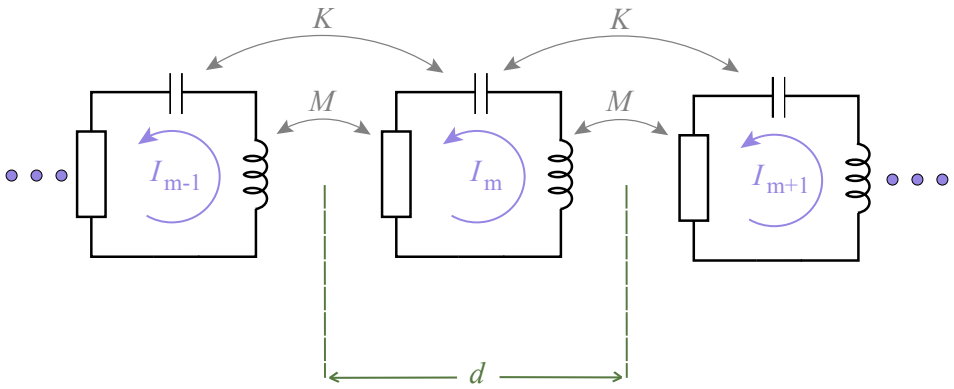


Figure 2.4: Equivalent circuit model for a periodic array of elements. There is a mutual inductance M and mutual capacitance K assumed between elements. I_{m-1}, I_m, I_{m+1} are the currents of the corresponding elements, and d is the unit cell size.

Similarly to the two-element system, in a one-dimensional N-resonator metamaterial array, as the one in Fig. 2.4, Kirchoff's equation for the m^{th} element can be written in the form of

$$Z_0 I_m + Z_M (I_{m-1} + I_{m+1}) = 0\,. \tag{2.30}$$

In a periodic structure, wave propagation can be assumed in the form of

$$I_m = I_0 e^{-jmkd}\,, \tag{2.31}$$

where I_0 is the amplitude of the wave, $k = \beta - j\alpha$ is the wave number with β and α being the dispersion and attenuation coefficients respectively, and d is the unit cell size. The currents

of any three consecutive elements I_{m-1}, I_m, I_{m+1} are connected as

$$I_{m-1} + I_{m+1} = I_0 e^{-jmkd}(e^{jkd} + e^{-jkd}) = 2I_m \cos kd\,, \tag{2.32}$$

so that Eq. (2.30) is transformed into

$$Z_0 + Z_M 2\cos kd = 0\,. \tag{2.33}$$

Substituting Z_0 and Z_M from Eq. (2.3) and Eq. (2.4), and diving by $j\omega L$ leads to

$$1 - \frac{\omega_0^2}{\omega^2} - j\frac{\omega_0}{Q\omega} + \left(\kappa_H - \frac{\omega_0^2}{\omega^2}\kappa_E\right)\cos kd = 0\,. \tag{2.34}$$

In the absence of losses R=0 and $Q \to \infty$. Then, inside the passband α=0, so that Eq. (2.34) becomes

$$1 - \frac{\omega_0^2}{\omega^2} + \kappa_H \cos\beta d - \frac{\omega_0^2}{\omega^2}\kappa_E \cos\beta d = 0\,, \tag{2.35}$$

which can be solved for ω (or f)

$$\frac{f}{f_0} = \sqrt{\frac{1 + \kappa_E \cos\beta d}{1 + \kappa_H \cos\beta d}}\,. \tag{2.36}$$

If losses are not negligible, Eq. (2.34) can be rearranged to

$$\cos(\beta d - j\alpha d) = -\frac{1 - \frac{\omega_0^2}{\omega^2} - j\frac{\omega_0}{Q\omega}}{\left(\kappa_H - \frac{\omega_0^2}{\omega^2}\kappa_E\right)}\,, \tag{2.37}$$

allowing for the dispersion and attenuation curves to be calculated by taking the real or imaginary part of the equation. In the presence of retardation, the coupling coefficients are complex, so that

$$\kappa_H = \kappa_H^{'} + j\kappa_H^{''} \qquad \text{and} \qquad \kappa_E = \kappa_E^{'} + j\kappa_E^{''}\,, \tag{2.38}$$

where $\kappa_H^{'}$, $\kappa_E^{'}$ are the real parts of the coupling coefficients and $\kappa_H^{''}$, $\kappa_E^{''}$ are the imaginary parts.

The dispersion and attenuation curves of the metamaterial array can be plotted analytically through Eq. (2.37), by knowing the resonance, quality factor and coupling coefficients, and through Eq. (2.32) by using experimental or numerical data of each resonator's currents.

2.4 Impedance matrix

In an array of N SRRs the applied voltages are connected with the induced currents through the impedance matrix

$$V = ZI\,, \tag{2.39}$$

where

$$V = \begin{bmatrix} V_1 \\ V_2 \\ \vdots \\ V_N \end{bmatrix} \qquad \text{and} \qquad I = \begin{bmatrix} I_1 \\ I_2 \\ \vdots \\ I_N \end{bmatrix}\,, \tag{2.40}$$

are N-dimensional vectors with V_m and I_m being the voltage and current of the m^{th} element, and Z is the $N \times N$ impedance matrix. The impedance matrix is constructed by putting the self-impedance of each SRR, Z_0, in the diagonal and the mutual-coupling term between element i and j, Z_M^{ij}, in the element of row i and column j. If two elements of the array are not coupled, the corresponding matrix element is zero. There can be more than one coupling terms present in the structure e.g in a 2D array SRRs can be planar in the x-direction and axial in the y-direction. If the resonance frequency, quality factor and coupling coefficients of the resonators are known, the impedance matrix can be constructed and, by knowing vector V, Eq. (2.39) can be solved for the vector I to retrieve the currents of each SRR. This method is particularly useful if the number of elements is high.

The analytic model formulated in Chapter 2 is used extensively in Chapter 4, where the coupling coefficients and dispersion diagrams for various arrangements of discrete and coalesced resonators are extracted. The analytic model is also utilized in Chapter 5 to study the resonators made with Field's metal, while the impedance matrix theory is employed to study the 3D cubic resonator.

Chapter 3
Numerical setup

This chapter introduces the methodology of reliably setting up numerical simulations using the Computer Simulation Technology (CST) software. The underlying aim is to fit the simulation to the experimental data, by replicating the experimental setup on CST and optimising the simulation parameters. The first part investigates different excitation and measuring tools. It is shown that an experimental setup can be reliably replicated on CST, using a magnetic field loop antenna as an excitation and a magnetic field probe to measure the magnetic field. The second part looks at how the simulated resonance is affected by the simulation parameters, such as the meshing, bounding box settings or the positions of the probes. It is shown that these parameters can be optimised to match the experimental results, without the need to set up more computationally demanding simulations.

3.1 Replicating the experimental setup

The Frequency Domain solver of CST was used for the numerical simulations. The Frequency Domain solver uses the finite element method (FEM), where the structure inside a bounding box is divided into smaller finite elements through a space discretization, thus creating a mesh of the object. Using the specified boundary conditions, CST solves Maxwell's equations for each finite element, creating a larger system of equations that can be solved to approximate a solution to the problem.

Alternatively, the Time Domain solver of CST, which uses the finite integration technique (FIT), could have been utilised. The main difference between the two solvers is that FIT attempts to solve the time-dependent Maxwell's equations, making it potentially more computationally demanding depending on the problem. Both methods are similar in the sense that they solve the integral formulation of Maxwell's equations and they should give approximately the same results. For the purposes of this work, where individual unit cells and metamaterial arrays with a small number of unit cells are investigated, the Frequency Domain solver was deemed to be more useful. Naturally, the size of the mesh and the bounding box will affect the final result significantly. In all simulations, open boundary conditions are used which virtually extend the space to infinity, as they would be in an experimental measurement.

Can the experimental setup be reliably replicated on CST? In order to answer this, a typical experimental setup used for measuring a SRR was gradually replicated on the simulation software. The test resonator shown in Fig. 3.1(a) was designed with standard printed circuit board (PCB) dimensions; it is a 20×20 mm square resonator made of copper (yellow) with track width of 1 mm, gap size 1 mm and thickness of 35 μm. There is no substrate and the resonator is surrounded by air. This resonator has a resonance around 2 GHz, which is problematic because the radiative losses in this regime are in the order of 10 Ω, which is quite high, and the resonator will have a low quality factor [58]. For the purpose of setting up the simulation a sharp resonance is preferable. Hence, a lumped element 100 pF capacitor with an internal resistance of 1 mΩ was placed at the gap of the resonator, to drive down the resonance to the MHz regime, where radiative losses are lower. For reference, at 100 MHz and

by using the formula for a small loop antenna [119] the radiative losses are in the order of $10^{-5}\,\Omega$.

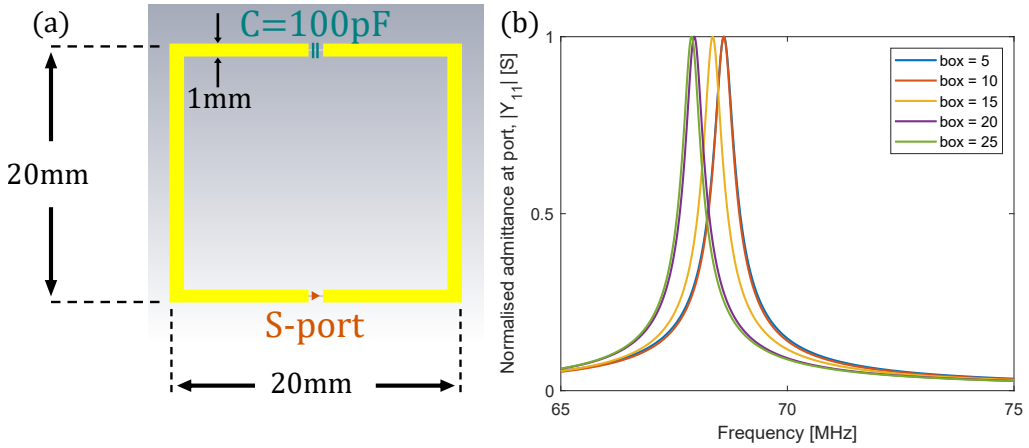


Figure 3.1: (a) CST setup for measuring a single SRR. A lumped 100 pF capacitor has been placed in the gap and the SRR is excited with an S-port on a second gap, and (b) The normalised admittance measured at the S-port showing the resonance peak changing with the bounding box size measured in cm.

On this first step, a second gap was introduced on the SRR so that it can be excited directly with an S-port. The S-port is a lumped element consisting of a current source with an inner impedance and has an input power of 1 W. Using the S-port enables the calculation of the S-parameters, impedance and admittance at the port. The S-parameters are the elements of the scattering matrix, describing the input-output relationships between ports in an electrical system which is excited by an electrical signal. The scattering matrix for a 2-port system is shown on Fig. 3.2. The elements of the scattering matrix are used to measure the reflected power at a port or the transmitted power from one port to another as a function of frequency.

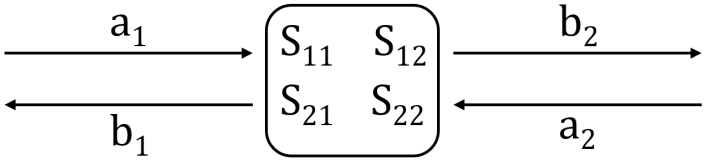


Figure 3.2: Illustration of the scattering matrix in a system with two ports.

The normalised admittance measured at the S-port at the default mesh and for different bounding box sizes measured in cm is shown in Fig. 3.1(b). The bounding box is expanded

symmetrically across the xyz directions, as shown in Fig. 3.3. It can be seen that the resonance peak shifts as the boundary box changes even at the same mesh settings.

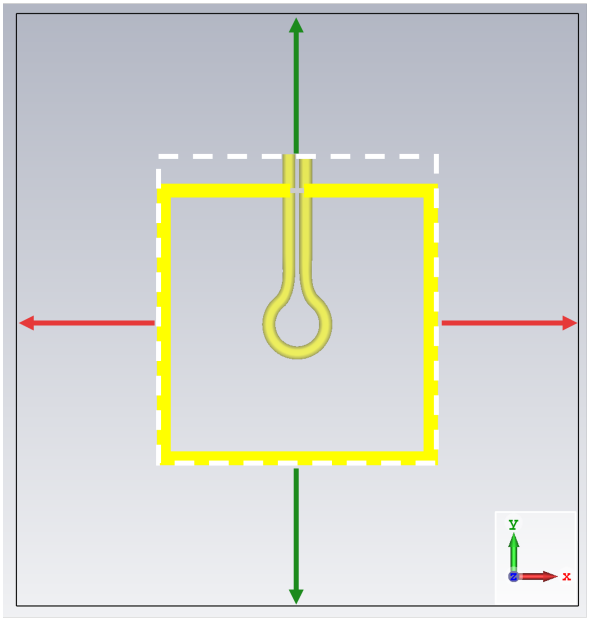


Figure 3.3: Visual representation of the bounding box size.

At resonance, the inductive and capacitive reactances of the circuit cancel each other out, making the self-impedance of the circuit real, with its absolute value being at a minimum. The impedance and admittance are inversely proportional, so at resonance the admittance is at a maximum. The resonance frequency is calculated directly from the peak of the admittance graph [120]. It is clear that f_0 decreases as the mesh becomes finer, see Fig. 3.4(a). In the legend, the mesh number is the maximum step width allowed in cm when curving out the mesh of the structure, while 'default mesh' corresponds to the CST default mesh settings. On the other hand, as the bounding box size increases, f_0 decreases. The effect of the bounding box is more prominent on the coarser meshes, while the finer mesh has a more constant f_0. As the bounding box increases, the solver has a bigger simulated space and can calculate the fields more accurately inside it, so that the results at different meshes appear to converge. The quality factor is calculated from the same graph using the expression

$$Q = \frac{f_0}{\Delta f_0}\,, \tag{3.1}$$

where Δf_0 is the bandwidth at the $-3\,\mathrm{dB}$ level below the maximum. The values of Q paint a similar picture in Fig. 3.4(b). Higher Q values correspond to finer meshes and as the bounding box size increases all data sets appear to converge.

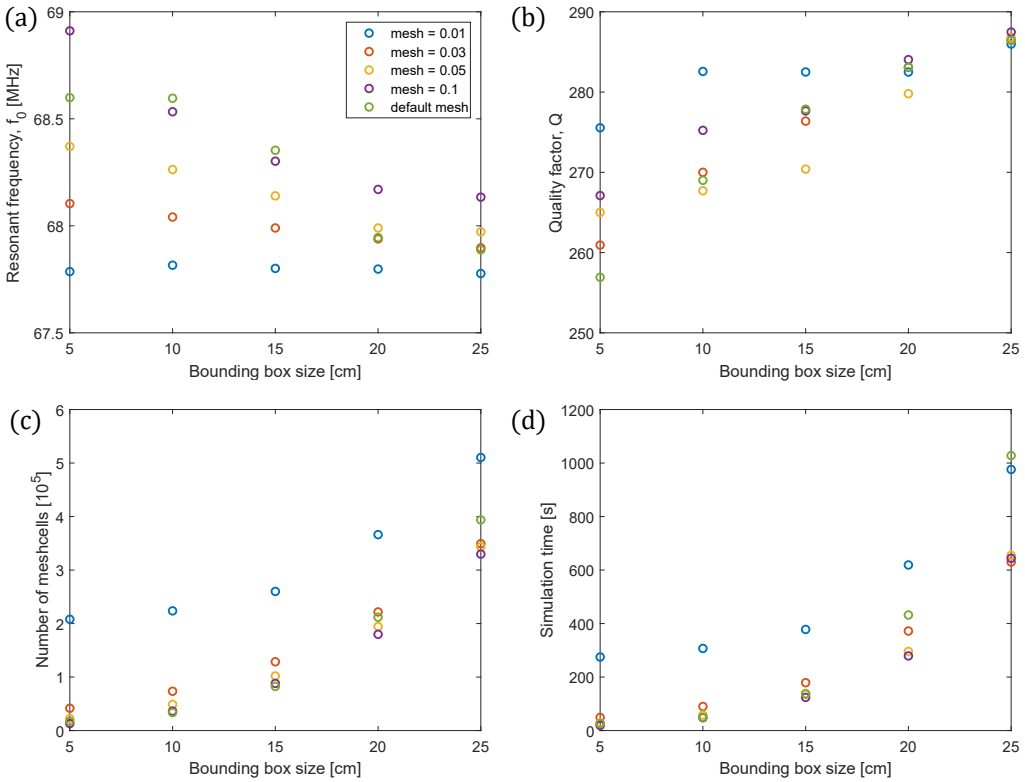


Figure 3.4: (a) Resonance frequency f_0, (b) Quality factor Q, (c) Number of meshcells, and (d) Total simulation time for different mesh and bounding box sizes when exciting the SRR directly with an S-port at a second gap.

The number of mesh cells and total time for each simulation are shown in Figs. 3.4(c) and (d). As expected for a finite element system, for finer mesh and larger bounding box, the simulation becomes more computationally demanding, as more elements are needed to divide the simulation space which results in an increase in the simulation time. This could pose a problem because the simulation time has started to visibly increase, but f_0 and Q have not converged completely. For example, at the smallest bounding box size of $5 \times 5 \times 5\,\mathrm{cm}$ the simulation time in most cases is a few seconds, while at the largest bounding box size of $25 \times 25 \times 25\,\mathrm{cm}$, the simulation time has increased to 600 seconds and above.

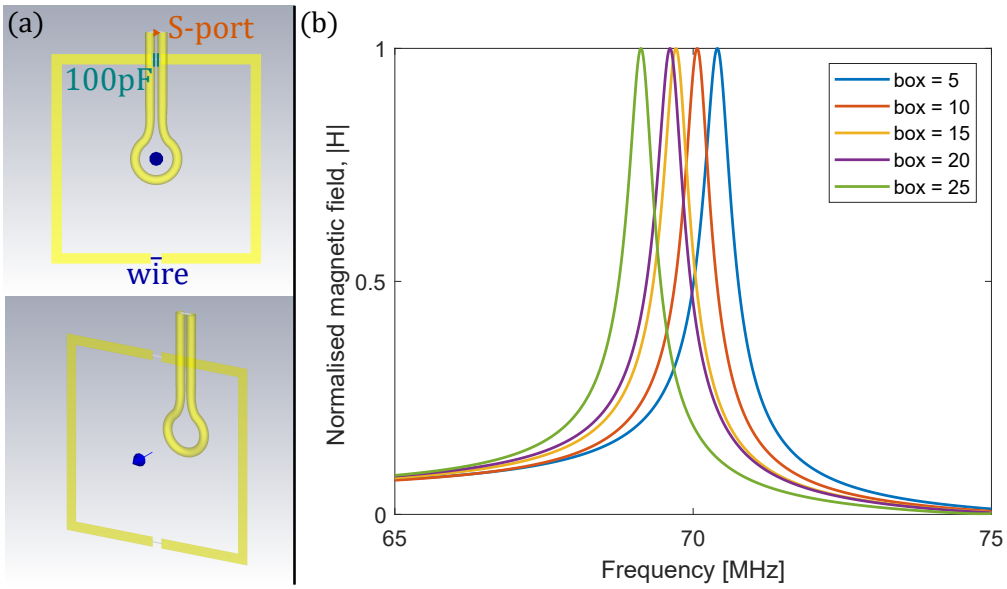


Figure 3.5: (a) CST setup for measuring a single SRR. A lumped 100 pF capacitor has been placed in the gap and the S-port on the second gap has been replaced with a wire, while the SRR is excited with a magnetic loop antenna. The resonance is measured with an H-probe which records the magnetic field, and (b) The normalised magnetic field measured from the H-probe showing the resonance peak changing with the bounding box size.

Exciting the SRR directly from a second gap is accurate but the geometry is changed in the process which is not practical. A less intrusive approach is to use a magnetic loop antenna to excite the structure. The S-port of the SRR is replaced with a wire to short the second gap and the resonator is excited axially using a magnetic loop antenna at 0.55 cm below the center of the SRR as shown in Fig. 3.5(a). Because the admittance at the excitation port is too weak, an H-probe is placed 0.25 cm above the center of the SRR to record the magnetic field. The normalised magnetic field at the default mesh settings and for different bounding box sizes is shown in Fig. 3.5(b).

The resonance frequency and the quality factor show a similar dependence on the mesh and bounding box size, see Figs. 3.6(a) and (b). The quality factor is setup-sensitive, so it is lower now that the SRR is excited with the magnetic loop. The number of meshcells and the total simulation time are in the same order of magnitude, as shown in Figs. 3.6(c) and (d).

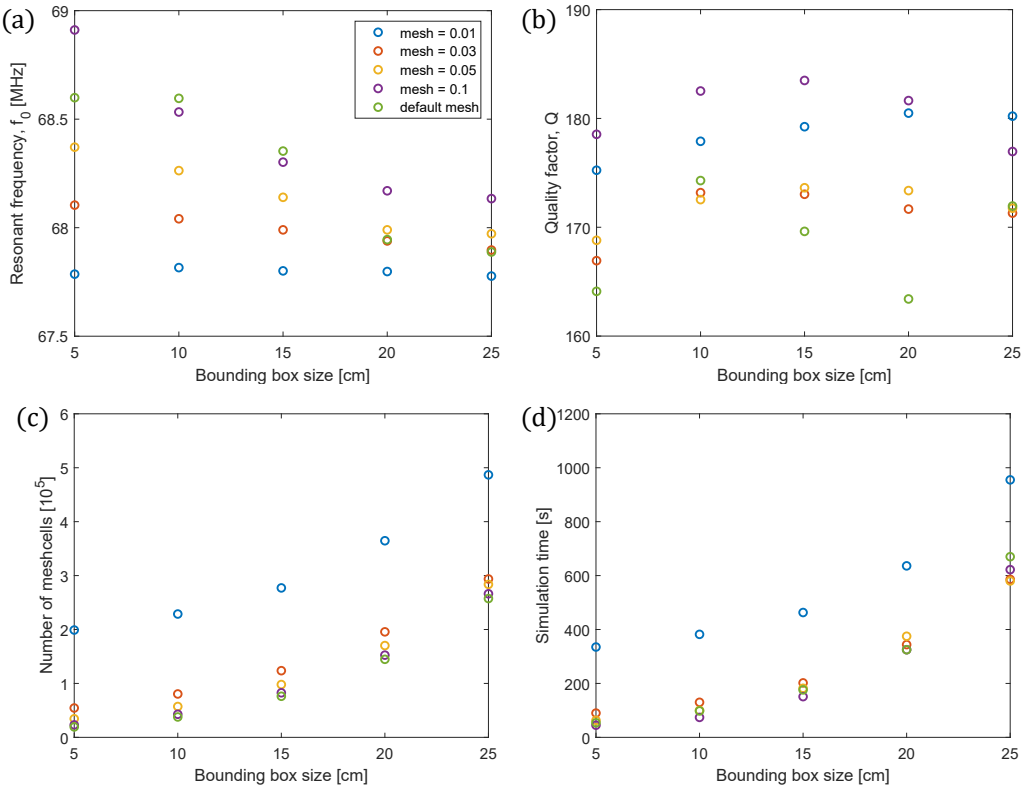


Figure 3.6: (a) Resonance frequency f_0, (b) Quality factor Q, (c) Number of meshcells, and (d) Total simulation time for different mesh and bounding box sizes when exciting the SRR with a magnetic loop and the second gap has been shorted with a wire.

Finally, the second gap is removed entirely while the SRR is excited with a magnetic loop, replicating a typical experimental setup shown in Fig. 3.7(a). The measured magnetic field recorded from the H-probe is shown in Fig. 3.7(b). The resonance frequency is slightly shifted because the self-inductance is increased due to the second gap closing, but the same dependence on mesh and bounding box size can be observed in Fig. 3. 8(a). The quality factor shown in Fig. 3.8(b) does not appear to converge for the mesh and bounding box sizes measured.

The number of meshcells and the simulation time have increased as shown in Figs. 3.8(c) and (d). For example, at the smallest bounding box size of 5 cm the simulation time in most cases is roughly 60 s, while at the largest bounding box size of $25 \times 25 \times 25$ cm, the simulation time has increased to at least 1000 s.

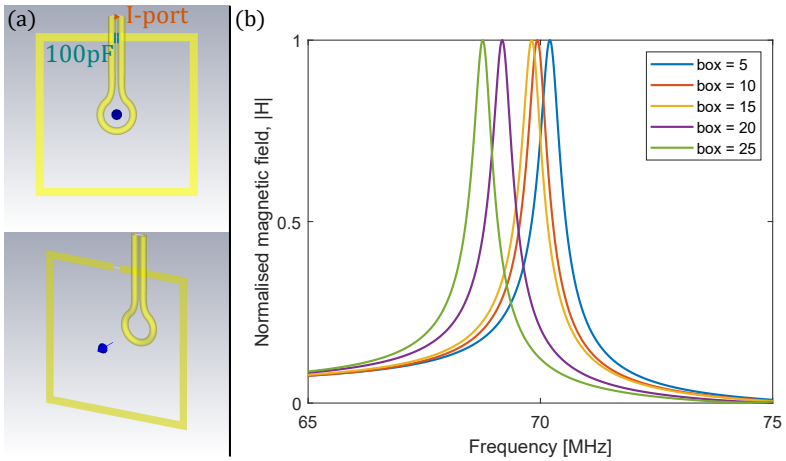


Figure 3.7: (a) CST setup for measuring a single SRR. A lumped 100 pF capacitor has been placed in the gap and the second gap has been removed entirely, while the SRR is excited with a magnetic loop. The resonance is measured with an H-probe which records the magnetic field, and (b) The normalised magnetic field measured from the H-probe showing the resonance peak changing with the bounding box size.

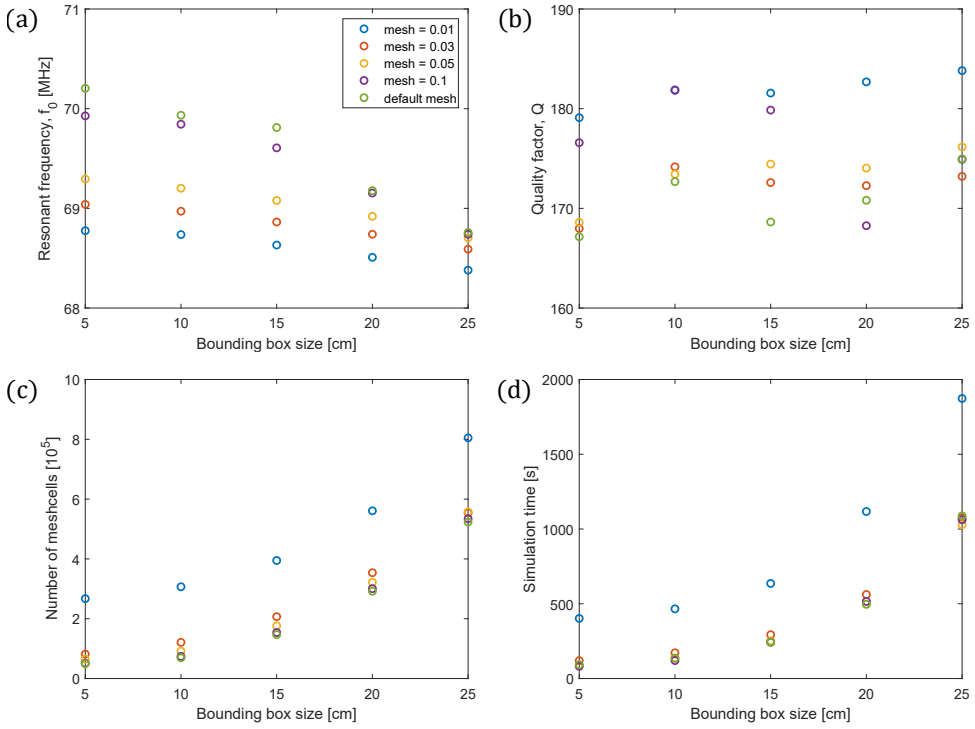


Figure 3.8: (a) Resonance frequency f_0, (b) Quality factor Q, (c) Number of meshcells, and (d) Total simulation time for different mesh and bounding box sizes when exciting the SRR with a magnetic loop and the second gap has been removed completely.

However, it is clear that relying on the f_0 and Q to converge, a more computationally demanding simulation is needed. For a single element this may not be a problem, but as more SRRs are added the simulation time would increase dramatically. In Chapter 4 it will be shown that there is another method of setting the mesh and boundary box size, by fitting the simulation data to the experimental measurement of the same SRR.

3.2 Simulation parameters

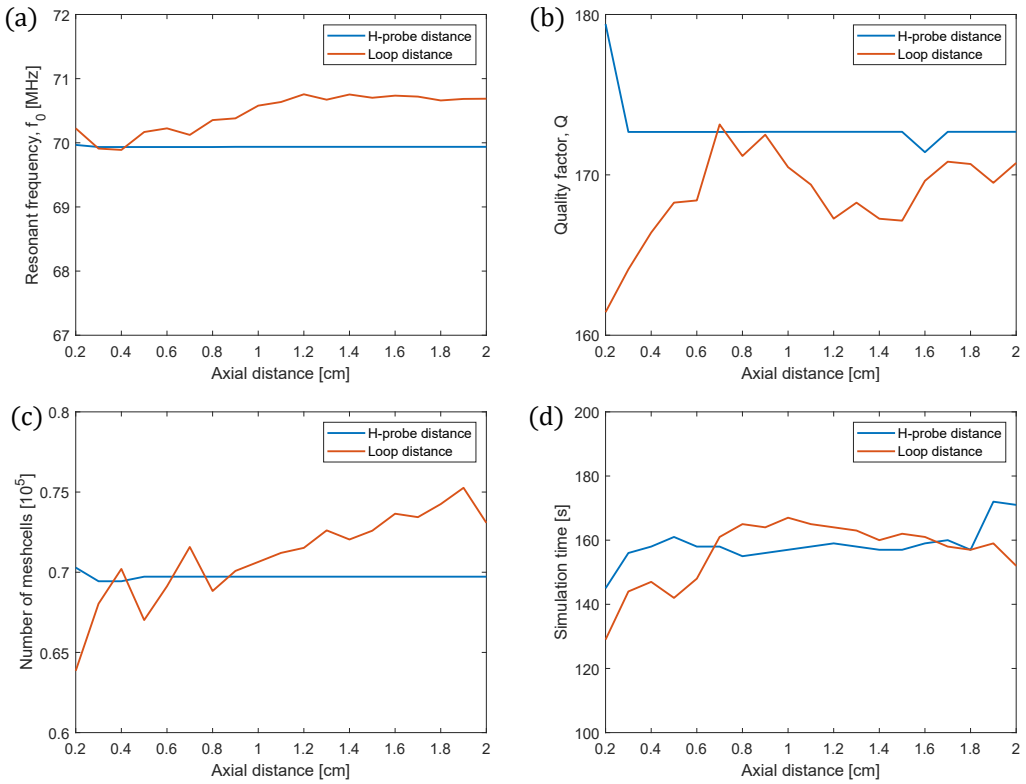
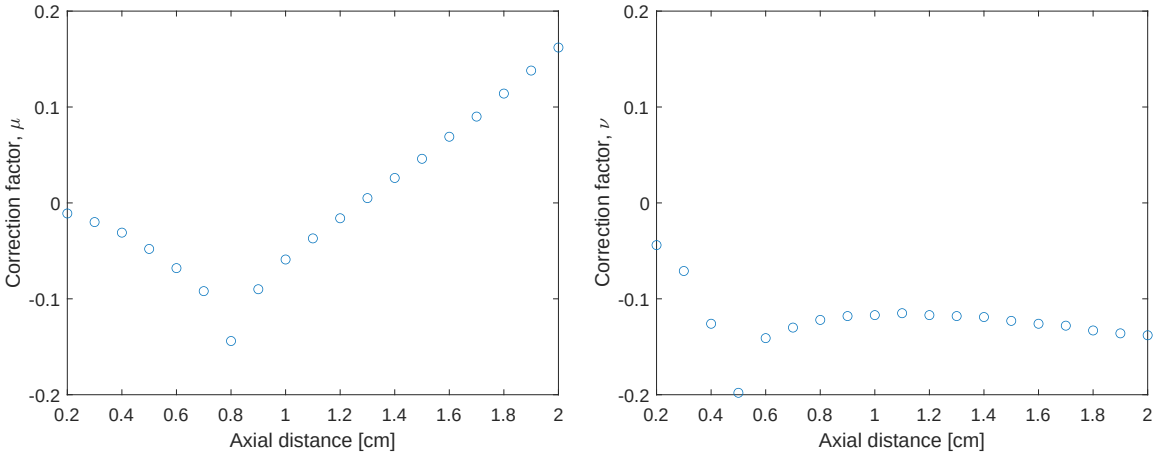


Figure 3.9: (a) Resonance frequency f_0, (b) Quality factor Q, (c) Number of meshcells, and (d) Total simulation time versus the axial distance of the H-probe and the loop from the center of the SRR.

Apart from the mesh and bounding box, there are other parameters that can affect the resonance. In Figs. 3.9(a) and (b), the f_0 and Q versus the axial distance of the H-probe and the loop from the center of the SRR are shown. These results are for default mesh settings and bounding box size of 10 cm. The H-probe has practically no effect on either graphs, which is

not surprising since it is just a point where CST calculates the magnetic field. The excitation loop antenna on the other hand is made of copper, and metal objects are known to affect the resonance due to eddy currents [53], [59]. As the excitation loop moves further away from the SRR, the simulation box becomes slightly larger which naturally increases the number of meshcells as shown in Fig. 3.9(c). However, this does not have a clear effect on the simulation time, which stays relatively constant in Fig. 3.9(d).



(a) (b)

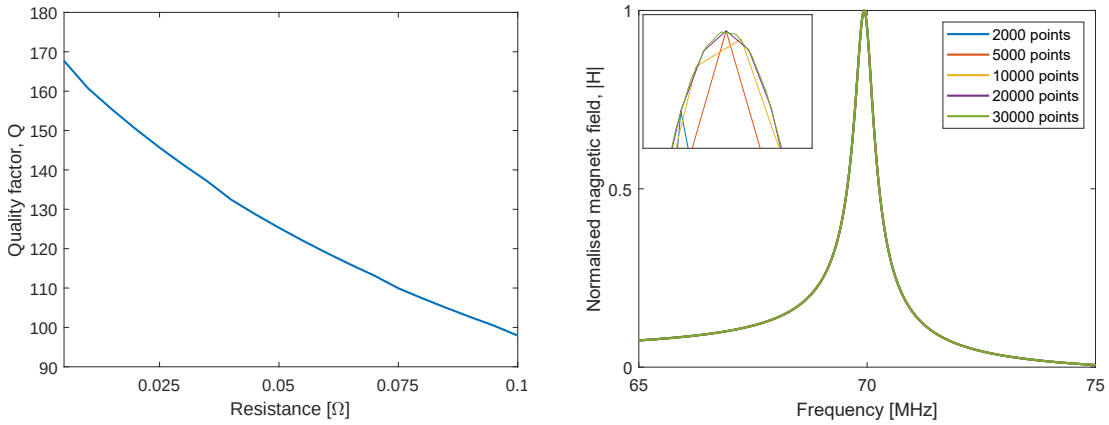
Figure 3.10: The correction factor (a) μ, and (b) ν versus the distance of the excitation loop from the center of the SRR.

At the same time, the axial distance of the excitation probe from the SRR affects the correction factors μ and ν, defined in Chapter 2, as shown in Fig. 3.10. This can be used to more accurately replicate the experimental setup on the simulation environment by matching the correction factors.

During a simulation, CST will compute ohmic, dielectric and radiative losses. However, in the experimental samples where a lumped capacitor has been soldered into the SRR, there are additional losses due to the soldering. By varying the resistance of the lumped capacitor, hence accounting for these extra soldering losses, the quality factor can be tuned to match the experimental values, see Fig. 3.11(a). Varying the resistance does not affect f_0 or the simulation time.

The resonance curves in CST are calculated using a pre-defined set of discrete frequency

values, referred to as "data points". The resonance peak for different number of data points is shown in Fig. 3.11(b). It appears that at least 20000 data points are needed to get an accurate shape at the resonance, which is crucial for calculating f_0 and Q. Surprisingly, increasing the number of data points does not increase the meshcells or the simulation time. Even though a 10 MHz range is shown on the graph, the simulation was set up for a 50 MHz range, which means data points are spaced at 2.5 kHz.



(a) (b)

Figure 3.11: (a) The quality factor Q versus the resistance of the lumped capacitor, and (b) The normalised magnetic field measured from the H-probe for different number of data points.

This chapter investigated how the experimental setup can be reliably replicated in CST. A novel approach is employed, where the numerical simulations are fitted to the experimental data, thus reducing the required computational resources and time. The effects of the meshing and boundary conditions on the resonance, quality factor and simulation time have been thoroughly analyzed. Other simulation parameters investigated include the position of the excitation loop, the resistance of lumped elements and the number of data points. The optimised settings are the key findings that enabled the accurate analysis in Chapter 4 on larger metamaterial arrays, while maintaining reasonable simulation times.

Chapter 4
Discrete and coalesced resonators

Chapter 4 explores novel ways of controlling the dispersion properties on arrays of SRRs. It builds on the previous two chapters by providing experimental results on discrete and coalesced SRRs in the MHz and GHz regimes. Using the analytical model introduced in Chapter 2, the coupling coefficients between elements are extracted from experimental data from dimer samples. The numerical simulations are fitted to the experimental data on the single resonator samples, with the optimisation procedure outlined in Chapter 3. The retrieved dispersion curves provide a proof that forward waves can propagate in planar arrays of coalesced square SRRs with three or four gaps. Experimental, numerical and analytical results are shown to be in excellent agreement. It is demonstrated that by optimising the simulation to match the experiment, we are able to calculate quantities that are difficult to measure experimentally such as the soldering losses. Furthermore, the agreement between experiment and simulation remains good for more complex structures, such as dimers and metamaterial arrays, enabling the use of the simulations to reliably investigate structures of coalesced SRRs for novel ways of dispersion control. By soldering different capacitors in the gaps, the coupling coefficients and the dispersion diagrams are extracted at higher frequencies.

4.1 Experimental methods and sample preparation

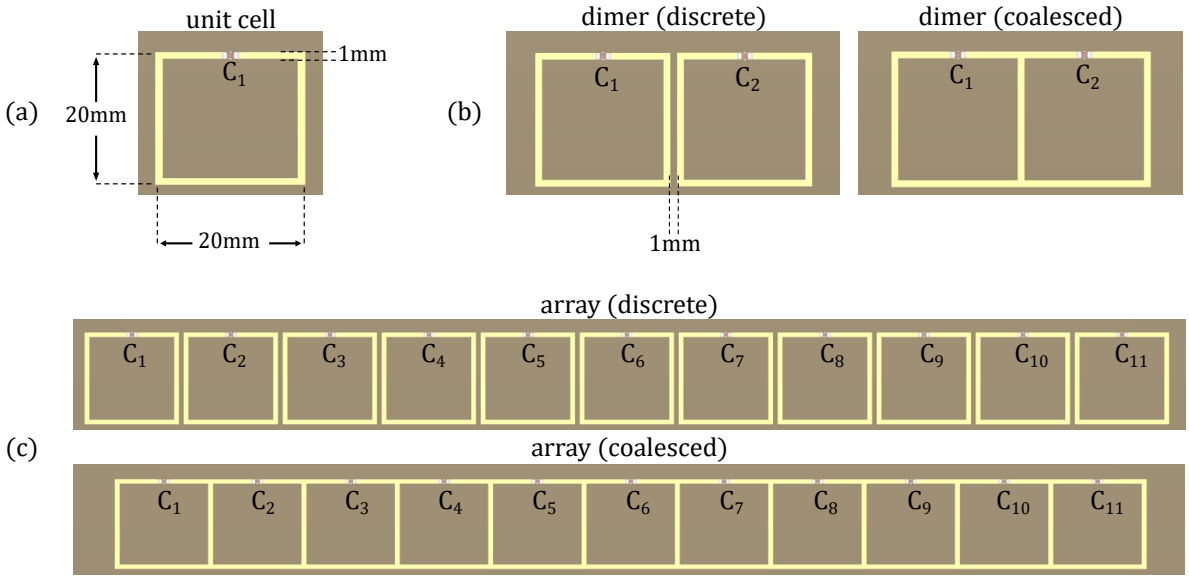
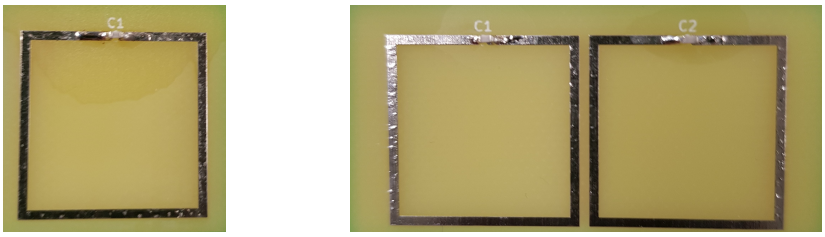


Figure 4.1: The one-gap group of PCB samples: (a) The unit cell, (b) Discrete and coalesced dimers, and (c) Discrete and coalesced 11-element arrays. Images from KiCad.

Three groups of square resonators were fabricated on PCB: one-gap, three-gap and four-gap. The one-gap samples are shown in Fig. 4.1. All resonators are square-shaped of side 20 mm, track width 1 mm, gap size 1 mm. The spacing between them is either 1 mm (discrete) or −1 mm (coalesced), meaning that the SRRs are sharing one side when coalesced. Each group consists of a unit cell (for measuring f_0, Q and correction factors), two dimers (for calculating κ_H, κ_E for the discrete and coalesced cases) and two 11-element arrays (for extracting the dispersion for the discrete and coalesced cases). The samples were fabricated on single-layered PCB with FR4 TG130−140 as the base material. The copper tracks have a thickness of 35 µm (1 oz). The PCB dimensions are 100 mm × 100 mm for the unit cell and dimers, and 270 mm × 100 mm for the 11-element arrays, while the thickness of the dielectric substrate in all samples is 1.6 mm. The solder resist layer around the resonators was removed at the design stage, so that capacitors could be soldered into the gaps. On their own, the resonators have a resonance in the range of 2−4 GHz depending on the number of gaps. This could be problematic because the wavelength is no longer significantly larger than the unit cell size, an assumption on which the analytical theory is founded on. Hence, 100 pF capacitors

were soldered into the gaps of the resonators, see Fig. 4.2 to drive down the resonance to the MHz regime, where circuit theory can be safely used. All capacitors were individually tested prior to soldering, so that those within a tolerance of less than 1% of rated capacitance values are used.



(a) (b)

Figure 4.2: Samples with soldered capacitors for the one-gap (a) unit cell, and (b) dimer.

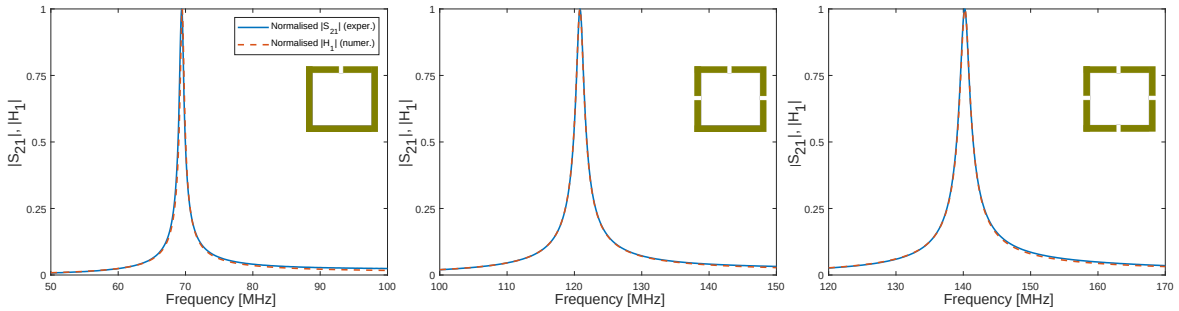
The measurements were performed using two magnetic loop antennas connected to a vector network analyzer (VNA). The loops had a diameter of 2.5 mm, wire thickness 1 mm and a gap size 1 mm. The first probe would excite element 1 below its center, while the second probe would move above the center of each element to record the S_{21} parameter. Background measurements without the samples were also recorded and subtracted from the measured S_{21} during analysis.

4.2 100 pF resonators

4.2.1 Unit cells

The experimental $|S_{21}|$ parameter (solid blue line) and numerical $|H_1|$ field (dashed red line) for the unit cell samples are shown in Fig. 4.3. The match between the numerical and experimental curves is excellent. The parameters used for each simulation are listed in Table 1.

The size of bounding box was kept at $10 \times 10 \times 10$ cm across all cases. Knowing the total capacitance, the self-inductance L_n can be calculated from Eq. (2.1), where n is the number of gaps in each resonator. It can be seen that L_n decreases slightly as more gaps are added and the total length of the metallic path is reduced. Initially, CST computes only ohmic, dielectric and radiation losses, all three of which are merged in the term R_n. The increase in R_n is



(a) (b) (c)

Figure 4.3: Normalised experimental $|S_{21}|$ (solid blue line) and numerical $|H_1|$ (dashed red line) measurements for the (a) One-gap, (b) Three-gap, and (c) Four-gap unit cells.

expected, as both ohmic and radiation losses increase with frequency. However, CST does not include the extra losses due to soldering and it calculates a higher quality factor than the one observed in the experiment. As was demonstrated in Chapter 3, by increasing the internal resistance of the lumped element capacitor, the simulated values of Q can be matched to the experimental ones. The quantity R_n^s is the additional resistance that was added and spread among all capacitors of each unit cell to match Q. The capacitors were soldered manually on the PCB samples, so the value of the solder resistance was found to range from 0.054 to 0.064 Ω for each capacitor. The values for f_0 and Q are shown in Table 2.

Table 1: Fitting calculations.

Resonator	Mesh size [cm]	Capacitance, C [pF]	Self inductance, L_n [nH]	Non-soldering losses, R_n [Ω]	Soldering losses, R_n^s [Ω]
one-gap	0.033	100	52.6	0.15	0.054
three-gap	0.095	100/3	52.1	0.20	0.192
four-gap	0.128	100/4	51.6	0.21	0.248

Table 2: Resonance results.

Resonator	Resonant frequency, f_0 [MHz]	Quality factor, Q
one-gap	69.4	116
three-gap	121	105
four-gap	140	100

4.2.2 Dimers

The next step is to characterise the coupling mechanisms for discrete and coalesced SRRs. There are six dimer samples. The normalised experimental $|S_{21}|$ parameter (solid blue line) and numerical $|H_1|$ field (dashed red line) measured above the first resonator are shown in Fig. 4.4. The position of the resonance of the unit cell is shown as the vertical dashed grey line. The agreement between experiment and simulation appears to slightly falter. The most likely reason is that CST produces an approximation for each geometry by creating a mesh. Although the simulation was fitted to the experimental data of the unit cell, when a second element is added, the geometry is changed and so is the meshing. Despite this, the agreement remains good overall.

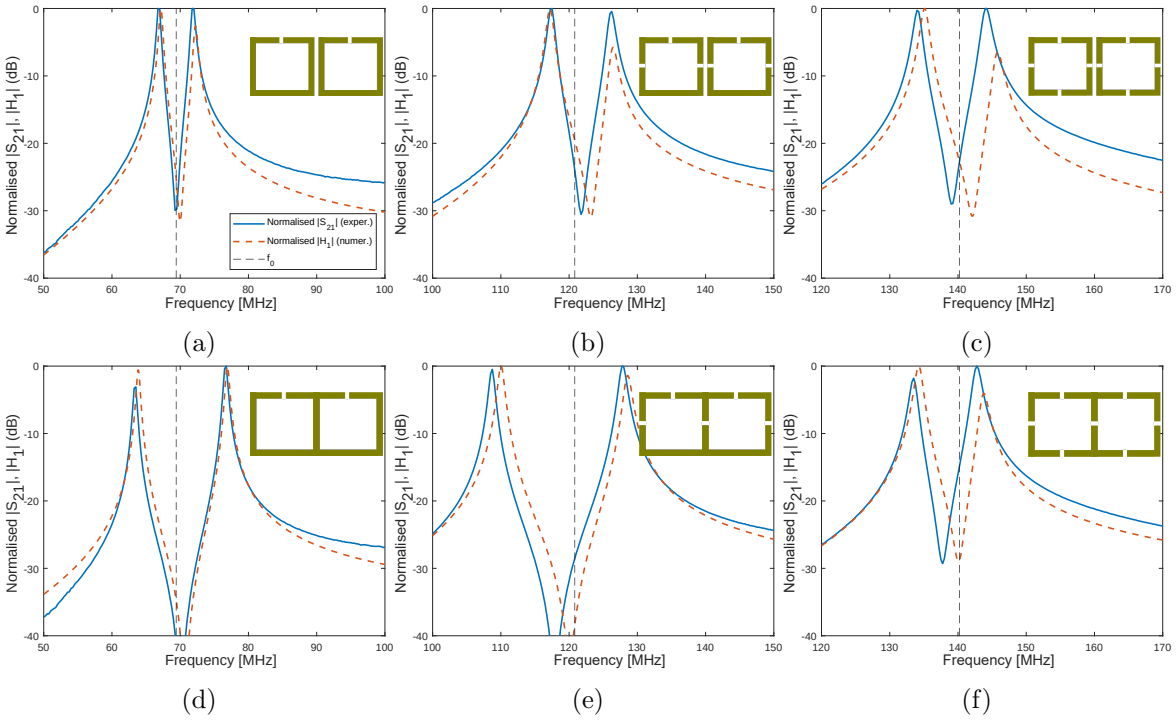


Figure 4.4: Normalised experimental $|S_{21}|$ (solid blue line) and numerical $|H_1|$ (dashed red line) measurements for dimer samples. (a)-(c) Discrete, and (d)-(f) Coalesced dimers. The grey dashed line shows the resonance of the unit cell. Insets show the geometry of each dimer.

There is a resonance split around the original f_0, resulting in two peaks. The separation and the position of the two peaks compared to f_0, is a measure of the magnitude and the sign of the total coupling coefficient. For example, the coalesced cases appear to have a larger

coupling compared to their discrete counterparts. Furthermore, in Figs. 4.4(e) and (f) the resonance split expands more towards lower frequencies, which is a sign of electric coupling [121].

This is further supported by the phase of the ratio of currents I_2/I_1 in Fig. 4.5. In the experiment, the S_{21} parameter is measured, while in the simulation the magnetic field H is recorded above each resonator. For the phase graphs the assumption that the currents are proportional to the S_{21} parameters and H fields was made. In the discrete cases, the currents are not in phase in the lower mode, which is antisymmetric. As the frequency increases, the currents become in phase, making the higher mode symmetric. This is the expected behaviour when the total coupling coefficient is negative. It is the same situation for the one-gap coalesced case, but the three-gap and four-gap coalesced dimers have the opposite behaviour; a lower symmetric mode and a higher antisymmetric one. This is a proof that in these two cases the total coupling coefficient switches to positive values.

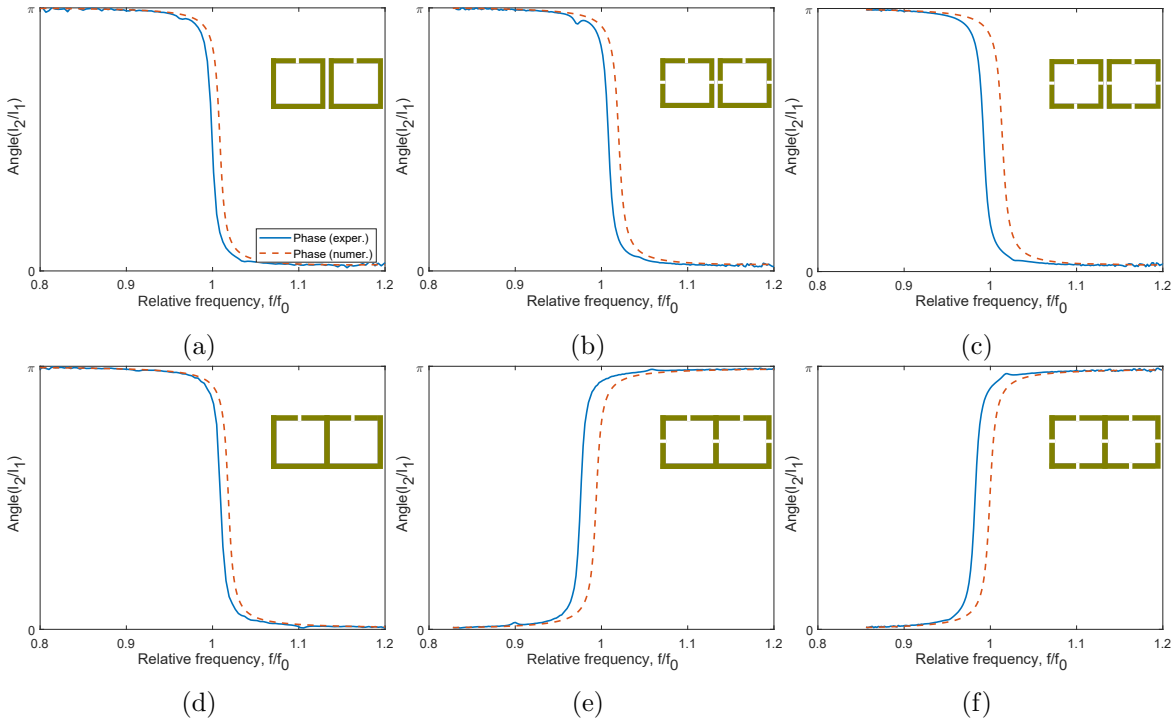


Figure 4.5: Experimental (solid blue line) and numerical (dashed red line) phase of the currents I_2/I_1. (a)-(c) Discrete, and (d)-(f) Coalesced dimers.

However, if the magnetic and electric coupling coefficients are to be measured separately, Eq. (2.26) needs to be used. Since the experimental and simulation data are still in a good agreement, the mesh and bounding box settings are kept the same in the simulations. The correction factors for each case are calculated from Eq. (2.7). In general, they increase slightly when the resonators are coalesced, since the second resonator is closer both to the first one and to the excitation probe. In all cases, however, the correction factors were calculated as $\delta = -0.07$ and $\mu = -0.1$ for both experiment and simulation.

Before extracting the coupling coefficients, there is one important issue to consider. The resonance frequency f_0 and the quality factors Q were measured on a setup with a single SRR. As shown previously in Chapter 3, the presence of metal nearby, specifically the presence of a neighbouring SRR, can affect the resonance. We expect that this would result in the appearance of a spike when plotting the right-hand side of Eq. (2.26) versus $(\omega_0/\omega)^2$ with the original values for f_0 and Q. Instead, a $f_{0,\text{fit}}$ and Q_{fit} can be used by minimising the size of the spike. In Fig. 4.6, the results of the fitting process for the one-gap discrete dimer are shown, where the size of the spike is minimized at slightly different values of f_0 and Q. The fitted values for all cases are summarised in Table 3.

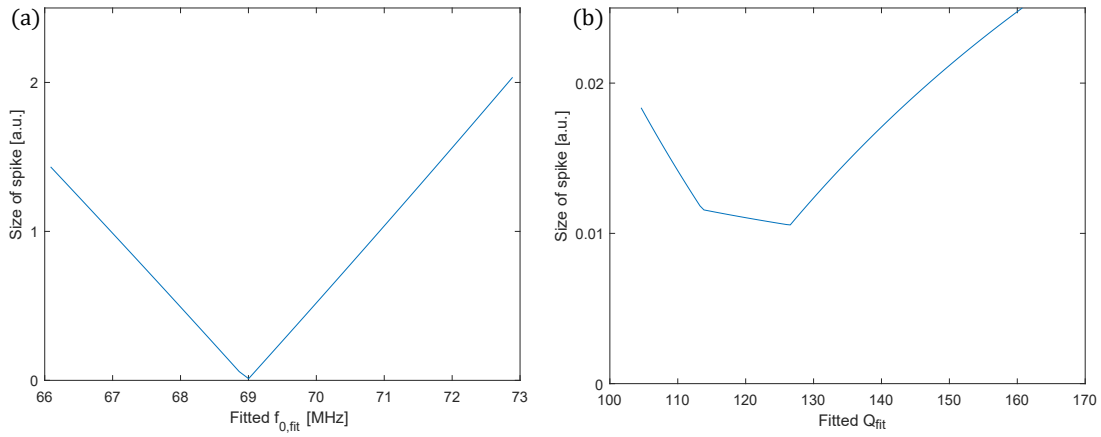


Figure 4.6: (a) Fitted Resonance, and (b) Fitted quality factor for the one-gap discrete dimer.

Now the coupling coefficients can be extracted by applying Eq. (2.26) using the experimental and numerical data. In Fig. 4.7 the real (blue, cyan) and imaginary (red, magenta) parts of the right side of Eq. (2.26) are plotted versus f_0^2/f^2. Experimental data are shown

Table 3: Fitted resonance and quality factor.

Dimer	Fitted resonance, $f_{0,\text{fit}}$ [MHz]	Fitted quality factor, Q_{fit}
one-gap discrete	69.0	126
one-gap coalesced	68.8	123
three-gap discrete	121	100
three-gap coalesced	120	117
four-gap discrete	138	111
four-gap coalesced	139	107

with blue (real) and red (imaginary), while numerical data are shown with cyan (real) and magenta (imaginary). As expected, in all cases the graph is of a line, with the linear fit also included. The agreement between experiment and simulation is excellent in almost all the cases. It can be observed that around the resonance there is the appearance of a spike, which has been greatly restricted due to the corrections factors and the fitting of the resonance and quality factor.

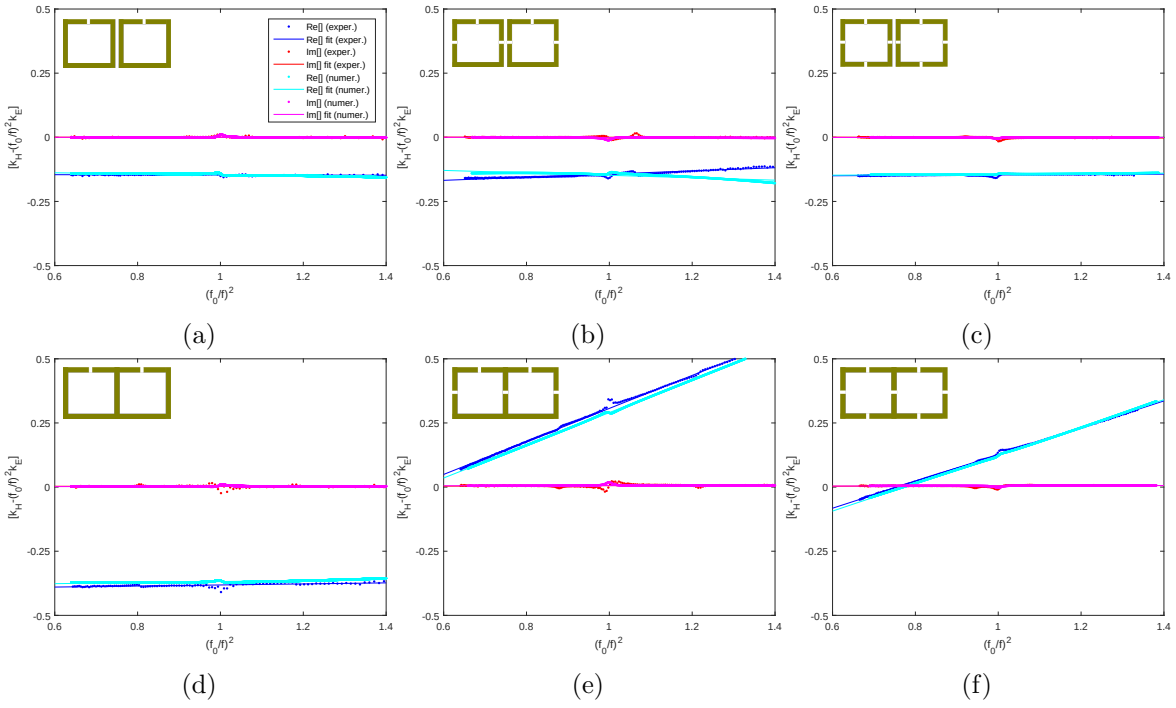


Figure 4.7: Real (blue and cyan) and imaginary (red and magenta) parts of Eq. (2.5) for experimental and numerical data for (a)-(c) Discrete, and (d)-(f) Coalesced dimers. The linear fit is also shown.

The imaginary parts of the coupling coefficients are near zero for all six configurations, confirming that retardation should be virtually non-existent. The slope of the real part of the discrete cases is flat and the intercept is negative, which according to our analytic model, implies that the electric coupling coefficient is practically zero while the magnetic coupling coefficient is negative. The same holds true for the one-gap coalesced case. The three-gap and four-gap coalesced dimers show a positive slope of the real part, attesting to a non-zero electric coupling coefficient.

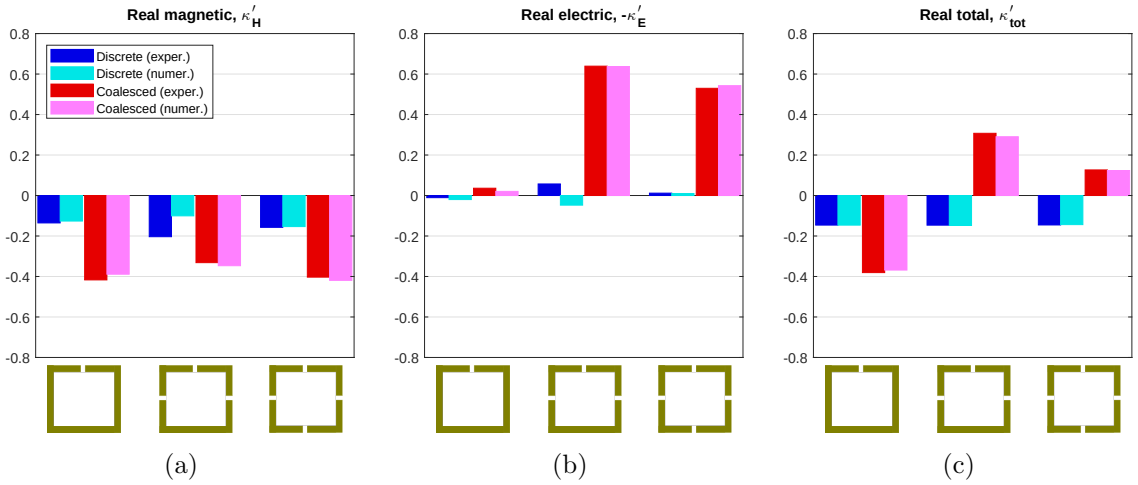


Figure 4.8: Real parts of the (a) Magnetic, (b) Electric, and (c) Total coupling coefficients for the discrete and coalesced dimers. The values for the discrete resonators are shown with blue (experimental) and cyan (numerical), while the values for the coalesced resonators are shown with red (experimental) and magenta (numerical).

The extracted values for the real part of the magnetic κ'_H, electric κ'_E and total coupling κ'_{tot} coefficients are summarised in Fig. 4.8. The values for the discrete resonators are shown with blue (experimental) and cyan (numerical), while the values for the coalesced resonators are shown with red (experimental) and magenta (numerical). One immediately notices the behaviour of κ'_{tot} in Fig. 4.8(c), which was calculated by adding κ'_H and $-\kappa'_E$. When the resonators are not in contact, κ'_{tot} is negative and constant, regardless of the number of gaps. It can be seen in Figs. 4.8(a) and (b) that the main contribution comes from the magnetic coupling coefficient κ'_H, while κ'_E is near zero for both the experimental and numerical setup. Even though there are minor disagreements between the two, the total coupling κ'_{tot} values

are almost identical. When the resonators are coalesced, $\kappa_H^{'}$ increases in magnitude and $\kappa_E^{'}$ stays approximately the same for the one-gap case. However, in the three-gap and four-gap cases where the shared side has a gap, $\kappa_E^{'}$ has a dramatic increase resulting in $\kappa_{\text{tot}}^{'}$ to turn positive. The agreement between experimental and numerical results is excellent. This switch to positive values means that a planar array will be able to support the propagation of forward MI waves. The imaginary parts of the coupling coefficients were calculated to be less than $< 1\%$ of their real counterparts and are therefore disregarded.

The magnetic coupling coefficient is higher in the coalesced dimers, compared to the discrete counterparts. From its definition,

$$\kappa_H = \frac{2M}{L}\,. \tag{4.1}$$

Since the SRRs are closer in the coalesced arrangement, the magnetic coupling M is higher. At the same time, because the SRRs are sharing one side, the self-inductance L is lower compared to the discrete case. Both of these factors contribute to the increase of κ_H.

Assuming that the number of gaps in one resonator is n, the total capacitance per unit cell can be estimated as

$$C = \frac{C_0}{n}\,, \tag{4.2}$$

where C_0 is the capacitance of a single gap. Using the expression for the electric coupling,

$$\kappa_E = \frac{2C}{K} \Rightarrow, \tag{4.3}$$

and the extracted values of κ_E, the mutual capacitance is calculated as $K \approx -C_0$ across all coalesced resonators with a gap on their shared side. The electric coupling coefficient can therefore be shown to vary with n as

$$\kappa_E = \frac{2C}{K} \approx -\frac{2}{n}\,. \tag{4.4}$$

We can conclude that the coupling can be tailored by the number of gaps per unit cell,

when the shared side of coalesced resonators is capacitively loaded. Furthermore, κ_E should not depend on the shape of the resonator. To investigate this behaviour, coalesced ring dimers of similar dimensions to the square SRRs were designed and simulated in CST. Only cases with a gap in the shared side were investigated. The coupling coefficients for both square and circular shapes were calculated and plotted versus the number of gaps. In Fig. 4.9(a), κ_H is slightly different for the two cases since the shape is different, but remains relatively constant as the number of gaps changes. In Fig. 4.9(b), $|\kappa_E|$ is shown to be the same for both shapes, decreasing as more gaps are added, while the data points follow the expected trendline from Eq. (4.4).

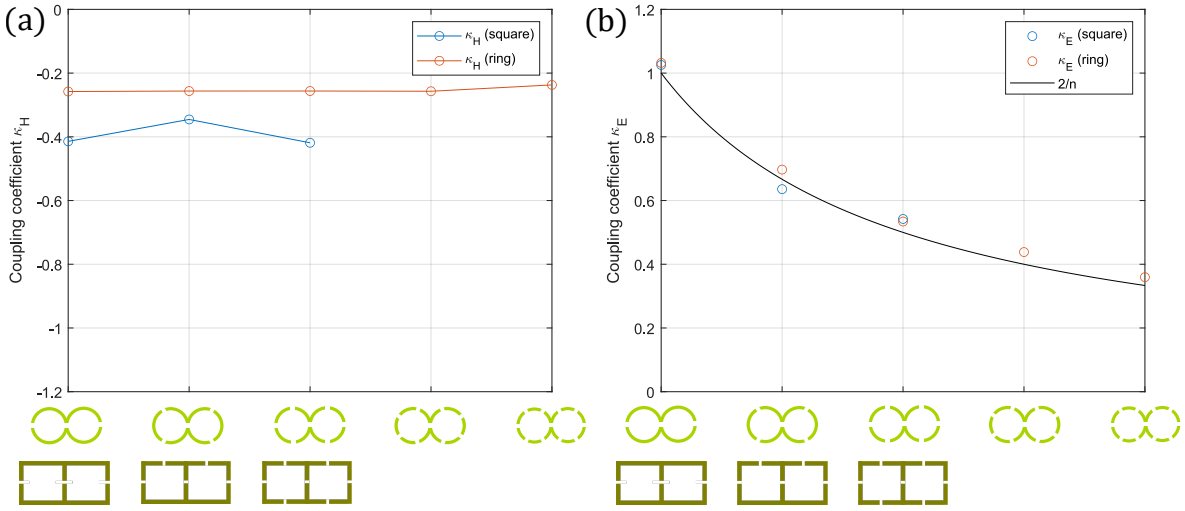


Figure 4.9: (a) Magnetic, and (b) Electric coupling coefficients for square (blue) and circular (red) SRRs calculated from CST.

4.2.3 Arrays

Equipped with the knowledge of all system parameters (f_0, Q of individual resonators and κ_E, κ_H for the coupling between resonators), we are now able to proceed with the investigation of the metamaterial arrays. The goal is to evaluate the dispersion characteristics of MI waves and verify our hypothesis that the wave nature (forward/backward) can be tailored by adjusting the capacitive links in planar arrays. The normalised experimental $|S_{21}|$ parameter (solid blue line) and numerical $|H|$ field (dashed red line) measured above the 6^{th} element of

the 11-element arrays are shown in Fig. 4.10. The numerical and experimental peaks are in reasonable agreement, featuring the correct number of peaks, although with a small frequency mismatch which was expected already from the analysis of the dimer samples. The largest disagreement appears in the three-gap discrete array, see Fig. 4.10(b), where the magnitude and the position of the experimental and numerical peaks are not the same. This is the same case where the biggest disparity of coupling coefficients was observed. Overall, the coalesced arrays appear to have a larger bandwidth than their discrete counterparts.

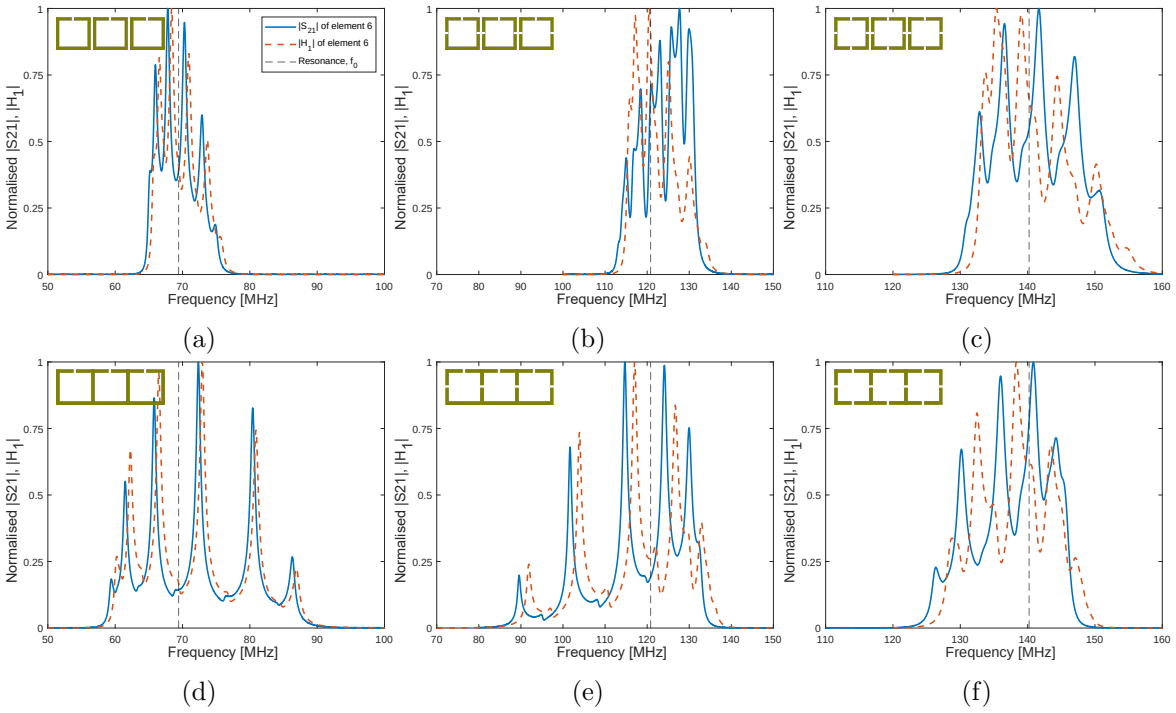


Figure 4.10: Normalised spectra for the experimental S_{21} (solid blue line) and the numerical $|H|$ (dashed red line) for the 6^{th} element in the 11-element array. (a)-(c) Discrete, and (d)-(f) Coalesced.

The dispersion curves $\beta(\omega)$ and $\alpha(\omega)$ are calculated analytically through Eq. (2.37). At the same time, assuming that the currents are proportional to the S_{21} parameters and H fields, Eq. (2.32) can be used to plot the dispersion curves from the experimental and numerical data of three consecutive resonators. This method of extracting the dispersion relies on the magnetic field of each resonator. In all cases, the frequencies outside the passband have relatively low magnetic fields, making the extracted dispersion unreliable in these parts, which

have therefore been discounted. The experimental (blue dots) and numerical (red dots) data, along with the analytical curves (yellow curve) are shown in Fig. 4.11. For the analytical curve, the experimental values for $f_{0,\mathrm{fit}}$, Q_{fit}, κ_E and κ_H were used.

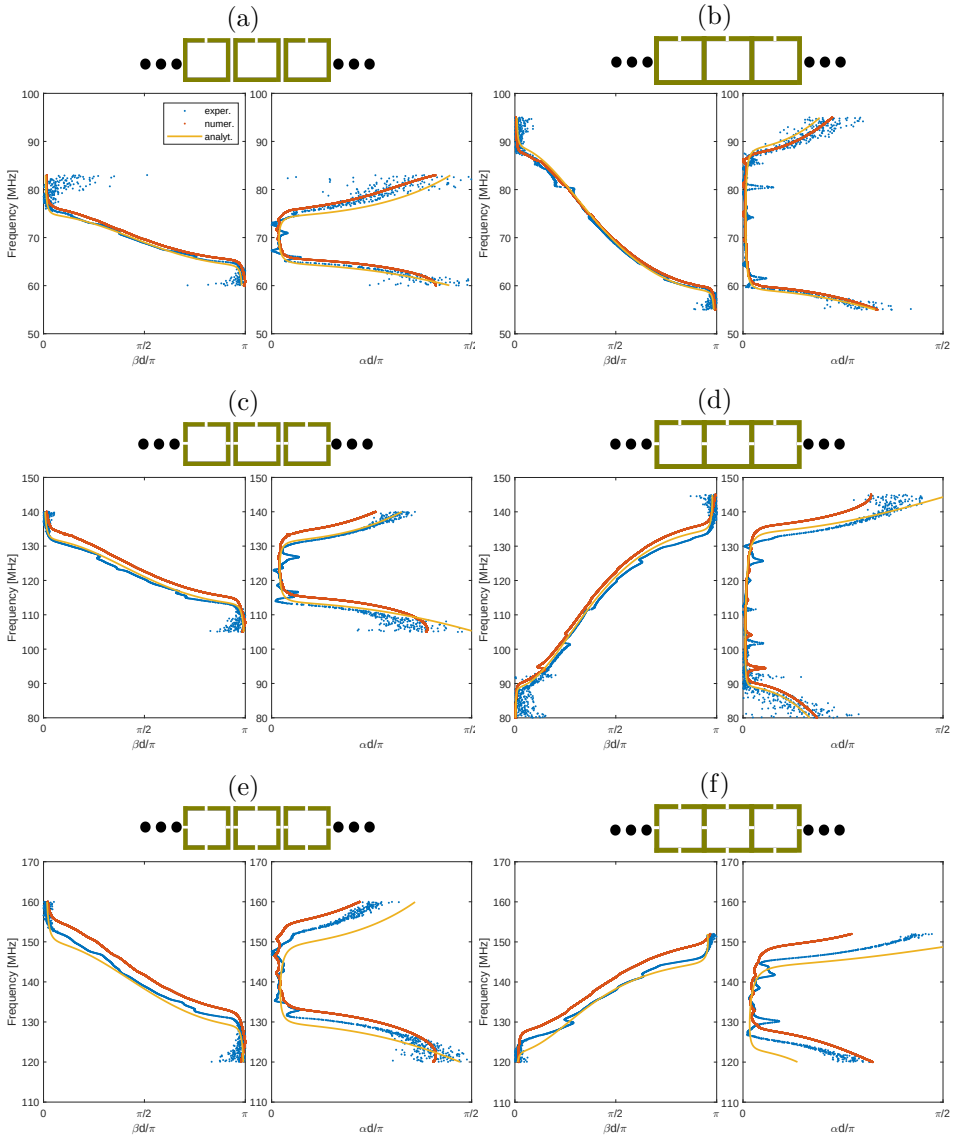


Figure 4.11: Dispersion curves for the (a), (b) One-gap, (c),(d) Three-gap, and (e), (f) Four-gap arrays. The experimental (blue dots) and simulation (red dots) data were calculated from the currents of three consecutive elements from the 11-element array. The analytic model (yellow line) includes losses and retardation.

Overall, there is a good agreement between the experiment, simulation and analytic model. There is backward wave propagation in all setups, except in the three-gap and four-gap

coalesced arrays, see Fig. 4.11(d) and (f), where the κ'_{tot} becomes positive. The analytical model using the two coupling coefficients κ_H and κ_E is in excellent agreement with the experimental data, accurately predicting the switch from a backward to a forward MI wave that occurs when the shared side is capacitively loaded. As discussed previously, CST produces an approximate solution, resulting in a slight divergence from the experimental curves, which is not surprising given the frequency mismatch arising already in the dimers. The fractional normalised bandwidth is nearly 14% for the discrete and four-gap coalesced arrays, while it is close to 40% for the one-gap and three-gap coalesced arrays, due to the higher coupling between elements.

4.2.4 Variable capacitors

The coupling between elements can switch signs depending on the number of gaps. However, this is not very practical because it requires changing the unit cell to switch between negative and positive coupling. Alternatively, an equivalent effect can be achieved by tuning the capacitance in the shared gap.

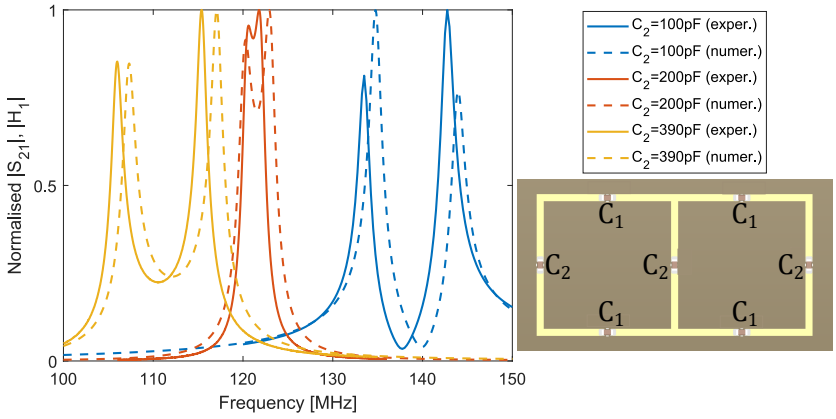


Figure 4.12: Normalised experimental $|S_{21}|$ parameter (solid lines) and numerical $|H_1|$ field (dashed lines) for different values of the capacitor C_2.

The normalised experimental $|S_{21}|$ parameter (solid lines) and numerical $|H_1|$ field (dashed lines) for the four-gap coalesced dimer are shown in Fig. 4.12. The capacitance C_1 was 100 pF for all measurements while C_2 was varied. For the numerical simulations, the mesh, bounding box and added lumped element resistance are the same as the ones fitted earlier, see Table 1.

The frequency mismatch between experimental and numerical data arises once again but the agreement remains good. There is a resonance split when 100 pF and 390 pF capacitors are placed in the C_2 gaps. However, when 200 pF are placed in the C_2 gaps, the resonance split is significantly weaker, showing signs of a near-zero total coupling between the elements.

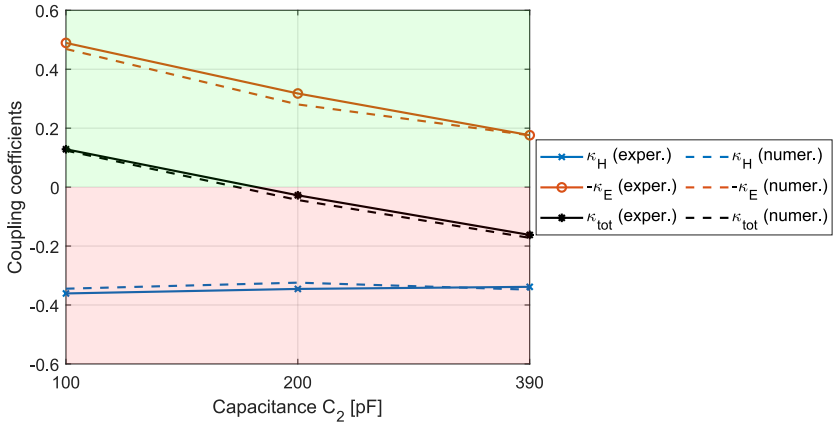


Figure 4.13: The coupling coefficients extracted from experimental (solid lines) and numerical (dashed lines) data for 100 pF, 200 pF and 390 pF capacitors in the C_2 gaps.

Table 4: Mutual capacitance.

C_2 [pF]	C_{tot} [pF]	κ_E	K [pF]
100	25	-0.47	-106
200	33	-0.30	-222
390	40	-0.18	-444

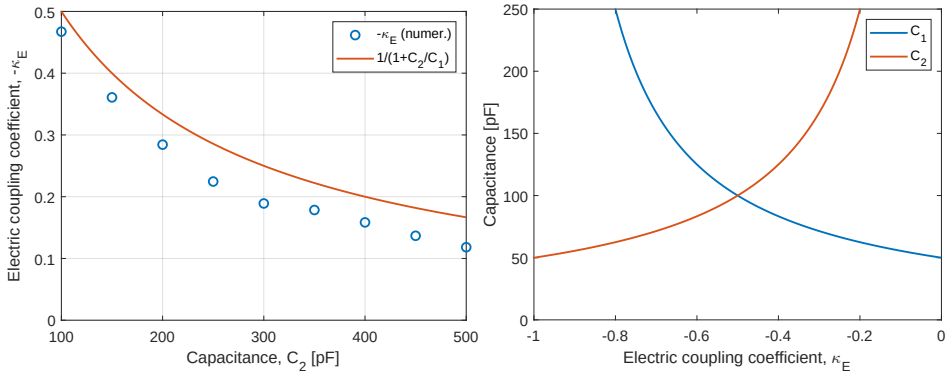
The extracted coupling coefficients for three different values of C_2 are shown in Fig. 4.13. When C_2=100 pF, κ_H is negative and $-\kappa_E$ is positive, so that the total coupling coefficient is positive. As the capacitance in C_2 increases, κ_E is reduced while κ_H remains approximately the same. This results in κ_{tot} to switch to negative values, passing through zero at around C_2=200 pF, as was expected from Fig. 4.12. Using the extracted values of κ_E, the mutual capacitance can be calculated. From Table 4, it appears that $K \sim -C_2$, so that

$$\kappa_E = -\frac{2}{C_2}\frac{C_1 C_2}{2C_1 + 2C_2} = -\frac{C_1}{C_1 + C_2}\,, \tag{4.5}$$

which can be solved for κ_E

$$\kappa_E = -\frac{1}{1+\dfrac{C_2}{C_1}}\,. \tag{4.6}$$

Using CST the coupling coefficients for more values of C_2 were calculated, as shown in Fig. 4.14(a). The curve from Eq. (4.6) is slightly higher than the extracted values of $-\kappa_E$, but the shape of the curve accurately traces the data points.



(a) (b)

Figure 4.14: (a) Comparison of κ_E extracted from numerical data and Eq. (4.6) for different values of C_2, and (b) C_1, C_2 from Eqs. (4.7) and (4.12) that produce different values of κ_E while the total capacitance stays the samef.

Taking this a step further, both C_1 and C_2 can be varied simultaneously to tailor the total coupling, while keeping the resonance frequency unchanged. If C is the total capacitance of the SRR, then from Eq. (4.5)

$$\kappa_E = -\frac{2C}{C_2}\,, \tag{4.7}$$

which can be solved for C_2

$$C_2 = -\frac{2C}{\kappa_E}\,. \tag{4.8}$$

Now the total capacitance is

$$C = -\frac{C_1\frac{2C}{\kappa_E}}{2C_1 - 2\frac{2C}{\kappa_E}}\,, \tag{4.9}$$

which can be rearranged as

$$C_1 - \frac{2C}{\kappa_E} = -\frac{C_1}{\kappa_E}\,, \tag{4.10}$$

and simplified to

$$\kappa_E C_1 - 2C = -C_1 \,. \tag{4.11}$$

Equation 4.11 can be solved for C_1

$$C_1 = \frac{2C}{1+\kappa_E} \,. \tag{4.12}$$

Assuming that the self-inductance of the SRR does not change, for the resonance to be the same, C needs to stay the same. Then in Eqs. (4.7) and (4.12) the only variable is κ_E, so there is a combination of C_1 and C_2 that can produce any desired electric coupling coefficient while the resonance remains unchanged. In Fig. 4.14(b), C_1 and C_2 for different values of κ_E with C=25 pF are shown.

The dispersion of MI waves in arrays of discrete and coalesced SRRs has been investigated. Our hypothesis that the total coupling coefficient switches to positive values when the resonators are coalesced and their shared side is capacitively loaded, thus allowing forward MI waves to propagate, has been confirmed. The analytic model formulated in Chapter 2 and the numerical setup outlined in Chapter 3, were vital in understanding this behaviour and allowed for novel ways of dispersion control by tuning the capacitance of the SRRs.

4.3 Higher frequencies

Will our approach of tunable MI wave dispersion work for metamaterials at higher frequencies? To investigate this we repeated the analysis on unit cells, dimers and arrays with a higher resonant frequency, by soldering smaller capacitors into the gaps. The numerical simulations were fitted to each resonator's experimental data, showing similar agreement as with the 100 pF samples, with a similar frequency mismatch arising as well. Hence, in this section only selected results are shown, highlighting the key features of our findings. All results for unit cells, dimers and arrays with 10 pF and 1 pF resonators soldered at the gaps are included in Appendix A.

4.3.1 Unit cells

The resonance results for the 100 pF, 10 pF and 1 pF capacitors are summarised in Table 5. In every gap there is a parallel plate capacitor with height h, width dl and gap size g

$$C_g = \varepsilon_0 \varepsilon_r \frac{h\, dl}{g} = 0.00031\,\text{pF}\,. \tag{4.13}$$

There is another contribution from the fringing effect approximated as

$$C_f = \varepsilon_0 \varepsilon_r (h + dl + g) = 0.018\,\text{pF}\,. \tag{4.14}$$

These capacitors, being parallel to each other, are added together to yield a total capacitance of 0.01831 pF. The soldered 100 pF and 10 pF capacitors have a substantially larger capacitance than that, which can be ignored in the calculations. However, in the 1 pF case, the natural capacitance of the gaps cannot be ignored because it is approximately 2 % of the soldered capacitor. The self-inductance for each group of samples decreases as more gaps are added and parts of the conductor are removed. At the same time, as the frequency increases so does the self-inductance. This is due to the skin depth effect, which reduces the effective thickness of the conductor at higher frequencies [119].

Table 5: Resonance results.

Capacitor [pF]	Resonator	Mesh	Resonant frequency, f_0 [MHz]	Self inductance, L [nH]	Quality factor, Q
100	1-gap	0.033	69.4	52.6	116
100	3-gap	0.095	121	52.1	105
100	4-gap	0.128	140	51.6	100
10	1-gap	0.022	217	53.7	155
10	3-gap	0.076	379	52.9	158
10	4-gap	0.100	438	52.8	146
1	1-gap	0.011	621	64.5	98
1	3-gap	0.032	1103	61.3	77
1	4-gap	0.078	1303	58.6	79

The quality factor appears to peak at around 400 MHz and then declines rapidly as the

losses become larger. Initially, CST computes ohmic, radiative and dielectric resistances which are all combined in the term R_n shown in Table 6. The ohmic resistance accounting for the skin depth δ can be expressed as

$$R_{\text{ohm}} = \rho_0 \frac{l_{\text{tot}}}{hdl - (h - 2\delta)(dl - 2\delta)}, \tag{4.15}$$

where ρ_0 is the resistivity of copper and l_{tot} is the perimeter of the SRR. Due to the skin effect, the ohmic resistance increase with frequency [119].

Table 6: Resistances.

Capacitor [pF]	Resonator	R_n [Ω]	R_{diel} [Ω]	R_n^s [Ω]
100	1-gap	0.15	0.067	0.054
100	3-gap	0.20	0.091	0.192
100	4-gap	0.21	0.092	0.248
10	1-gap	0.301	0.154	0.171
10	3-gap	0.408	0.203	0.390
10	4-gap	0.420	0.190	0.575
1	1-gap	1.337	0.999	1.500
1	3-gap	2.525	1.289	3.435
1	4-gap	3.153	1.022	3.033

The radiative resistance can be approximated using the formula for a small loop antenna [119],

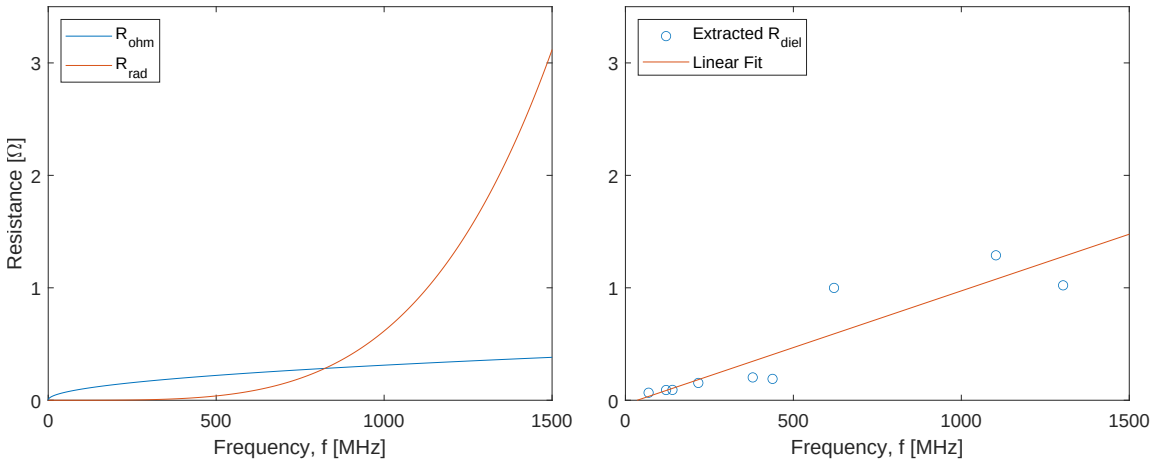
$$R_{\text{rad}} = 320\pi^4 \left[NA \left(\frac{f}{c} \right)^2 \right]^2, \tag{4.16}$$

where N is the number of turns (in our case $N = 1$), A is the cross-section of the SRR, f is the frequency and c is the speed of light. The ohmic and radiative resistances versus frequency are plotted in Fig. 4.15(a). At lower frequencies the radiative resistance is negligible while most of the losses come from the ohmic resistance. As the frequency goes up, the radiative losses rapidly increase and become the main contributor to the total losses. To evaluate the dielectric resistance R_{diel}, the values of R_{ohm} and R_{rad} are calculated at the measured resonant frequencies from Eqs. (4.15) and (4.16). Using the calculated values of R_n from CST, the dielectric resistance can be extracted. The extracted points are plotted in Fig. 4.15(b). A

line can be fitted to the data points to retrieve an empirical expression for R_{diel},

$$R_{\text{diel}} = 0.001 f \,. \tag{4.17}$$

Using the equations for R_{ohm}, R_{rad}, R_{diel} and the average self-inductance of 55.6 nH the quality factor can be plotted versus the frequency in Fig. 4.16. Since R_n^s is not included, the approximated Q is higher than the measured values. However, the maximum is around the same frequency and the shape of the curve appears to be similar to that of the measured values.



(a) (b)

Figure 4.15: (a) Ohmic and radiative resistances versus frequency calculated analytically, and (b) Extracted values for the dielectric resistance versus frequency.

As previously discussed, the soldered capacitors have a fixed internal resistance of their own. However, capacitors have a frequency-dependent resistance as well called the equivalent series resistance (ESR). Both of these can be estimated from the manufacturer's technical data sheet. However, by soldering the capacitors at the gaps, additional resistance due to the connection is introduced. These resistances are included in the term R_n^s but due to the different number of gaps, it is not possible to find a closed-form expression, and it is therefore not included in the calculation of Q in Fig. 4.16. By gradually increasing the resistance of the lumped capacitors and repeating simulations in CST, the quality factor that matches the experiment can be found. The resulting values of R_n^s found via this iterative procedure, are

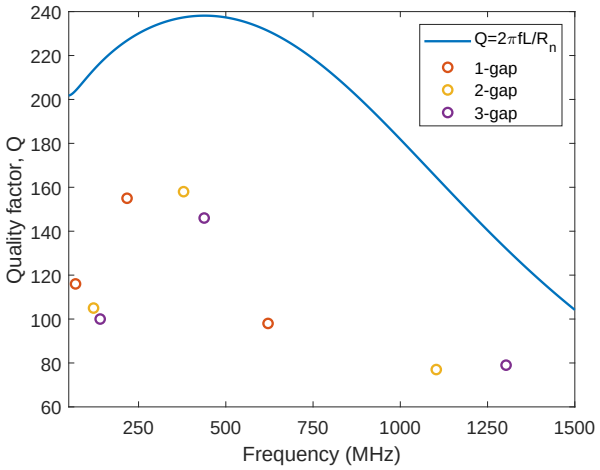


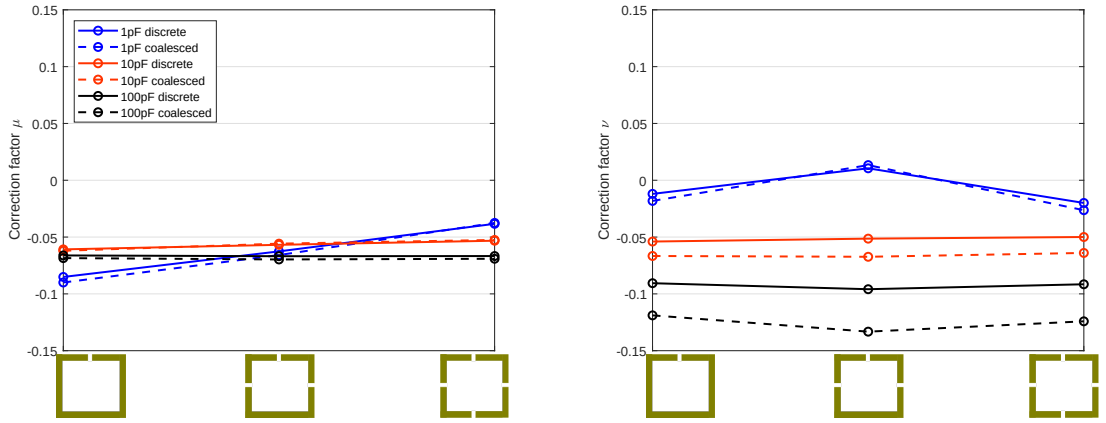
Figure 4.16: Measured (circles) and approximated (blue line) quality factors versus frequency.

summarised in Table 6. They represent the total added resistance shared among all capacitors within the unit cell.

4.3.2 Dimers

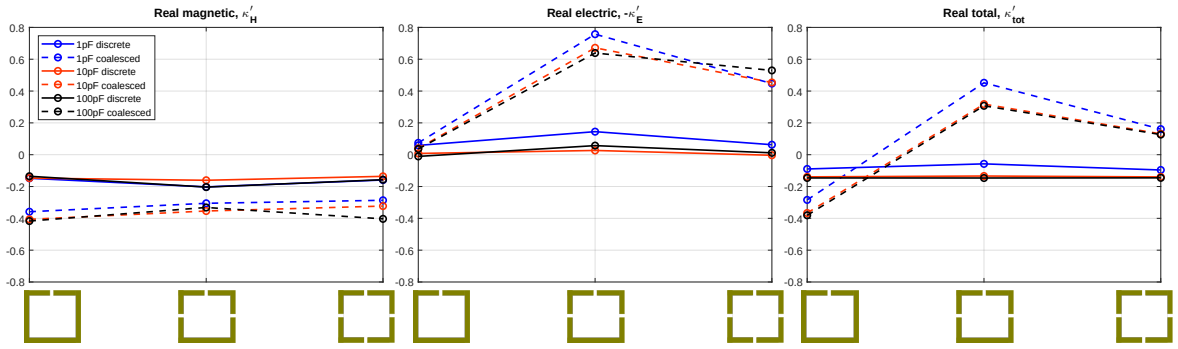
The correction factors for discrete (solid lines) and coalesced (dashed lines) resonators with 100 pF (black), 10 pF (red) and 1 pF (blue) capacitors soldered into the gaps are shown on Fig. 4. 17. The numerical data are not shown because they were in good agreement with the experimental values, and they would make the graphs more complicated. Samples with different capacitors were measured on different days and it was found that variations in the experimental setup, such as probe positions, resulted in a variation of the correction factors. For 100 pF and 10 pF, μ and ν remain relatively constant for different number of gaps, with only a minor difference in their values for the discrete and coalesced cases. The correction factors of the 1 pF case appear to vary with the number of gaps.

The coupling coefficients for discrete (solid lines) and coalesced (dashed lines) resonators with 100 pF (black), 10 pF (red) and 1 pF (blue) capacitors soldered into the gaps are shown in Fig. 4.18. The samples with different capacitors paint a similar picture; when the resonators are coalesced with a capacitor in their shared gap, the electric coupling increases in magnitude, making the total coupling positive. Especially the 100 pF and 10 pF samples are almost identical. For the 1 pF samples, the discrete resonators have a stronger κ_E, which reduces



(a) (b)

Figure 4.17: (a) Correction factors μ, and (b) ν for discrete (solid lines) and coalesced (dashed lines) resonators with 100 pF (black), 10 pF (red) and 1 pF (blue) capacitors soldered into the gaps.



(a) (b) (c)

Figure 4.18: Coupling coefficient (a) κ_H, (b) κ_E, and (c) κ_{tot} for discrete (solid lines) and coalesced (dashed lines) resonators with 100 pF (black), 10 pF (red) and 1 pF (blue) capacitors soldered into the gaps.

their total coupling, while the coalesced resonators have a slightly weaker κ_H but slightly stronger κ_E, resulting in κ_{tot} to be shifted higher.

The imaginary parts of the coupling coefficients were significantly smaller than the real parts, indicating that retardation is practically non-existent. Even though retardation is expected to be more prominent at higher frequencies, the SRRs investigated have a perimeter of 80 mm, which is sufficiently smaller than the wavelength (300 mm) at 1 GHz. Our findings verify the switching behaviour of the total coupling coefficient in higher frequencies as well. This allows for the tunability of the total coupling coefficient over a broad range of frequencies.

4.3.3 Arrays

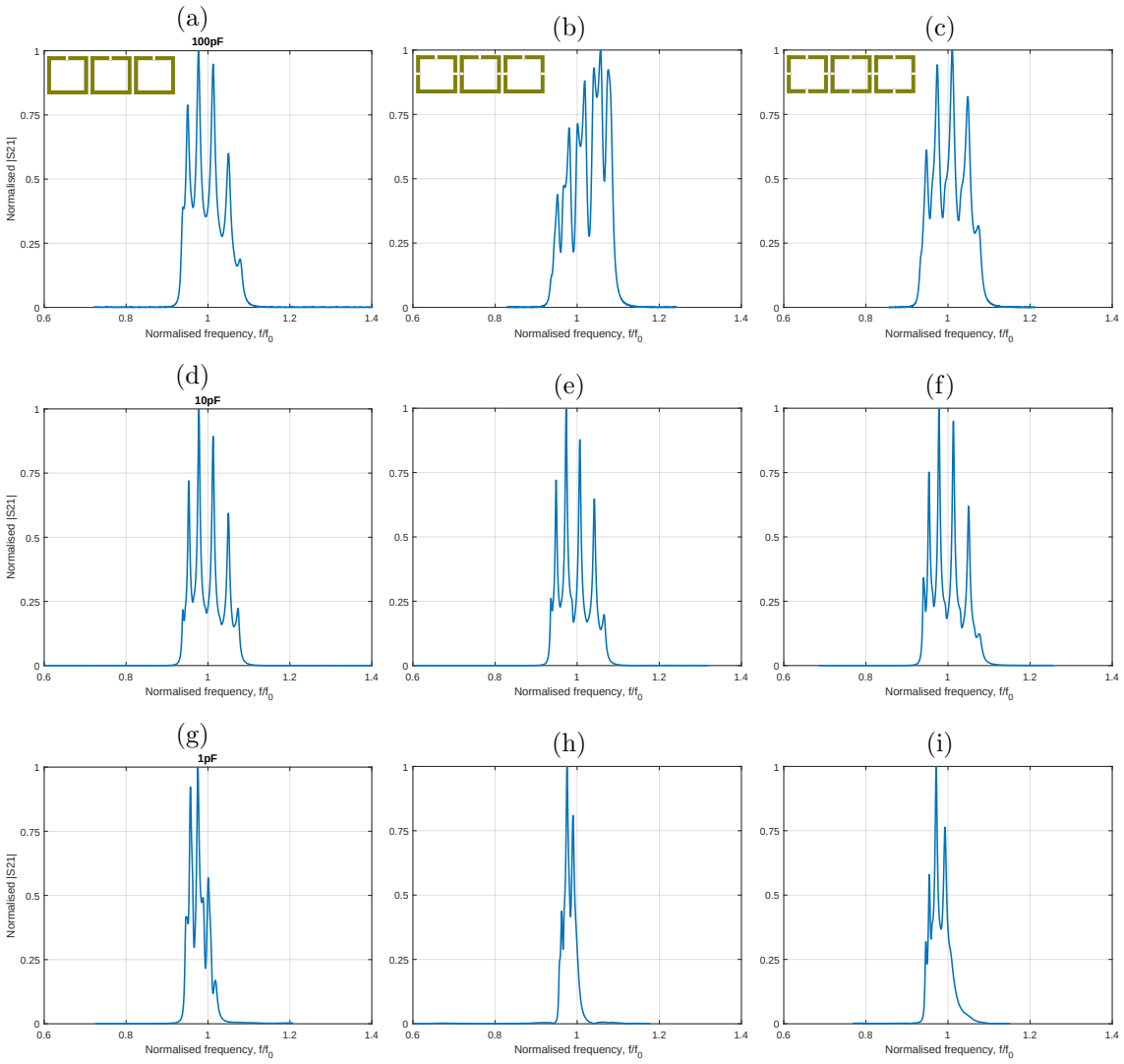


Figure 4.19: Normalised $|S_{21}|$ parameter measured above the 6^{th} element of all discrete arrays for (a)-(c) 100 pF, (d)-(f) 10 pF, and (g)-(i) 1 pF capacitors places at their gaps. On the horizontal axes, the frequency is normalised to the corresponding resonant frequency.

As a final step, we are now able to look at the dispersion for arrays of discrete and coalesced resonators at higher frequencies. The normalised $|S_{21}|$ parameter measured above the 6^{th} element of all discrete arrays are shown in Fig. 4.19. Each row shows data for the same capacitance as the number of gaps increases, with the 100 pF case shown in Figs. 4.19(a)-(c), the 10 pF case shown in Figs. 4.19(d)-(f) and the 1 pF case shown in Figs. 4.19(g)-(i). The

frequency on the horizontal axes is normalised to the corresponding resonant frequency f_0.

As expected from the extracted coupling coefficients, the discrete arrays with 100 pF and 10 pF have a similar-sized band forming around their respective original resonance, as shown in Figs. 4.19(a)-(f). Due to a decrease in the total coupling coefficient, the discrete 1 pF arrays have a smaller band forming for each number of gaps, see Figs. 4.19(g)-(i).

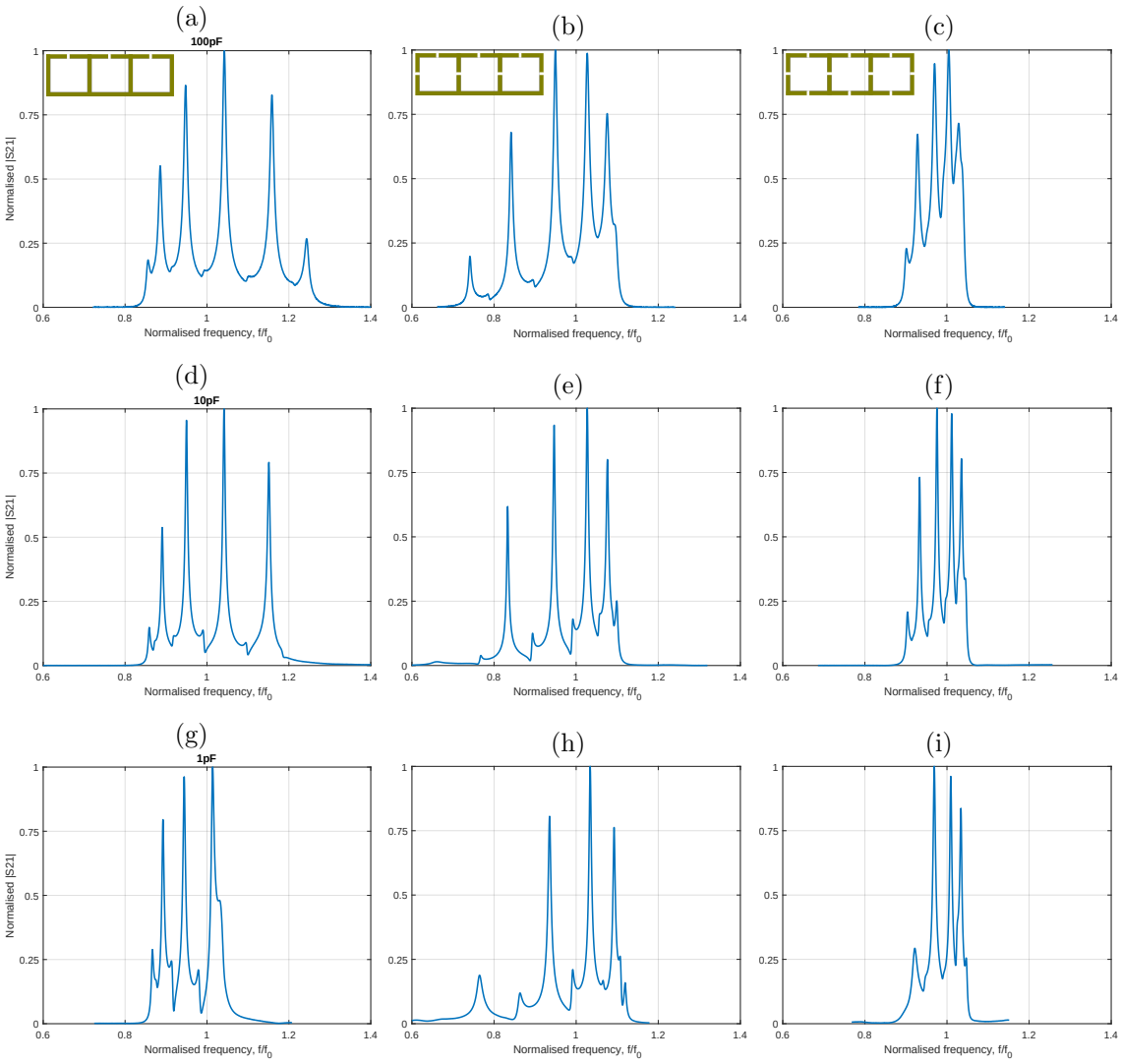


Figure 4.20: Normalised $|S_{21}|$ parameter measured above the 6^{th} element of all coalesced arrays for (a)-(c) 100 pF, (d)-(f) 10 pF, and (g)-(i) 1 pF capacitors places at their gaps. On the horizontal axes, the frequency is normalised to the corresponding resonant frequency.

The corresponding plots for the coalesced cases are shown in Fig. 4.20. The one-gap coalesced arrays have a shrinking band size as the frequency increases, see Figs. 4.20(a),(d)

and (g), which is not the case for the three-gap coalesced arrays, shown in Figs. 4.20(b),(e) and (h). Finally, the four-gap coalesced arrays have a similar band size, see Figs. 4.20(c),(f) and (i). This is expected from the total coupling coefficient κ_{tot} showed in Fig. 4.18(c).

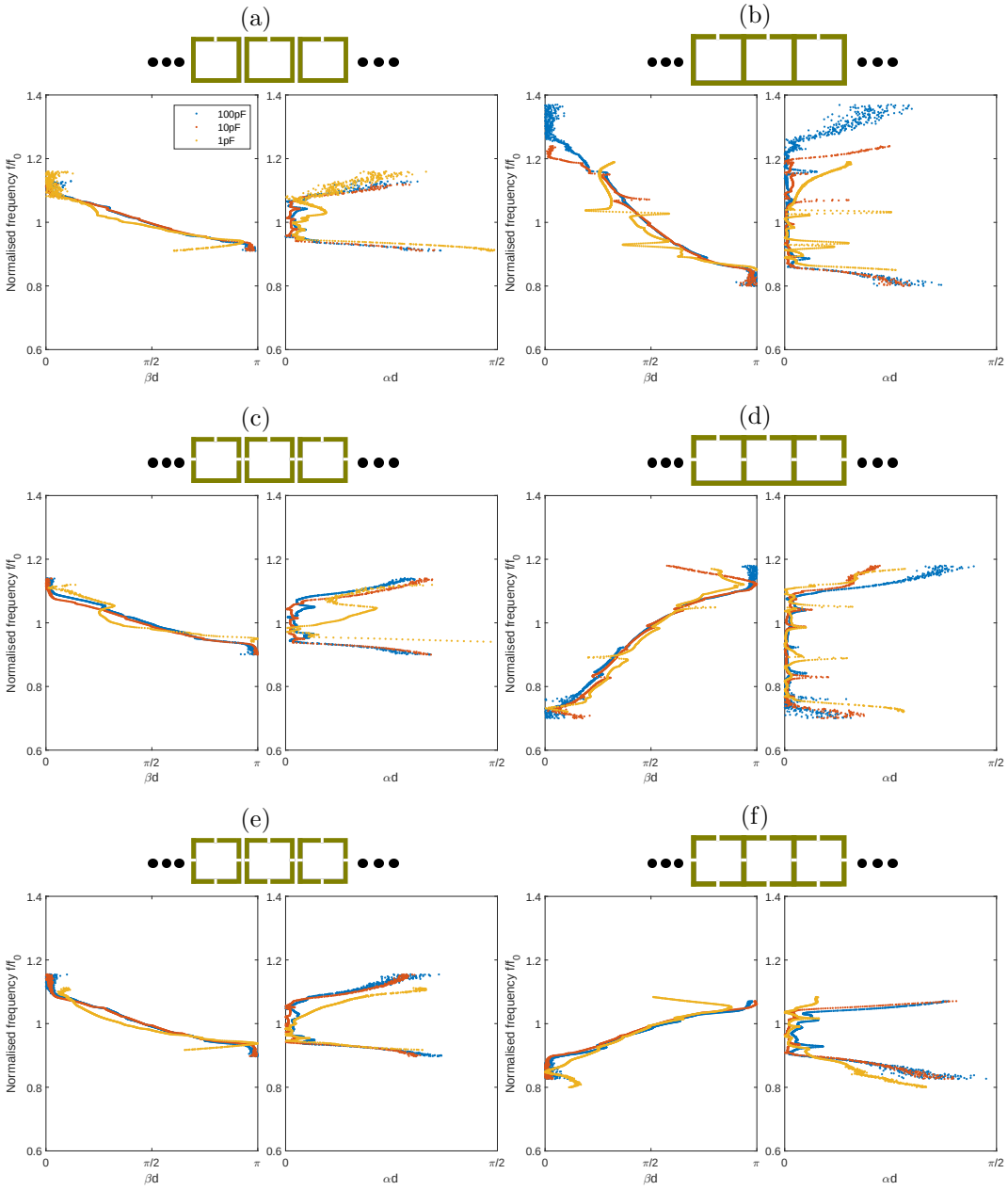


Figure 4.21: Experimental dispersion and attenuation for the (a), (b) One-gap, (c),(d) Three-gap, and (e), (f) Four-gap 11-element arrays with 100 pF (blue dots), 10 pF (red dots) and 1 pF (yellow dots) capacitors in their gaps.

Plotting the dispersion, reveals the switch to forward wave propagation in the three-gap and four-gap coalesced arrays, as shown in Fig. 4. 21. Because the quality factors of the 1 pF samples are significantly smaller, the extracted dispersion plots are scattered more than the 10 pF and 100 pF samples. Overall, it appears that increasing the frequency does not significantly impact the band, which is slightly narrower in the 1 pF samples. The one-gap coalesced array is the exception, where the band size is clearly decreasing as the frequency increases, which was expected from Fig. 4.18(c) showing that κ_{tot} is reduced.

This chapter investigated arrays of discrete and coalesced SRRs over a broad range of frequencies, showing novel ways of controlling the dispersion of MI waves in metamaterials. The circuit theory model formulated in Chapter 2, previously applied on discrete SRRs, is shown to be applicable to metamaterials consisting of coalesced SRRs. The iterative fitting procedure of the simulation parameters proposed in Chapter 3, allowed for CST simulations to match the experimental configurations. Following a detailed parametric study on SRRs in discrete and coalesced arrangements, while varying the number of gaps and the capacitance values, we conclude that the electric coupling due to the capacitive loading of the shared side of the SRRs is responsible for the total coupling coefficient switching to positive values. Across all frequencies studied, in discrete arrangements, it is found that all three coupling coefficients remained practically unaffected by the number of gaps. In coalesced arrangements, the magnetic coupling coefficient is also found to remain effectively constant for all frequencies and number of gaps studied, but the electric coupling coefficient increases as more gaps are added, leading to the sign of the total coupling coefficient to change. As a result, arrays of discrete resonators can only support backward MI waves whereas arrays of coalesced resonators can support both backward and forward MI waves. Our findings show an excellent agreement between the analytical model, numerical simulations and experimental results. Tunable capacitive loading is then proposed as a more practical method of coupling and dispersion control in arrays of coalesced SRRs. It is demonstrated that the total coupling coefficient can be switched over a range of desired values, while maintaining the same resonance frequency. Even though SRRs with a resonance frequency in the GHz regime were studied, it was shown that retardation did not significantly impact the dispersion diagrams due to the electrical size of the SRRs being approximately one quarter of the wavelength at resonance.

Chapter 5
Field's metal fabrication

Chapter 5 demonstrates a novel method for fabricating 3D conductive structures, where fused deposition modelling (FDM) printed dielectric moulds are injected with molten Field's metal, which solidifies afterwards. The method's introduction is followed by a technical evaluation of the various materials that can be used, the resolution of fabricated paths, the conductivity that can be achieved and the fabrication constraints. Coalesced resonators with three gaps are fabricated using this method, whose measurements are compared with the results of the previous chapter. Utilizing the z-axis, 3D spiral resonators with high quality factors have been fabricated. It is demonstrated that the resonance of the spirals can be tuned by the number of turns and the dielectric material used to create the mould. The spirals are then used to construct a 3D metamaterial cube, for which the different couplings present in the structure are investigated. It is also demonstrated that the method can be used to realize 3D circuits with the fabrication of a thermometer device. It is shown that the metal can be formed into a Field's metal filament and loaded on a commercially available 3D pen, marking, to the best of our knowledge, the first proof-of-principle study demonstrating the potential of Field's metal fabrication to be incorporated into standard 3D printing apparatus. Furthermore, the metal can be removed and reused, while the dielectric can be recyclable or biocompostable, paving the path for the development of environmentally friendly 3D devices.

5.1 Materials

Field's metal is an alloy consisting of 32.5% Bismuth, 51% Indium and 16.5% Tin with a melting point of 65^{o}C, a temperature comfortably lower than the processing temperatures of many thermoplastic filaments used in FDM [118], [122]. In theory, 3D printed moulds could be filled with liquid Field's metal for the fabrication of metal-dielectric composite structures. Field's metal has a bulk conductivity of 1.97×10^6 S/m – around 3.3% that of bulk copper. The conductivity and melting temperature of various conductors (blue circles) and solders (red triangles) are shown in Fig. 5.1(a). The conductivity of Field's metal is comparable to that of many silver-based paints, gallium alloys and conductive inks, while it stands higher than that of conductive filaments used in FDM.

As the temperature of thermoplastic filaments is increased, they will transition from a hard and "glassy" state into a viscous or rubbery state [118]. The temperature at which this occurs is called the glass transition temperature, T_G. Due to the material becoming soft, above T_G significant heat deformation can occur, altering the shape of the initial mould. The T_G of PLA, HIPS and ABS are shown with vertical lines in Fig. 5.1(a). While PLA typically is processed at 180^{o}C, its T_G is lower than that.

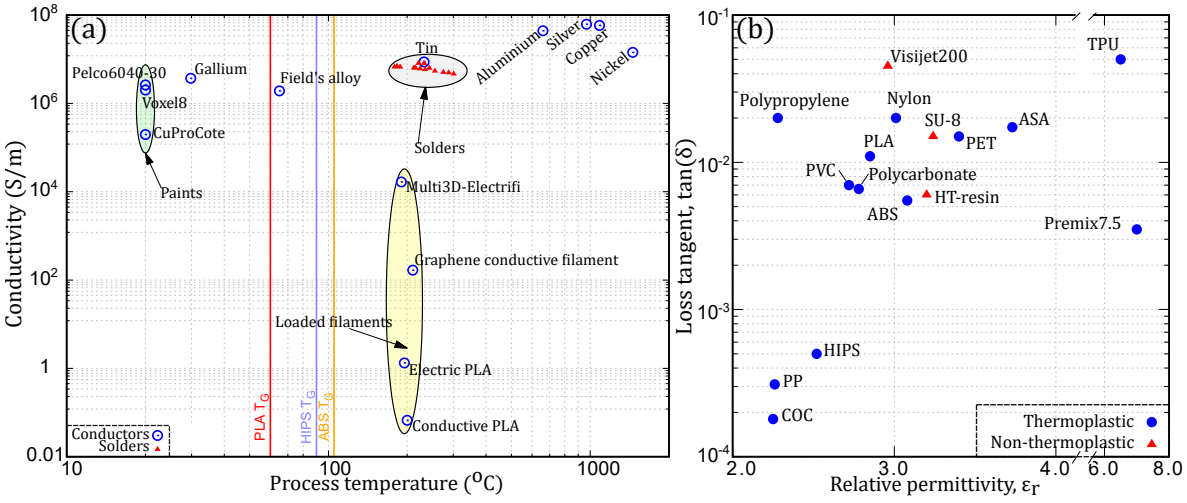


Figure 5.1: (a) Conductivity of various conductors (blue circles) and solder (red triangles) and their melting temperature. The glass transition temperature T_G of PLA, HIPS and ABS are also shown, and (b) Loss tangent tan(δ) and relative permittivity ε_r of various thermoplastics (blue circles) and photosetting (red triangles) resins. Reproduced from Ref. [122]

Table 1: Various low melting conductors [123-125].

Alloy	Bi	Pb	Sn	Cd	In	Ga [%]	Melting point [^{o}C]	Price in €/50 g	Conductivity [MS/m]
Rose's Metal	50	25	25	-	-	-	98	150	-
Wood's metal	50	26.7	13.3	10	-	-	70	40	1.25
Field's metal	32.5	-	16.5	-	51	-	65	70	1.97
EGaIn	-	-	-	-	25	75	15.7	1000	3.3
EGaInSn	-	-	10	-	22	68	-19	350	3.1
Gallium	-	-	-	-	-	100	30	900	3.4

Parameters of some low melting alloys with their chemical composition are summarised on Table 1. All of the listed alloys have a similar conductivity in the order of a few MS/m. The Bismuth-based alloys have a melting point above room temperature and cost roughly the same. However, some of them contain Pb or Cd which are toxic. The Gallium-based conductors have a lower melting point, in some cases lower than room temperature. This requires the conductive parts to be fully enclosed inside the dielectric, which could be less ideal for some applications. Alternatively, if the conductor is not completely enclosed, these structures are quite fragile having a single layer of Gallium oxide surrounding a liquid core which does not solidify at room temperature. At the same time, they are significantly more expensive than the Bismuth-based alloys. Field's metal melting point of 65^{o}C is higher than room temperature and at the same time it is lower than the T_G of many thermoplastic filaments used in FDM. This makes Field's metal thermally compatible with a range of thermoplastics.

Temperature compatibility is important when deciding on the material of the dielectric mould, but there are also the electrical properties to consider. Figure 5.1(b) shows the dielectric properties of various thermoplastics used in FDM (blue circles). Some photosetting resins are also shown (red triangles). From an electromagnetic point of view, the main parameters of interest are the loss tangent $\tan\delta$, quantifying a material's inherent dissipation of electromagnetic energy, and the relative permittivity ε_{r}, which measures the capacity of an insulator to store electric energy in an electrical field. Especially loss tangent is a key parameter for good quality RF systems and ideally should be lower than 10^{-3}. The relative permittivity of the substrate typically affects the operating frequency of a device, meaning

that substrates with higher ε_r enable capabilities for the miniaturisation of devices. It appears that three thermoplastic filaments stand out as potential candidates for their electromagnetic properties: HIPS, PP and COC. For comparison, FR−4, a material widely used in PCBs, has a $\tan\delta$=0.03, which is two order of magnitude greater than that of HIPS.

5.2 Fabrication methods

There are two different methods for fabricating Field's metal structures. The first method involves a heated water bath inside of which the dielectric mould is filled with liquid metal via injection, while the second one uses a custom-made Field's metal filament which is loaded on a commercially available 3D pen. For almost all of the samples fabricated during the work of this thesis, the 3D pen approach was used for the filling unless otherwise specified. In both methods an FDM printer was used to fabricate the dielectric moulds.

5.2.1 3D printer

For printing the dielectric structures a Raise 3D Pro 2 printer fitted with a 0.4 mm nozzle (Raise3D V3 Hardened Steel) was used. HIPS was used for most samples, so the nozzle and bed temperatures were set to 270^{o}C and 100^{o}C, respectively. Other printing parameters include: infill density 100 %, first layer height 0.15 mm, layer height 0.1 mm, extrusion width 0.4 mm, single shell with maximum shells overlap percentage 100 %, coasting distance 0.4 mm, print speed of 20 mm/s, fan speed 50 % and flow rate 101 %. The structures are designed on OpenSCAD and sliced on the slicing software of Raise3D, ideaMaker.

5.2.2 Heated water bath approach

The heated water bath fabrication procedure is shown in Fig. 5.2. First, the desired geometry is designed in any FDM-compatible software. The conductive parts are subtracted to create a dielectric mould with buried microchannels, as shown in Fig. 5.2(a). It is important that the design has two sprue holes, one for the liquid metal to enter and another one to exit, displacing any water or air along the paths. The structure file is then sliced and printed in

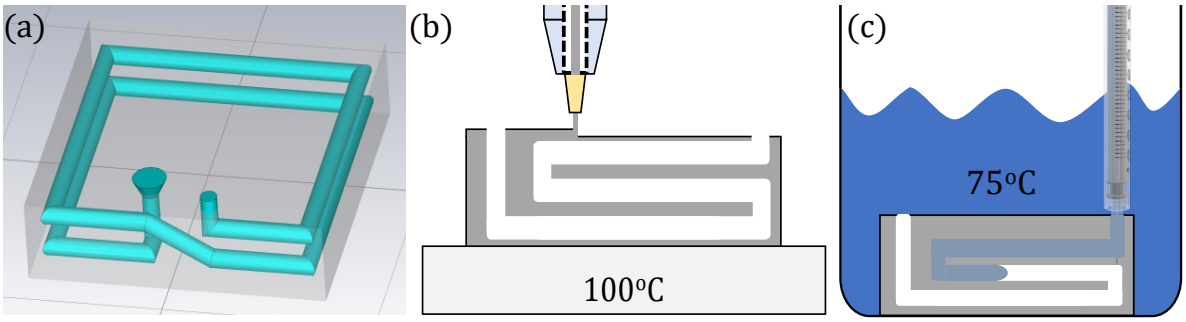


Figure 5.2: Field's metal fabrication method using a heated water bath. (a) The structure is designed with the metal parts subtracted, (b) The design is printed on a FDM printer, and (c) The printed dielectric mould is immersed in a heated water bath along with a syringe containing Field's metal. Once the metal inside the syringe has melted, it can be injected inside the mould. Once filled, the water cools down and the metal solidifies, adopting the shape of the microchannels. Reproduced from Ref. [126].

a layer-by-layer approach, as shown schematically in Fig. 5.2(b). In some cases, the printer bed is heated up to ensure the first layer of the structure sticks on the bed and no warping occurs. After printing, the dielectric mould is immersed in a 75^{o}C water bath along with a syringe containing Field's metal. When the metal inside the syringe has melted, the injection inside the dielectric mould can commence. Figure 5.2(c) shows how the liquid metal follows the path until it reaches the exit sprue hole. Once cooled down, the metal solidifies adopting the architecture of the microchannels. This way 3D complex conductive structures can be fabricated.

5.2.3 3D pen approach

We show that an alternate approach to do the filling is by forming a Field's metal filament which can then be loaded on a 3D pen. Figure 5.3 illustrates the process of creating the filament. A glass beaker containing Field's metal is placed on a hot plate, along with a glass beaker containing water. When the metal has melted, and the water has reached a temperature above 65^oC, a silicone tubing of internal diameter 1.6 mm is placed in the water beaker. The first end of the silicone tubing is placed inside the liquid Field's metal, while the second end is connected with a syringe to create a suction. By pulling on the syringe's plunger, liquid Field's metal will start filling the tubing. With this setup, part of the silicone

tubing is exposed to room temperature air, which poses the danger of the metal solidifying early. In order to minimise the exposure of the tubing with the cool air, aluminium foil is used to cover both beakers. Once the liquid metal inside the tubing has reached the hot water beaker, it will continue flowing until the syringe's plunger stops. While the syringe is still sealed, the now-filled silicone tubing is removed from both beakers and is left to cool in room temperature, as shown in Fig. 5.4(a).

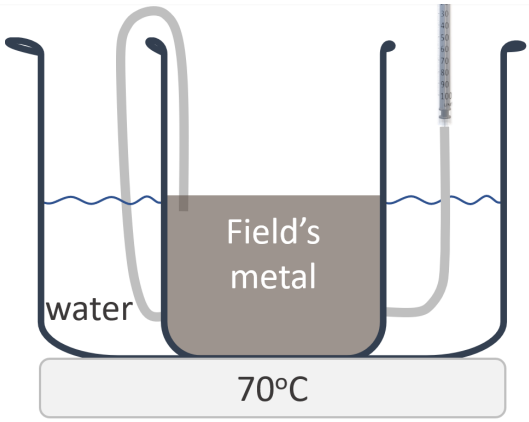


Figure 5.3: Creation of the Field's metal filament. A beaker containing Field's metal is placed in a heated water bath. Using a silicone tubing connected to a syringe, the tubing can be filled with the metal.

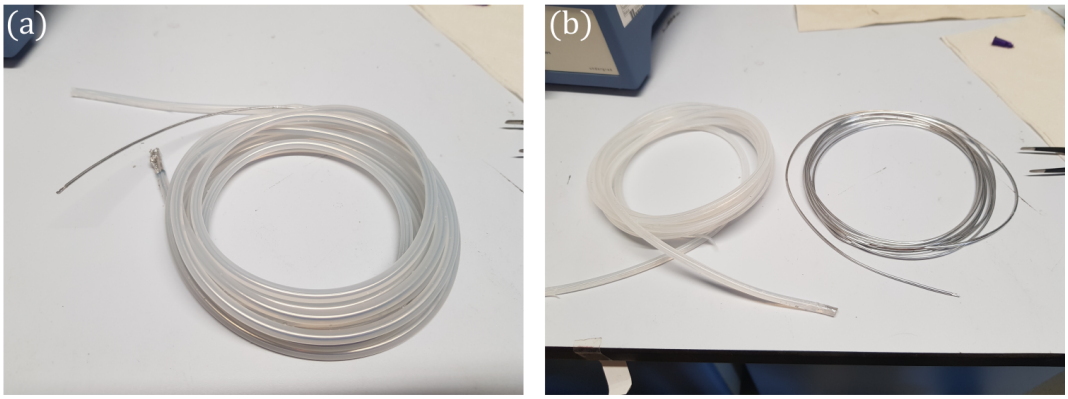


Figure 5.4: Photographs of (a) Filled silicone tubing, and (b) Stripped Field's metal filament. The total length is 3 m.

Once the metal is solidified, the silicone tubing is stripped. The 1.6 mm Field's metal filament is ready for use, see Fig. 5.4(b). The filament is loaded in a commercially available 3D pen (Geeetech TG−21) with adjustable nozzle temperature settings shown in Figure 5.5.

The temperature was set to 90°C, which is high enough to ensure a constant flow of metal, without heat deforming the dielectric mould which comes into direct contact with the nozzle. A hot plate is used to heat the dielectric mould so that the metal remains liquid while filling the paths. Since there is no hot water bath involved now, this makes the filling process faster, simpler and safer. Furthermore, this highlights that the filling process has the potential to be integrated to an FDM printer, thus automating all of the fabrication stages.



Figure 5.5: The Field's metal filament is loaded on a 3D pen which is used to fill a dielectric mould.

5.3 Fabrication characterization

5.3.1 Fabrication resolution

The most straightforward channel to attempt filling is a straight line. What diameter should this path have? Figure 5.6 shows the printed versus the designed diameter of horizontal paths

printed with HIPS. The diameters were measured using a digital microscope (Dino-Lite) and the error bars are associated with measuring the images on the microscope software. For design diameters up to 0.6 mm the paths were fabricated clogged. For 0.8 mm diameters and above, the printed paths are printed thinner than designed, but generally by less than the nozzle diameter, and are quite circular. In this work, paths with a 0.8 mm design diameter were used for the dielectric moulds. This size is the smallest that could be reliably reproduced with the printer and printing parameters used. Also, it matches the available nozzle size of syringes and 3D pens, allowing for leak-free injection.

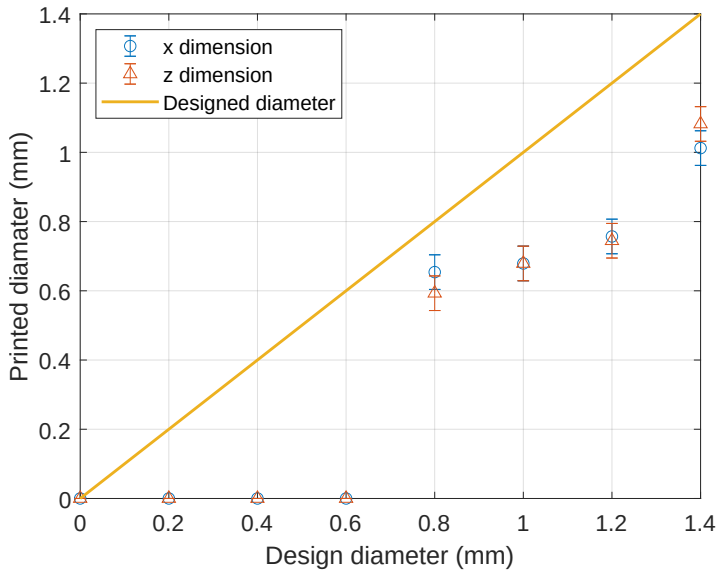


Figure 5.6: Printed versus designed diameter of horizontal paths.

In Fig. 5.7, vertical paths with a height ranging from 0.2 mm to 3 mm are shown. The vertical path diameter is clearly smaller then the horizontal one. As the height of the paths increases, the diameter becomes smaller, until at 3 mm, the vertical paths cannot be reliably printed unclogged. HIPS is a relative difficult material to print with. This is reflected on the larger mismatch between the designed and printed diameter of the horizontal paths, and the limitation in the height of vertical paths. The printing conditions used are the result of various series of optimizations that ensure the paths are printed with no leaks. Even though these conditions are not perfect, they are good enough to reliably fabricate buried channels inside a dielectric medium. A way to improve on the fabrication resolution in both direction

would be to use a smaller diameter nozzle, such as 0.2 mm or 0.1 mm.

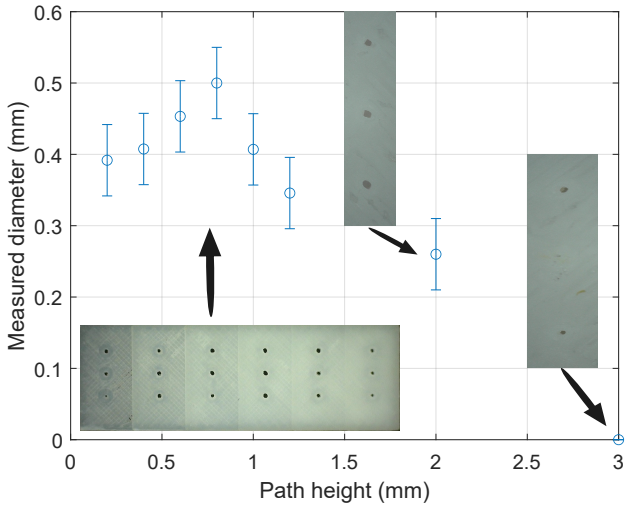


Figure 5.7: Diameter of vertical paths as the length of the paths increases.

5.3.2 Electrical isolation

In order to test that filled paths will be electrically isolated from each other, the design in Fig. 5.8(a) was fabricated using HIPS. Each path is 2.54 mm apart in horizontal and vertical directions. This distance was chosen as it is the standard pin distance in chips. The vertical sprue holes were made conical reaching a final diameter of 1.2 mm, so that they would not get blocked during printing as discussed in the Section 5.3.1. The sample, shown in Fig. 5.8(b), could easily be filled with a 3D pen and by using an ohmmeter it was verified that the paths were continuous and electrically isolated from each other. Reducing the distance between paths in the y and z directions to 1.27 mm makes the filling process harder as the sprue holes are closer together, but still possible. In Fig. 5.8(c), the metal of different sprue holes is in contact, but can be shaved off so that the paths are electrically isolated. At a hole distance of 1 mm, the holes are not separated and filling them is not possible as the 3D pen cannot seal around the sprue hole, as shown in Fig. 5.8(d). If a smaller nozzle is used, the resolution and the spacing of neighbouring holes should reduce, but, for the 0.4 mm nozzle diameter and the 0.8 mm path diameter used here, the holes need to have a spacing of at least 1.27 mm.

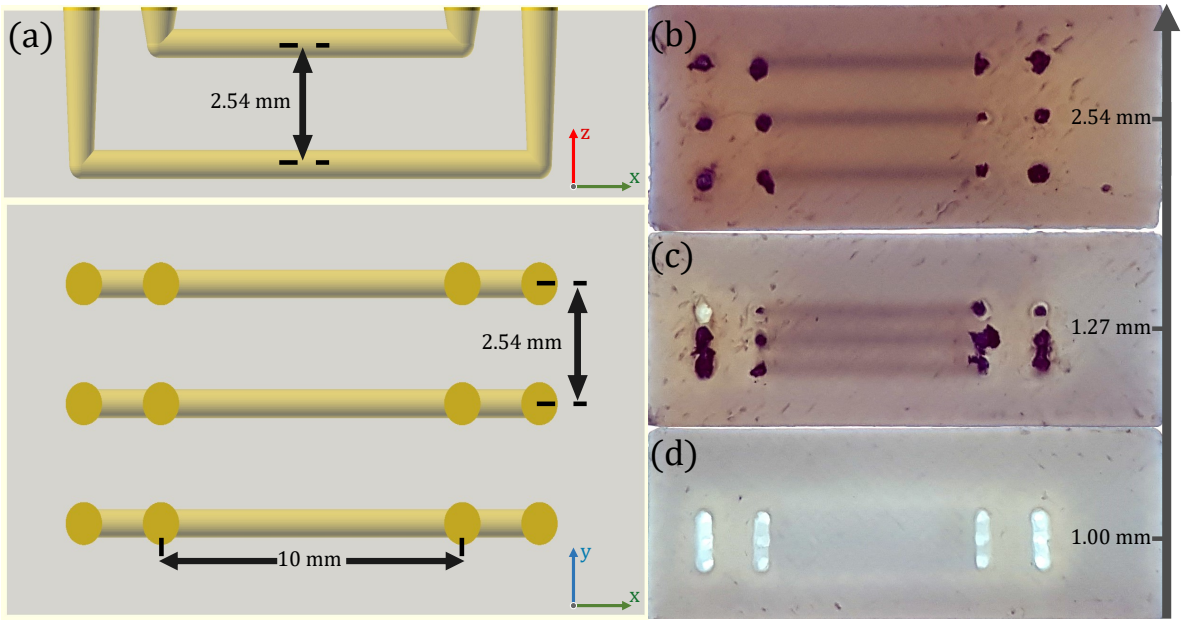


Figure 5.8: (a) Sketch of the designed structure which will test how close the sprue holes can be printed as to not touch each other. Photographs of the samples with (b) 2.54 mm, (c) 1.27 mm, and (d) 1.00 mm hole distance.

If the holes are adequately spaced, how close can the actual paths be? The design in Fig. 5.9(a) has the holes spaced more than 2.54 mm apart, but the horizontal path distance is set to 0.1 mm. The filled sample in Fig. 5.9(b) had continuous paths that do not touch each other. A similar design was used to test the minimum vertical distance of parallel paths, which was also found to be 0.1 mm.

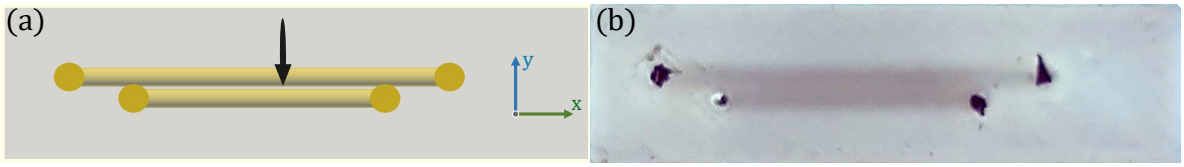


Figure 5.9: (a) Sketch of the designed structure which will test how close the paths can be printed horizontally as to not touch each other, (b) Photograph of sample with a 0.1 mm horizontal distance between paths.

5.3.3 Resistance and conductivity

In order to measure the resistance of the fabricated paths, lines of different length were designed as shown on Fig. 5.10(a). The resistance of the paths was measured with a four

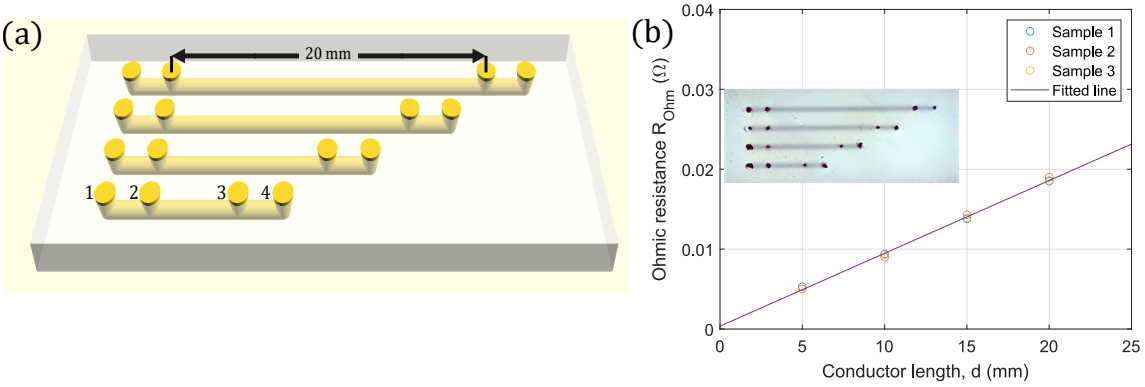


Figure 5.10: (a) Schematic of design for measuring the resistance versus path length using the four point method, and (b) Measured resistance versus path length.

point approach, where a constant current of 0.1 A was applied on points 1 and 4, while the voltage was measured at points 2 and 3. Doing it this way bypasses the contact resistance which would otherwise be present if the resistance was measured directly from two points. The measured resistance versus path length is plotted in Fig. 5.10(b). Three samples as the one shown on the graph's inset were measured. The data points from the different samples are almost identical, meaning that there is a small fabrication error associated with fabricating straight lines. The fitted line passes through all the measured values but does not go through zero. The reason is that the length of the vertical conductor in the sprue holes is not taken into account in the total conductor length, which shifts the measured values slightly to the left. Regardless, the slope of the fitted line in Fig. 5.10(b) can be used to calculate the resistivity ρ (and conductivity σ) using,

$$R = \frac{\rho}{A} d \,, \tag{5.1}$$

where A is the cross-sectional area of the conductive path. From the Section 5.3.1, the paths are shown to be circular with a diameter of 0.6 mm, resulting in a resistivity and conductivity for Field's metal of

$$\rho = 2.7 \cdot 10^{-7}\, \Omega \cdot m \qquad \text{and} \qquad \sigma = 3.6 \cdot 10^{6}\, S/m \,.$$

This is higher than the reported value of 1.97×10^6 S/m for the conductivity of Field's metal. This mismatch could be the result of using a wrong path diameter in Eq. (5.1). As shown in Fig. 5.10(b), for the 0.8 mm design diameter, the printed diameter can be be between $0.5 - 0.7$ mm. Taking this into account, the conductivity for Field's metal is within a range of $2.8 - 5.6$ MS/m, which is still higher than the reported value. There is a lack of a reliable conductivity measurement for Field's metal in the literature. The reported value of 1.97×10^6 S/m cited, originated from one of the manufacturer's data sheet (Alfa Aesar, 500g Field's metal ingot), which has been discontinued. To the best of our knowledge, the value provided in this chapter, is the most accurate measurement for Field's metal conductivity.

Apart from the length, it would be useful to know whether horizontal and vertical turns will have an effect on the resistance. In Fig. 5.11(a), a similar design is shown, having paths with an increasing number of horizontal turns. Each path was designed with a length of 25 mm between points 2 and 3, so only the effect of the turns can be investigated. The resistance versus the number of horizontal turns is plotted on Fig. 5.11(b). The fabrication error is higher in some cases, but remains small overall. Even though all paths were designed to have the same length, the resistance decreases as more horizontal turns are added. Taking a closer look at the filled sample, the metal appears to curve around each corner which reduces the effective conductive path, resulting in a smaller measured resistance.

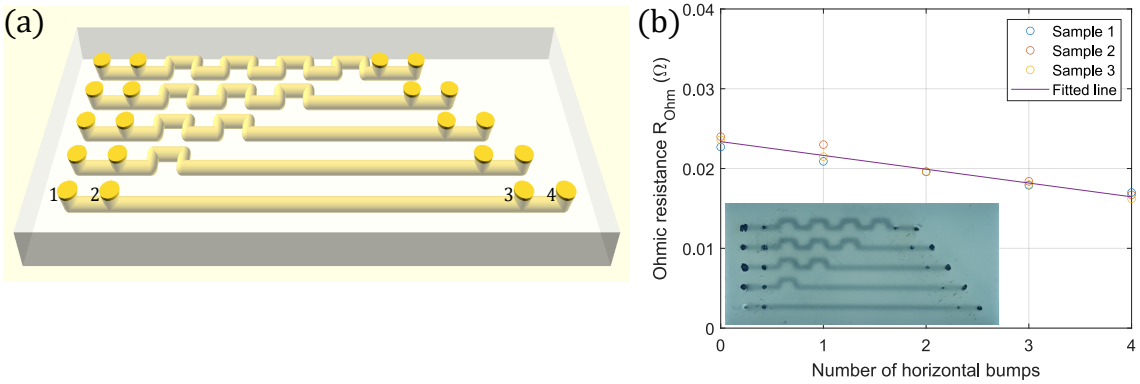


Figure 5.11: (a) Design for measuring the resistance versus number of horizontal turns using the four point method, and (b) Measured resistance versus number of horizontal turns.

The design for measuring the effect of vertical turns is shown in Fig. 5.12(a). Again, each

path was designed with a length of 25 mm between points 2 and 3. The resistance versus the number of vertical turns is plotted on Fig. 5.12(b). The fabrication error is visibly larger in this case, and the resistance appears to remain constant as more vertical turns are added. Since the paths are not as visible in this case, it is not easy to see if the metal curves around the corner here as well. From the fabrication resolution experiments, it follows that vertical paths cannot be printed as accurate as horizontal paths. Possibly, the vertical paths on this structure are printed with a smaller diameter and thus countering the reduction in resistance due to the metal curving around corners.

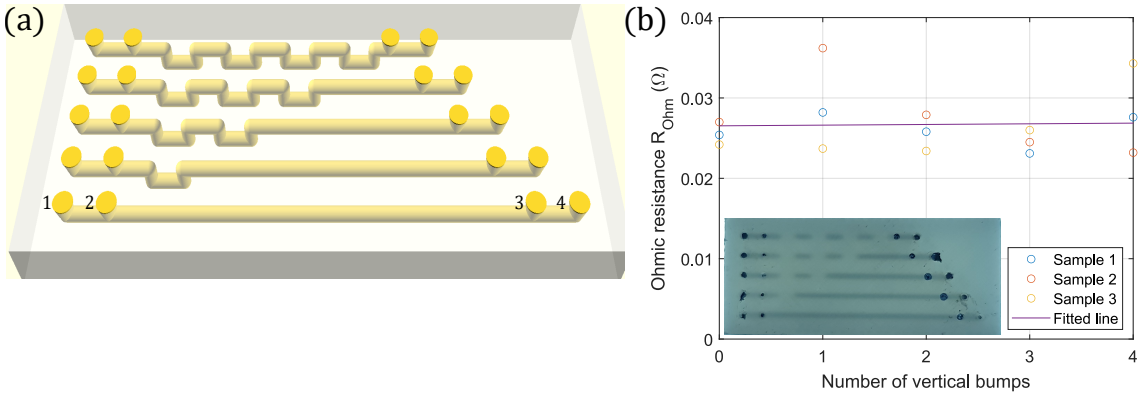


Figure 5.12: (a) Design for measuring the resistance versus number of vertical turns using the four point method, and (b) Measured resistance versus number of vertical turns.

5.4 Coalesced SRRs

In order to make a comparison between the Field's metal method and PCB fabrication, three-gap coalesced resonators were designed and fabricated, see Fig. 5.13. The resonators were designed with a side of 20 mm, track width 0.8 mm and gap size 1 mm. The dimensions are not precisely the same as the PCB samples, but the self-inductance of each SRR should not be too different. CST calculations showed that capacitors of roughly 45 pF need to be placed in the gaps to drive down the resonance frequency closer to that of the corresponding PCB samples. There is no need for soldering because the capacitors can be placed in the gaps while the metal is still liquid.

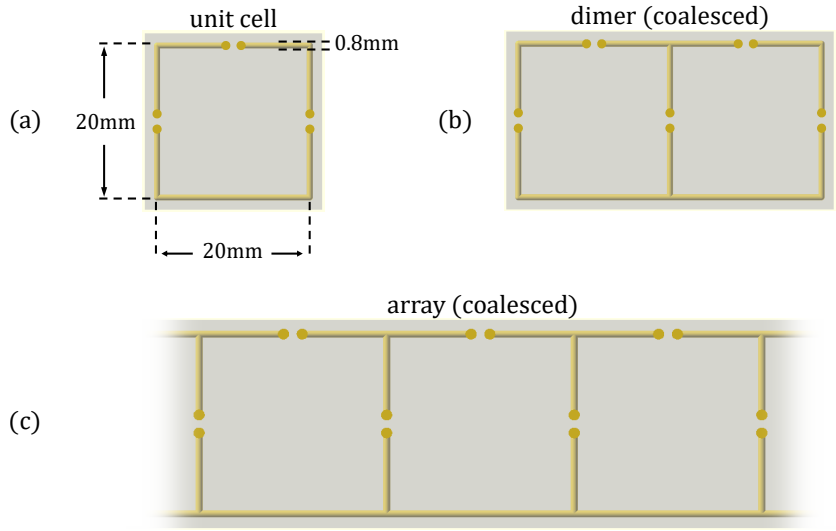


Figure 5.13: The three-gap group of Field's metal samples: (a) The unit cell, (b) Coalesced dimer, and (c) Coalesced 11-element array. Images from OpenSCAD.

The resonance of three unit cell samples was measured in Fig. 5.14(a). One of the filled samples with capacitors is shown in the inset. There is a slight mismatch between the samples associated with the fabrication error, which results in an average resonance of $164 \pm 1\,\mathrm{MHz}$. Similarly, the average quality factor is 70 ± 1, which is lower than the one from the PCB samples.

Three dimer samples were measured in a similar fashion. The normalised $|S_{21}|$ parameter measured above the first element of each dimer is shown in Fig. 5.14(b). As expected there is a frequency mismatch arising here as well. Two of the samples appear to be very close. The correction factors were calculated as $\mu = -0.07$ and $\nu = -0.06$. From the dimer samples, the coupling coefficients were calculated as $\kappa_H = -0.45 - j0.01$, $\kappa_E = -0.68 + j0.03$ and $\kappa_{\mathrm{tot}} = 0.23 + j0.04$. The coupling coefficients are almost identical to their PCB counterparts. Furthermore, the imaginary parts of all coupling coefficients remain small compared to their real parts. The normalised $|S_{21}|$ parameter measured above element 6 of the array shown in Fig. 5.14(c), shows the MI wave bandpass.

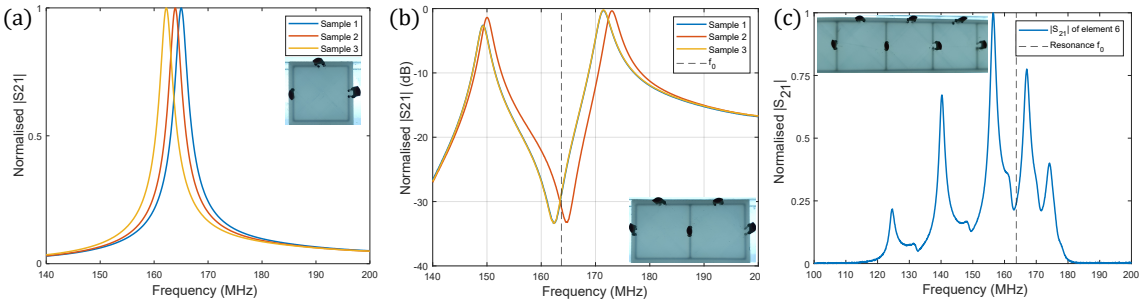


Figure 5.14: Normalised experimental $|S_{21}|$ measurement for (a) Three unit cell samples, (b) Three dimer samples, and (c) Element 6 of the array.

Moving on to the dispersion characteristics, the experimental (blue dots) and the analytical curves (red curve) are shown in Fig. 5.15. For the analytical curve, the experimental $f_{0,\mathrm{fit}}$, Q_{fit}, κ_E and κ_H were used. Both curves show forward wave propagation as expected from the positive total coupling coefficient. The agreement between analytical and experimental data is excellent.

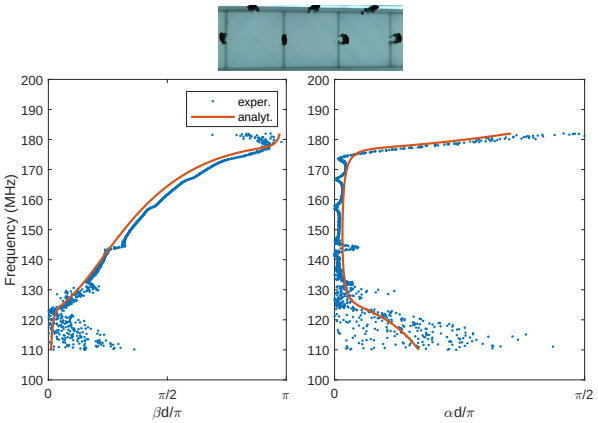


Figure 5.15: Dispersion characteristics $\beta(\omega)$ and $\alpha(\omega)$ for the three-gap Field's metal array. The experimental (blue dots) data were calculated from the currents of three consecutive elements. The analytic model (red line) includes losses and retardation.

5.5 Spiral resonator

The quality factor of the Field's metal SRRs, although quite high, is lower than the one from the PCB samples, mostly owning to the higher resistivity of Field's metal compared to copper. However, the strength of this method lies in its ability to fabricate 3D conductive

structures. Double-turn spiral resonators with the design shown schematically in Fig. 5.16(a) were fabricated. They are square spirals of side 12.85 mm designed with a path diameter 0.8 mm. The diagonal link between turns is rising at an angle of 26.5° to the horizontal plane.

Experiments shown here include spiral resonators fabricated in two different locations: In collaborators' facilities in Loughborough University and in our lab in Oxford. In both cases, the same printer model was used. The two sets of resonators have slight differences in resonance frequency and quality factor, but otherwise had a similar response. It will be specified which group is shown in each section.

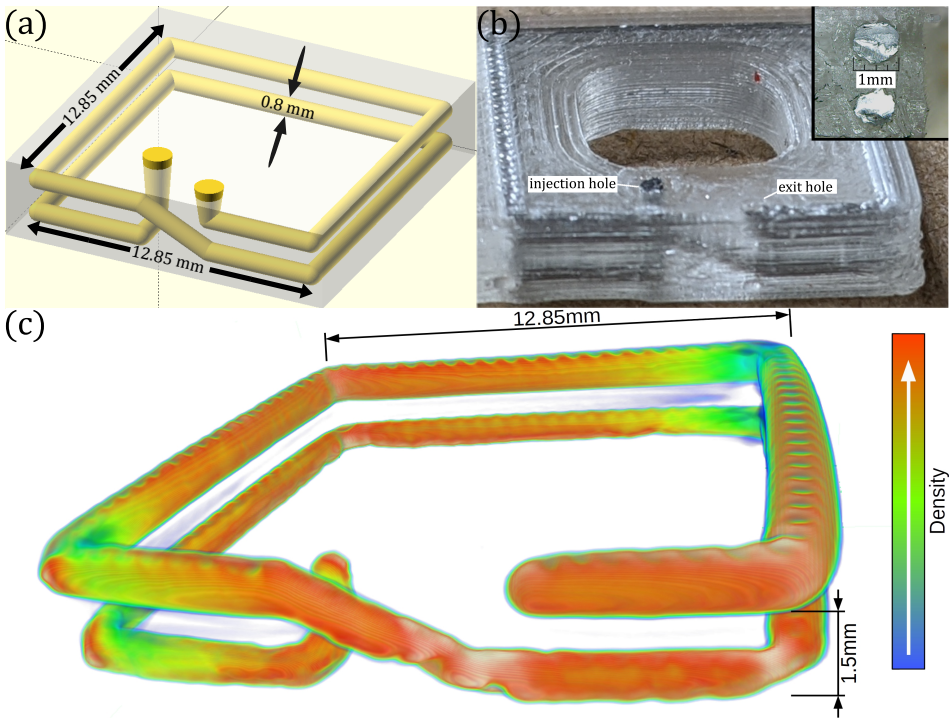


Figure 5.16: (a) Design of spiral resonator with two turns, (b) A filled sample with transparent PLA. The path dimension for only this sample is 1 mm, and (c) XCT image of the metal filled specimen, showcasing the uniformity of the filling. The XCT scan was performed by Dr. Andrew Lui at the Begbroke Science Park. Reproduced from Ref. [122]

5.5.1 Tunability of the resonance

A sample fabricated with transparent PLA (fabricated in Oxford) shown in Fig. 5.16(b) was especially useful in assessing the quality of the filling. This sample was filled using the water

bath approach and its path diameter was 1 mm. The resonator was cut in half to create a cross section. The metal has fully conformed to the shape of the voids and the channels appear to be filled thoroughly. To further investigate the filling quality, the transparent PLA sample was imaged using X-ray computer tomography scan (XCT), as shown in Fig. 5.16(c). Only the metal is shown, because the X-ray absorption contrast with the dielectric is very large, with the colour scale indicating the metal density inside the structure. The tops of the horizontal conductors are corrugated because of the FDM bridging process that lays adjacent cylindrical filaments across a gap to close the top of the tubes. Despite this, the structure is almost identical to the design and the metal has clearly adopted the shape of the paths.

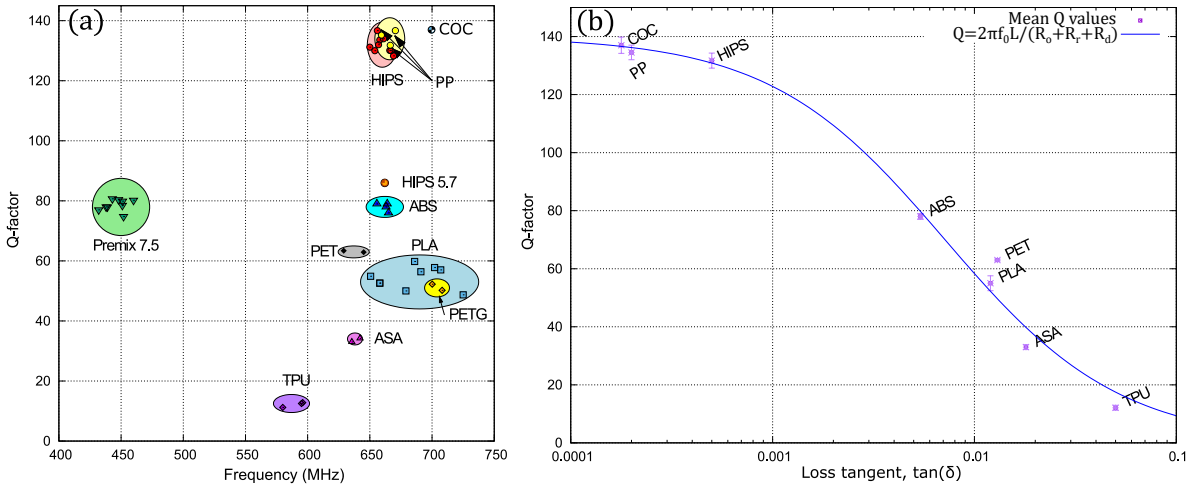


Figure 5.17: (a) Resonance frequency and quality factor of the measured spiral resonators fabricated with different FDM materials, and b) Measured quality factors versus loss tangents of the used materials. Reproduced from Ref. [122].

The resonance of the spirals relies on the capacitance between the parallel paths of consecutive layers. Naturally, the dielectric material in-between will impact both f_0 and Q because of its ε_r and $\tan\delta$. Figure 5.17(a) shows the measured f_0 and Q of spirals using different FDM materials for the dielectric bodies (fabricated in Loughborough, measured in Loughborough). The printing conditions were kept the same for all filaments except for the nozzle and bed temperatures which had to be adjusted and the metal filling was performed with the heated water bath approach. For each material, many samples were prepared to show the real production performance of the technique. Materials with fewer data points imply that

this material was hard to print with and samples were printed with blocked paths. In some cases, there was only one successfully filled sample e.g COC.

As expected from the materials' losses in Fig. 5.1(b), spirals made with HIPS, PP and COC have the highest quality factors. Data from samples made with PLA, one of the most common FDM filaments, are quite scattered, mainly due to the lower T_G of the material, which results in warping and deformation during the filling process. ABS samples, which is another very popular filament, even though more consistent, only achieved quality factors of below 80.

The average quality factor for each material is plotted versus that material's $\tan\delta$ in Fig. 5. 17(b). For the spiral resonators, Q can be modelled as

$$Q = \frac{2\pi f_0 L}{R_{\text{ohm}} + R_{\text{rad}} + R_{\text{diel}}}\,, \tag{5.2}$$

where L is the self inductance of the resonator, and R_{ohm}, R_{rad}, R_{diel} are the ohmic, dielectric and radiative resistances. Using the helical coil approximation L=103 nH and assuming that at resonance

$$R_{\text{diel}} = 2\pi f_0 L \tan\delta\,, \tag{5.3}$$

Eq. (5.2) can be fitted to the experimental data by varying $R_{\text{ohm}} + R_{\text{rad}}$, giving a combined resistance for ohmic and radiative losses of $\sim 3\,\Omega$. By considering the geometry of the structure and the published properties of Field's metal, R_{ohm}=1.26 Ω accounting for the skin effect and R_{rad}=0.08 Ω using the small loop antenna approximation at ∼660 MHz, which are half of what was expected from the fitting. As shown in the XCT scan in Fig. 5.16(c), the metal path is corrugated due to the FDM printing. This surface roughness was not taken into account when approximating the resistance, but it will inevitably make it larger.

Even though spirals made with COC and PP have the highest Q, many of the printed samples were fabricated clogged. Taking the printing reliability into account, HIPS comes out on top as the most suitable material for Field's metal fabrication, as it offers low dielectric losses, relative easy fabrication process and good repeatability.

Apart from the dielectric material, the resonance can also be tuned by the number of turns in the same spiral. The normalised $|S_{21}|$ parameter for HIPS spirals with a number of turns ranging from two (blue line) to five (purple line) is shown in Fig. 5.18 (fabricated in Oxford). The measured resonance of the spirals versus the number of turns is shown on Fig. 5.19(a). For each turn number, three samples were fabricated and measured. The f_0 from different samples is very consistent and decreases as the number of turns increase. The quality factor shown in Fig. 5.19(b) has a similar behaviour but varies more between different samples. Regardless, the resonators have quite high Q factors.

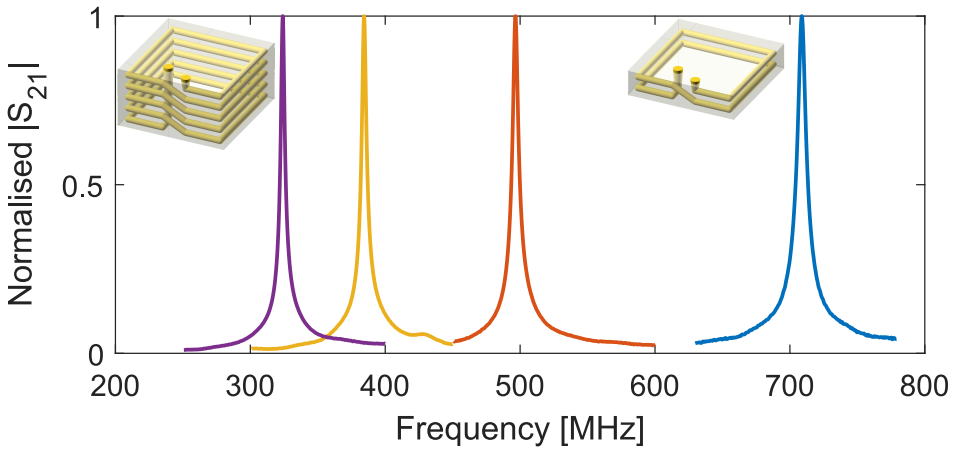


Figure 5.18: Normalised $|S_{21}|$ parameter of HIPS spiral resonators with a number of turns between two (blue) to five (purple).

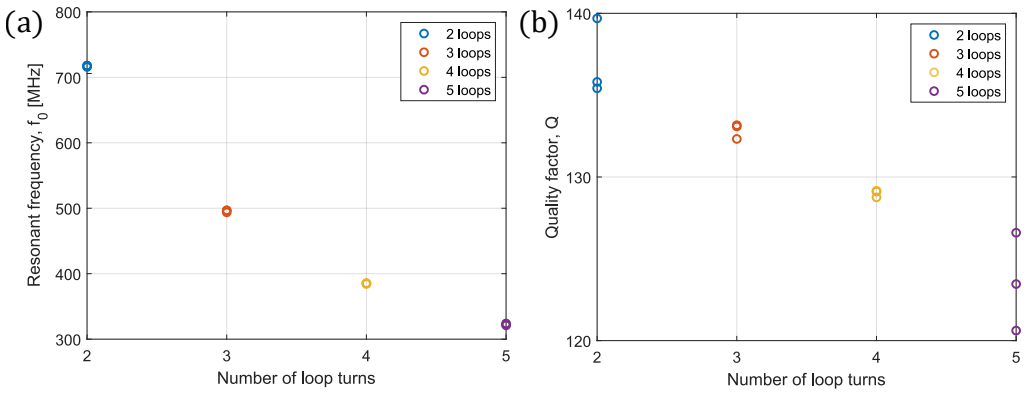


Figure 5.19: (a) Resonance, and (b) Quality factor of spirals with different number of turns.

5.5.2 Coupling coefficients

The spiral resonators are not symmetric because of the sprue holes, therefore the coupling between two of them will depend on their orientation to some extend. To investigate this, spirals with two turns were measured while the angle of each one is rotated by 90^o (fabricated in Oxford). As shown in Fig. 5.20(a), θ and φ are the rotation angles of the first and second spirals respectively, with both of them being at 0^o in the image. The normalised $|S_{21}|$ parameter of one spiral as it is rotated is shown in Fig. 5.20(b). Due to change of the relative position between the excitation/measuring loop and the resonator, the resonant frequency varies with θ.

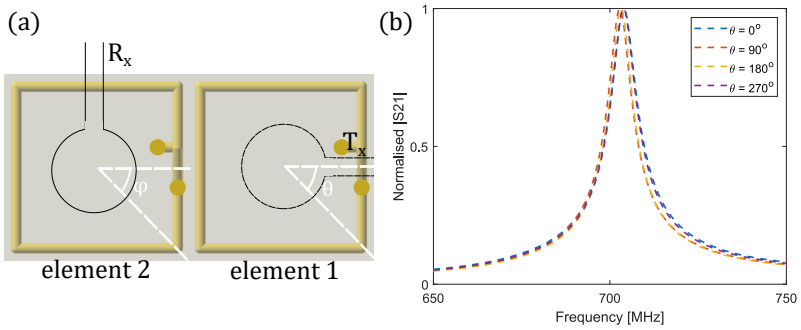


Figure 5.20: (a) Measurement setup for investigating the effect of the spirals' orientation relative to the excitation loop. Angle θ is for the first spiral and angle φ is for the second spiral. The excitation loop (T_x) excites element 1 below its center while the measuring loop (R_x) records the magnetic field above the center of each resonator, and (b) Normalised $|S_{21}|$ parameter of single spiral resonators rotated at different angles θ.

The effect of the orientation is more pronounced in the resonance split of dimer samples, see Fig. 5.21. In most cases the different angles of the spirals result in small variations in the separation of the peaks, and, by extension, to the total coupling. However, when $\theta = 180^o$ and $\varphi = 0^o$ the total coupling is visibly lower as shown with the blue curve in Fig. 5.21(c). At this particular orientation the two spirals have their sprue holes next to each other, which has a big impact to the total coupling.

Since the correction factors measure the additional interaction between the loop antennas and the resonators, they can be expected to vary depending on the angles θ and φ. The correction factor μ is shown on Fig. 5.22(a), where angle θ does not affect μ that much. The

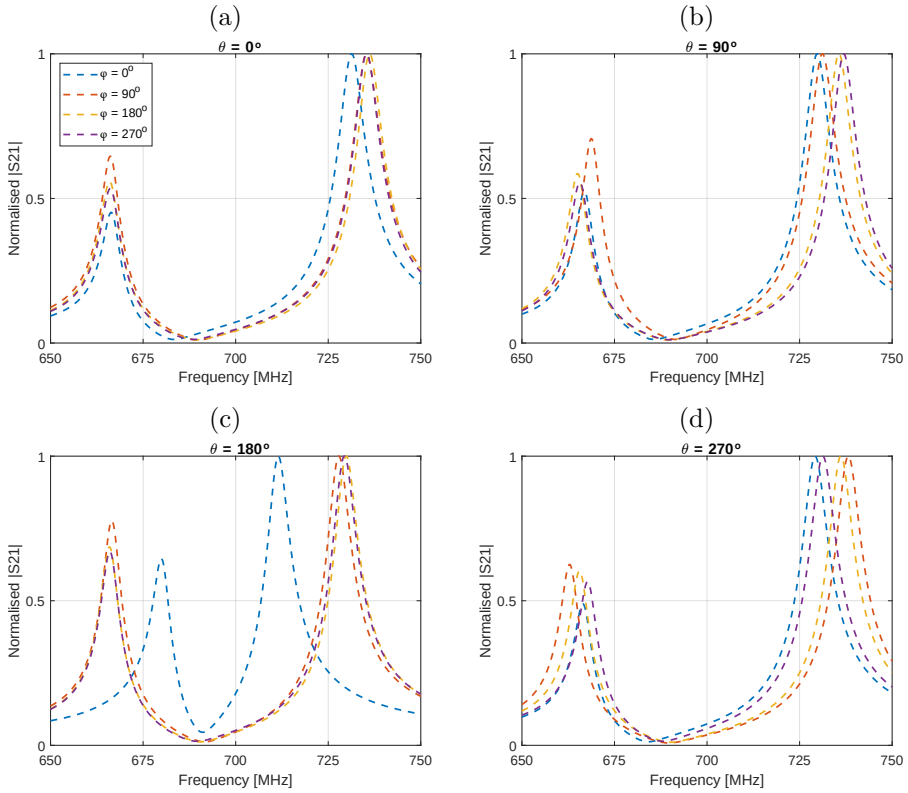


Figure 5.21: Normalised $|S_{21}|$ parameter of dimers at θ = (a) 0^o, (b) 90^o, (c) 180^o, and (d) 270^o for different values of φ.

angle of the second resonator φ has a bigger impact on μ, which is not surprising since μ measures the unwanted excitation of element 2. At $\varphi = 270^o$, μ is the largest. The correction factor ν paints a similar picture on Fig. 5.22(b), but is affected less from θ and φ.

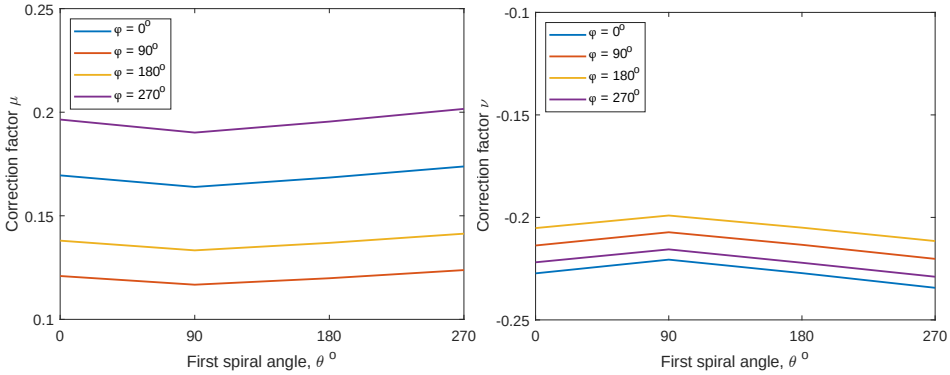
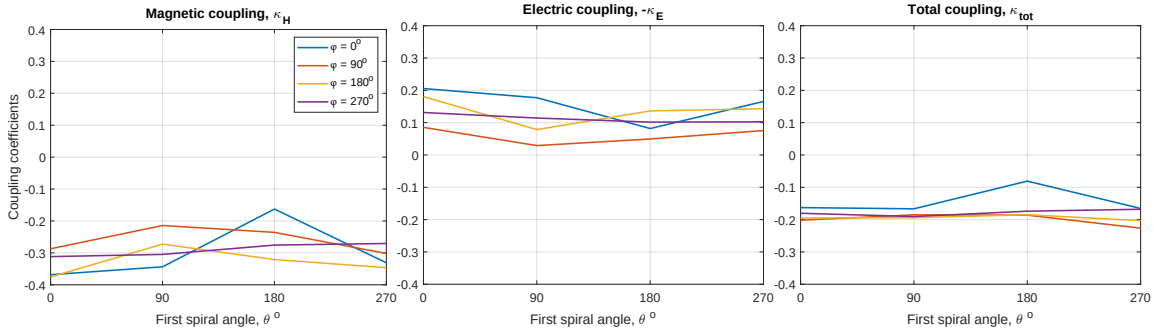


Figure 5.22: Correction factor (a) μ, and (b) ν as the angles of both resonators change.

Using the correction factors at different angles, the coupling coefficients can be calculated. In general, the magnetic coupling coefficient κ_H is always negative as shown in Fig. 5.23(a), while the electric coupling coefficient $-\kappa_E$ is always positive and smaller than κ_H as shown in Fig. 5.23(b). The total coupling coefficient κ_{tot} is always negative as shown on Fig. 5.23(c). It is on average -0.18, except for the case of $\theta = 180^o$ and $\varphi = 0^o$, where it drops to around -0.08, as expected from the resonance split on Fig. 5.21. This is due to a reduction in the magnetic coupling κ_H as shown on Fig. 5.23(a). The difference in these two couplings is big enough, so that if the spirals are oriented accordingly, a planar array could act as a diatomic chain, having both couplings present at the same time.



(a) (b) (c)

Figure 5.23: (a) Magnetic, (b) Electric, and (c) Total coupling coefficients for the different angles between the spirals.

Next, we shall retrieve the currents of both elements using the impedance matrix theory from Chapter 2. The impedance matrix for a two-element setup can be written as

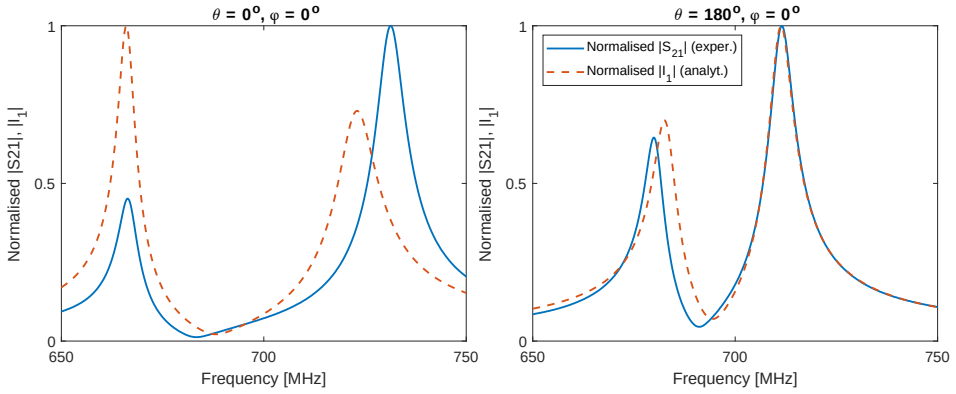
$$Z = \begin{bmatrix} Z_0 & Z_M \\ Z_M & Z_0 \end{bmatrix} = \frac{1}{2} j\omega L \begin{bmatrix} 2\left(1 - \frac{\omega_0^2}{\omega^2} - j\frac{\omega_0}{Q\omega}\right) & \left(\kappa_H - \frac{\omega_0^2}{\omega^2}\kappa_E\right) \\ \left(\kappa_H - \frac{\omega_0^2}{\omega^2}\kappa_E\right) & 2\left(1 - \frac{\omega_0^2}{\omega^2} - j\frac{\omega_0}{Q\omega}\right) \end{bmatrix}, \tag{5.4}$$

where Z_0 is the impedance of a single resonator and Z_M is the coupling term containing the magnetic and electric couplings. The resonance frequency, quality factor and coupling coefficients measured experimentally for each orientation are used. Assuming that the first

element is excited with a voltage V_1, the second element is also excited with a voltage μV_1

$$V = V_1 \begin{bmatrix} 1 \\ \mu \end{bmatrix}, \tag{5.5}$$

where the correction factor μ has been measured for all orientation of the spirals, see Fig. 5. 22(a).



(a) (b)

Figure 5.24: Normalised $|S_{21}|$ parameter and current $|I_1|$ of the first spiral in a two-element setup at (a) $\theta = 0^o$ and $\varphi = 0^o$, and (b) $\theta = 180^o$ and $\varphi = 0^o$.

Using the V vector and the Z matrix, the currents in both elements can be calculated analytically. The normalised experimental $|S_{21}|$ parameter and the analytical $|I_1|$ current of the first spiral for $\theta = 0^o$ and $\varphi = 0^o$ is shown on Fig. 5. 24(a). The resonance split of the analytical current is smaller than the experimental one, meaning that the extracted coupling which was used in Z is slightly underestimated. A similar situation can be observed for $\theta = 180^o$ and $\varphi = 0^o$ as shown on Fig. 5.24(b). It appears that the extraction method is not as accurate here as it is for the PCB samples studied in Chapter 4. The extracted method is based on circuit theory, which is very accurate when the electrical size of the unit cell is significantly smaller than the wavelength at resonance. However, the spirals have a conductor length of approximately 100 mm which is comparable with the wavelength at resonance (700 MHz, 430 mm). This could result in the currents not being homogeneous, which is an assumption the circuit model as well as the extraction method is based on. Also,

the spirals are different than the PCB samples because the conductor is encapsulated inside the dielectric. The analytic model may need to be adjusted to take that into account. In the future, this could be investigated by replicating the experimental results using CST. This would show whether the analytic model is accurate or not.

5.5.3 Spiral cube

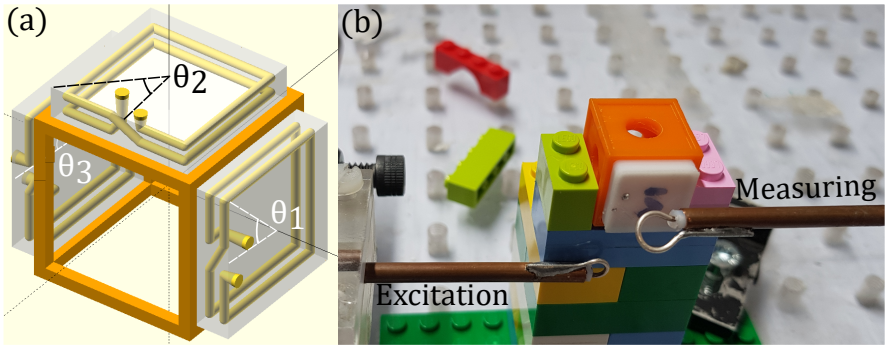


Figure 5.25: (a) The fabricated 3D metamaterial cube fitted with spiral resonators, and (b) Measurement setup of the cube. Instead of exciting the first resonator axially as in the previous experiments, the excitation loop antenna was placed diagonally on the same plane of the first resonator as shown. The measuring loop antenna recorded the magnetic field above the center of each resonator.

Using FDM enables the fabrication of 3D metamaterial unit cells. As was discussed in Chapter 1, cubic resonators show a degree of degeneration to their eigenvalues, defined by the symmetries and orientation of the its comprising resonators [79], [80]. It is particularly interesting to investigate such structures and study the different couplings that are present. Using the spirals, a 3D cubic resonator was fabricated, see Fig. 5.25(a). There should be two types of coupling coefficients in the structure: negative between the orthogonal spirals on the adjacent sides of the cube (e.g 1 and 2) and positive between the axial spirals on the opposite sides of the cube (e.g 1 and 3). In order to be able to measure the coupling coefficients present on the cube, a cubic mould made with orange PLA was printed, where the spirals could be wedged in and out. This way any arrangement of spirals could be measured, including the one with two orthogonal or two axial spirals for extracting the coupling coefficients. The measurement setup is shown on Fig. 5.25(b). If the excitation loop antenna is placed below

the center of the first resonator, it would also excite the other elements. To avoid that, the excitation loop was placed diagonally of the first resonator, as shown in Fig. 5.25(b). The measuring loop antenna recorded the magnetic field above the center of each resonator but was tilted at a 45^o angle along its axes. That way it would interact with the magnetic field of both vertical and horizontal resonators without the need to be rotated. With a point of view above each spiral, the rotations are performed clockwise.

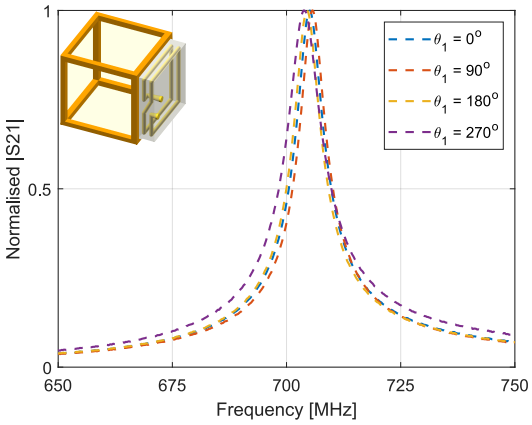


Figure 5.26: Normalised $|S_{21}|$ parameter of the cube with a single spiral as angle θ_1 changes.

The resonance of the cube fitted with a single spiral as θ_1 changes is shown on Fig. 5.26. Similarly to the planar case in the previous section, the resonance slightly shifts due to the interaction interaction of the spirals with the loop antennas.

The normalised $|S_{21}|$ parameters in the orthogonal arrangement for all angles θ_1 and θ_2 are shown in Fig. 5.27. All orientations have a similarly sized resonance split, except for the case of θ_1=90^{o}C and θ_2=270^{o}C where it is slightly reduced. In this arrangement the sprue holes are facing each other. However, the reduction is not as prominent as in the planar arrangement. The resonance split in the axial arrangement Fig. 5.28 is smaller and mostly unaffected as θ_1 and θ_3 change, which is not surprising given that the resonators are further away from each other.

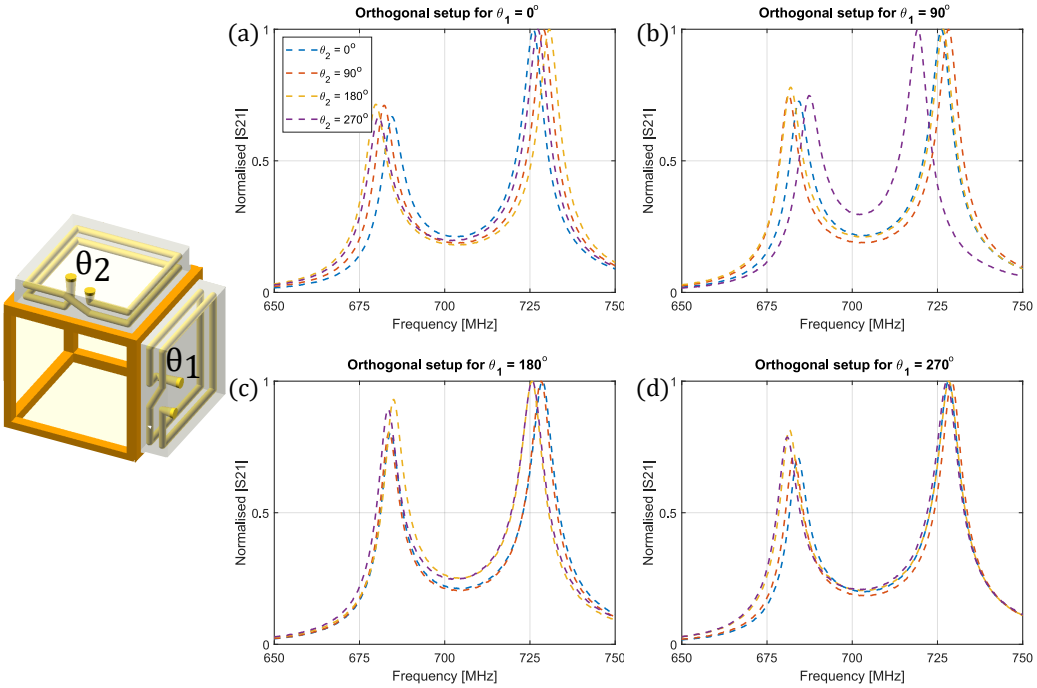


Figure 5.27: Normalised $|S_{21}|$ parameter of the cube with two spirals in the orthogonal setup at (a) θ_1=0^{o}C, (b) θ_1=90^{o}C, (c) θ_1=180^{o}C, and (d) θ_1=270^{o}C as angle θ_2 changes.

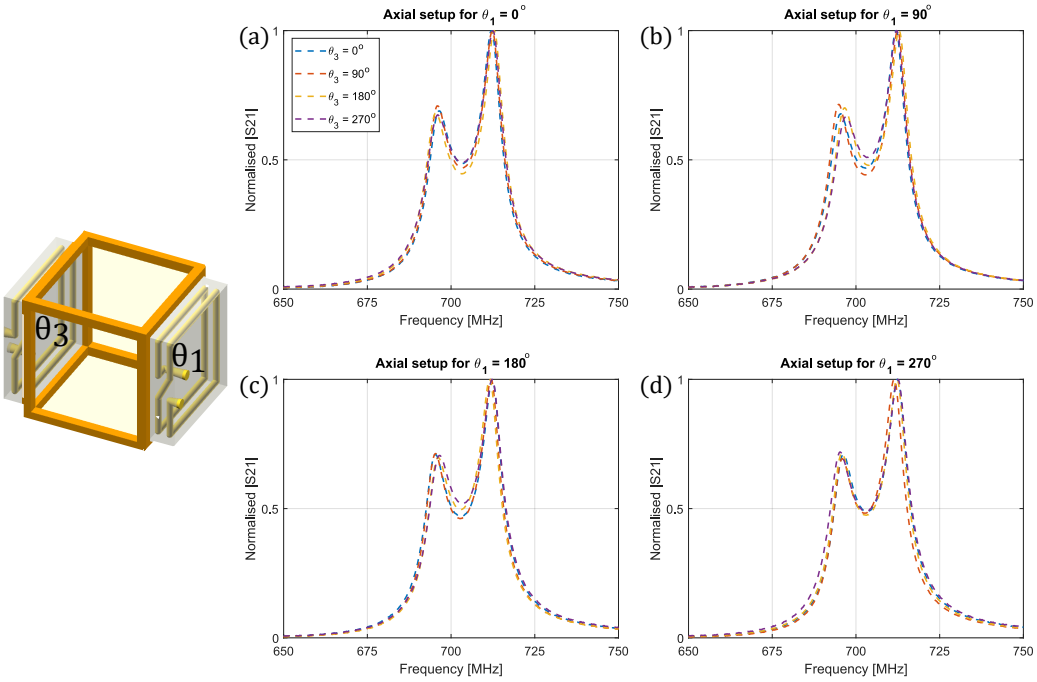


Figure 5.28: Normalised $|S_{21}|$ parameter of the cube with two spirals in the axial setup at (a) θ_1=0^{o}C, (b) θ_1=90^{o}C, (c) θ_1=180^{o}C, and (d) θ_1=270^{o}C as angle θ_3 changes.

The correction factors of the orthogonal (μ_1, ν_1) and axial (μ_2, ν_2) setups are shown in Fig. 5.29. All correction factors vary slightly with the spiral angles. On the orthogonal setup, μ_1 and ν_1 are larger since the spirals are closer to each other and by extension to the magnetic loops. The correction factors between orthogonal and axial setups have opposite signs, due to their relative position with respect to the excitation and measuring loop antennas.

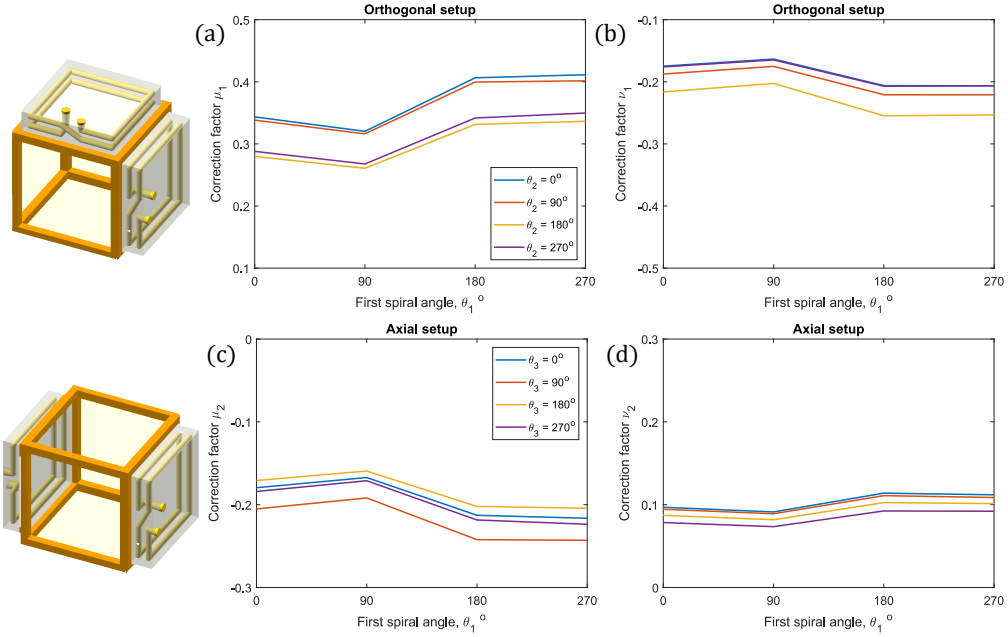


Figure 5.29: Correction factors for the (a), (b) Orthogonal setup, and (c), (d) Axial setup as the angle of the second spiral varies.

The coupling coefficients for the orthogonal (κ_H^1, $-\kappa_E^1$, κ_{tot}^1) and axial (κ_H^2, $-\kappa_E^2$, κ_{tot}^2) setups are shown on Fig. 5. 30. As expected the total coupling in the orthogonal setup is negative, while it is positive for the axial setup. In Fig. 5.30(c), κ_{tot}^1 varies slightly with the angles θ_1 and θ_2 but for almost all orientations it is around -0.2, which, curiously, is the same for the planar spirals setup. However, the resonance split in the orthogonal setup is 45 MHz, clearly smaller than the 60 MHz split in the planar setup. The extraction method is not as trustworthy in this case. The axial total coupling coefficient κ_{tot}^2 does not fluctuate as much with θ_1 and θ_3 and is roughly 0.07, which is not surprising given the larger distance between the spirals.

Looking at a comparison of the experimental $|S_{21}|$ parameter and analytical $|I_1|$ current

on Fig. 5.31, the extracted coupling coefficients are higher than their actual values, because the resonance split from the impedance matrix model is larger than in the experiment. The insets of the cube show whether the spirals are in the orthogonal or in the axial arrangement.

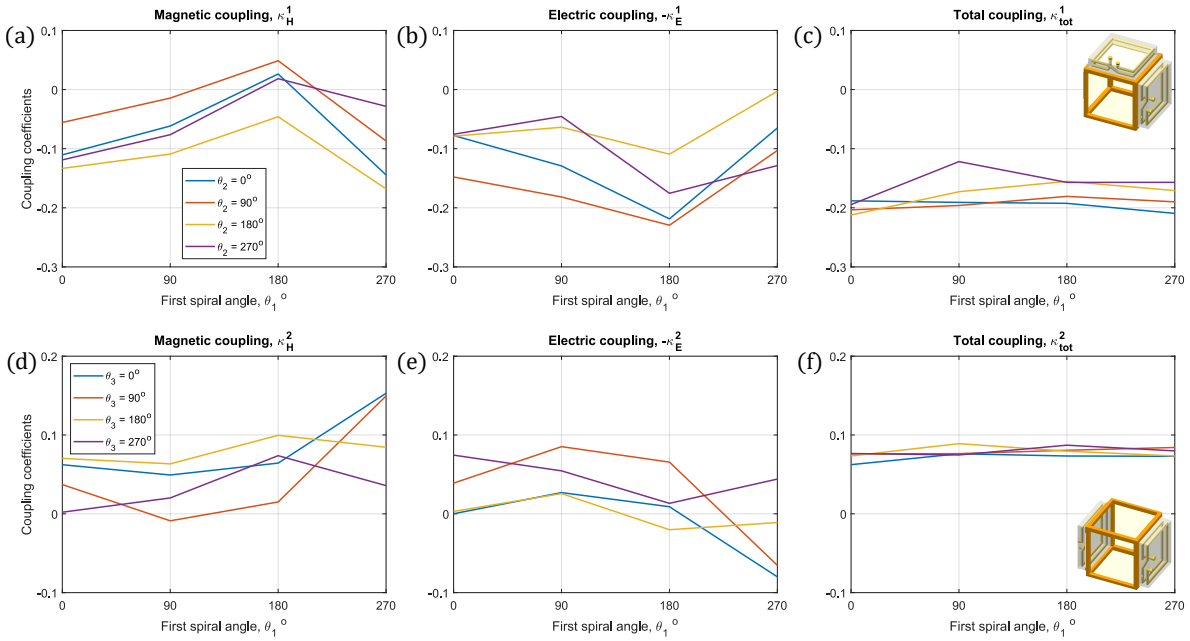


Figure 5.30: Coupling coefficients for the (a)-(c) Orthogonal setup, and (d)-(f) Axial setup as the angle of the second spiral changes.

Again, the coupling coefficients between theory and experiment differ, but qualitatively the model still provides useful information on the coupling mechanisms. The correction factors for the orthogonal case are quite large, almost double in magnitude than the correction factors of the axial setup. At the same time, in the axial setup the disagreement in Fig. 5.31(c) is not as prominent. Thus, the method could fail when the correction factors become large.

Regardless, the extracted coupling coefficients are not trustworthy. Alternatively, the magnitude of the total coupling coefficient can be estimated from the size of the resonance split and the sign can be determined from the phase of the currents I_2/I_1. As shown in Fig. 5. 32, the orthogonal arrangements have a negative coupling coefficient because the lower mode is antisymmetric. Conversely, the axial arrangement shows a positive coupling coefficient. The three total coupling coefficients are $\kappa_1 = -0.12$ (orthogonal), $\kappa_2 = -0.09$ (orthogonal, $\theta_1 = 90^o$, $\theta_2 = 270^o$) and $\kappa_3 = 0.05$ (axial). The Z matrix of any number of spirals in the

cube can now be constructed. The spirals can be placed in such a way so that there are three different coupling coefficients present in the cube, depending on whether two sets of sprue holes are facing each other or not so that κ_2 is present.

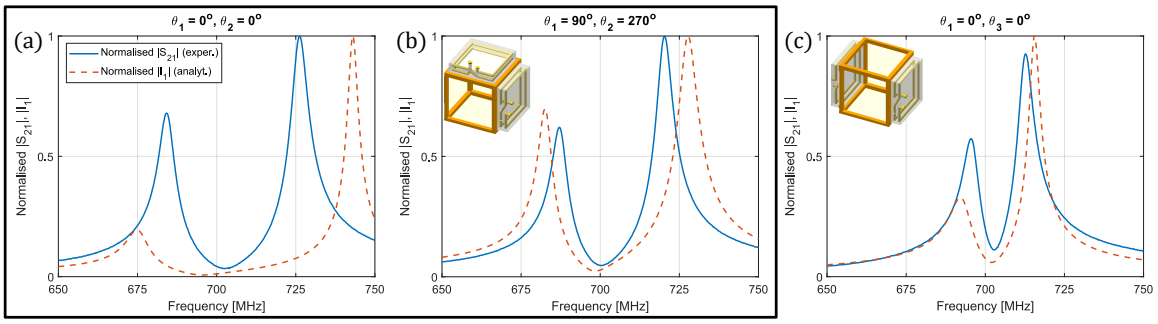


Figure 5.31: Normalised $|S_{21}|$ parameter and current $|I_1|$ of the first spiral in the orthogonal setup at (a) $\theta_1 = 0^o$, $\theta_2 = 0^o$, (b) $\theta_1 = 90^o$, $\theta_2 = 270^o$, and (c) Axial setup at $\theta_1 = 0^o$, $\theta_3 = 0^o$.

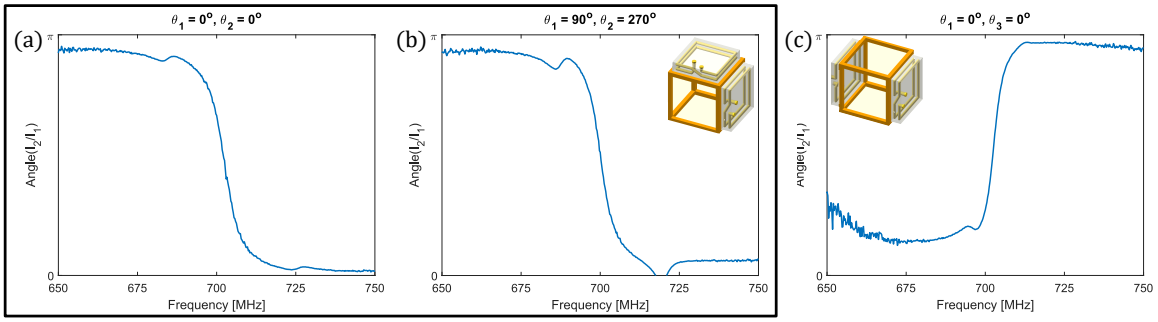


Figure 5.32: Experimental phase of the currents I_2/I_1 in the orthogonal setup at (a) $\theta_1 = 0^o$, $\theta_2 = 0^o$, (b) $\theta_1 = 90^o$, $\theta_2 = 270^o$, and (c) Axial setup at $\theta_1 = 0^o$, $\theta_3 = 0^o$.

In Fig. 5.33 the normalised experimental $|S_{21}|$ parameter (red) and analytic $|I_1|$ current (blue) of the cube fitted with three spirals are shown. The spirals can be fitted in such a way so that there is only the κ_1 coupling present in the cube, as shown in Fig. 5.33(a). In this case two resonances appear on the graph, with a larger split of 65 MHz. The spirals can be placed in the cube so that there is also the κ_2 coupling, see Fig. 5.33(b), resulting in three peaks showing in the graph. There are no experimental data for this case. A different arrangement can allow for the axial coupling κ_3 to be present in the structure, see Fig. 5.33(c), which also leads to three resonances. In all cases, the higher resonance appears in the same frequency of $\sim$750 MHz.

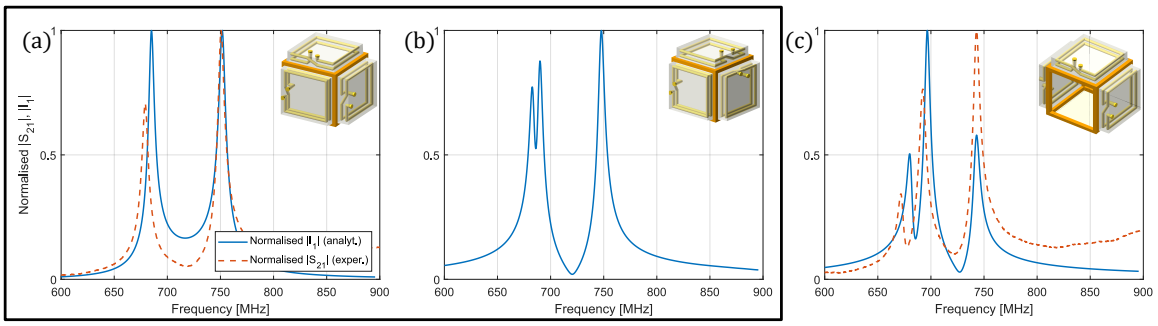


Figure 5.33: Normalised experimental $|S_{21}|$ parameter (red dashes) and analytic $|I_1|$ current (blue line) of the cube fitted with three spirals. (a) Only κ_1, (b) κ_1 and κ_2, and (c) κ_1 and κ_3.

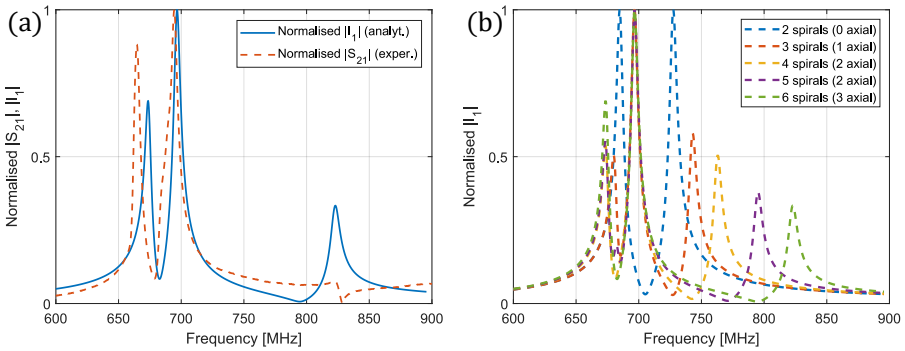


Figure 5.34: Normalised experimental $|S_{21}|$ parameter (red dashes) and analytic $|I_1|$ current (blue line) of the cube fitted with six spirals without the coupling κ_2, and (b) Analytic $|I_1|$ current for arrangements with increasing number of spirals.

A cube fitted with six spirals was measured on Fig. 5.34(a). The spirals were fitted in such a way that there is no coupling κ_2 present in the structure. Both the experiment and analytic data show three resonances. It appears that when there are two couplings, κ_1 and κ_3, up to three resonances can appear due to the degeneracy in the cube. In Fig. 5.34(b) the analytic currents $|I_1|$ for various arrangements of spirals in the cube are shown. The numbers of spirals was increased from two to six, with the number of axial spirals shown in the parenthesis of the legend. All setups show three resonances, except the one with the two spirals. As more spirals are added, the lower resonance is close to 670 MHz, while the central resonance for all cases is close to 700 MHz, which is the resonance of the single resonator. The upper resonance however shifts to higher frequencies as more spirals are added to the cube.

The spiral resonator has only a 360^o rotation symmetry. A cube made of such a unit

cell is expected to show three resonances as shown by Baena et. al in [78]. Here we show that, depending on the orientation of the spirals in the cube, up to three different coupling coefficients can be present in the structure, effectively allowing for the number and position of the resonances to be tuned. A cube will have an isotropic behaviour if resonators of high symmetry are used, such as the bianisotropic SRR. In the future, these resonators could be fabricated using the Field's metal method.

5.6 3D circuits

This chapter will close off with a promising application of the Field's metal method, which is the fabrication of 3D circuits. It has been demonstrated that conductive tracks buried inside a dielectric medium can be reliably fabricated. In the previous sections, the size and resistance of the buried tracks was characterized. Utilising the 3D capabilities of the method, the conductive tracks can curve around each other while remaining electrically isolated, allowing for the miniaturization of the circuit. At the same time, the dielectric substrate does not have to be a planar rectangular, but can be of any shape to better fit the intended application. Both of those are limitations in standard circuits made with PCB.

It was also shown that filled samples can be reheated to melt the metal, thus allowing for "solderless soldering" in which components can simply be placed in the sprue holes. When the device has run its life, it can be reheated so all the components can be removed and reused or recycled. Furthermore, once melted, the metal can also be removed and reused, leaving only the dielectric substrate which can be made from a recyclable or compostable material. This paves the path for recyclable devices with a low environmental impact.

To demonstrate the method's capabilities, a thermometer circuit shown in Fig. 5.35(a) was fabricated as a proof of concept. A thermistor senses the temperature while a PNP array is used to drive each of the two LED digits. The microcontroller is programmed to show the temperature according to the input of the thermistor. The thermometer design with the buried paths for Field's metal filling is shown in Fig. 5.35(b). Each path has a diameter of 0.8 mm, with the sprue holes being conical reaching a diameter of 1.2 mm to avoid clogging of

the vertical paths. Red colour indicates the "+" path while blue shows the ground. There are three layers of buried paths with a separation of 0.2 mm between them: from top to bottom yellow, green and purple. On the insets, it can be seen that the paths are fabricated quite densely and can change layers to curve around each other without touching.

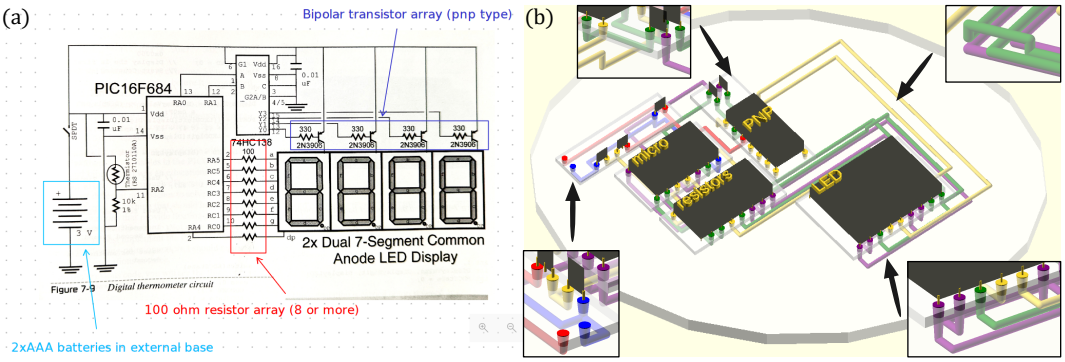


Figure 5.35: (a) Circuit diagram of the thermometer taken from "123 PIC microcontroller projects for the evil genius", and (b) The designed circuit on OpenSCAD.

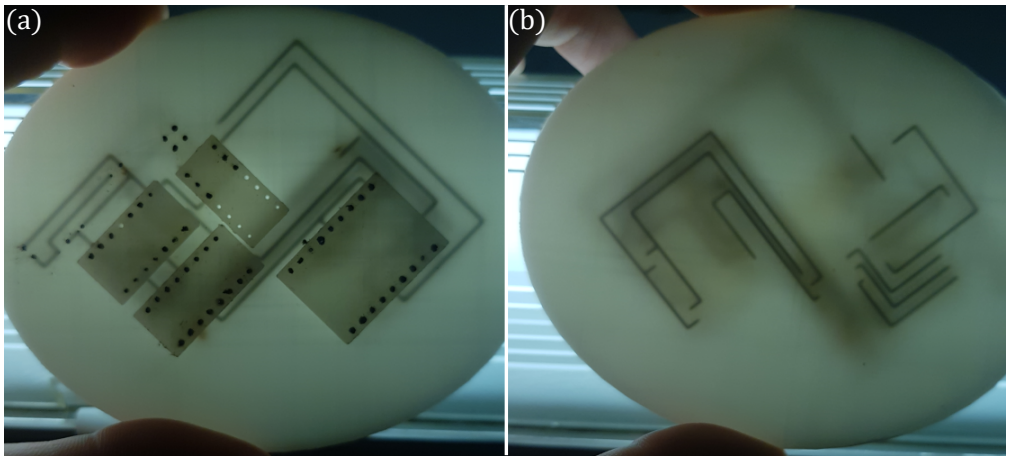


Figure 5.36: Photograph of the thermometer circuit fabricated with HIPS. (a) Top view, and (b) Bottom view.

On Fig. 5.36 the filled HIPS sample is shown as seen from the top and the bottom side. Using a back light, the first and last layers of metal paths inside the HIPS substrate can be seen. In order to see the paths clearly, a thermometer with 4 LED digits was printed with a transparent resin using a photopolymer printer (3D Systems Multijet MJP 2500 Plus) at the 3D printing laboratory of the department, see Fig. 5.37.

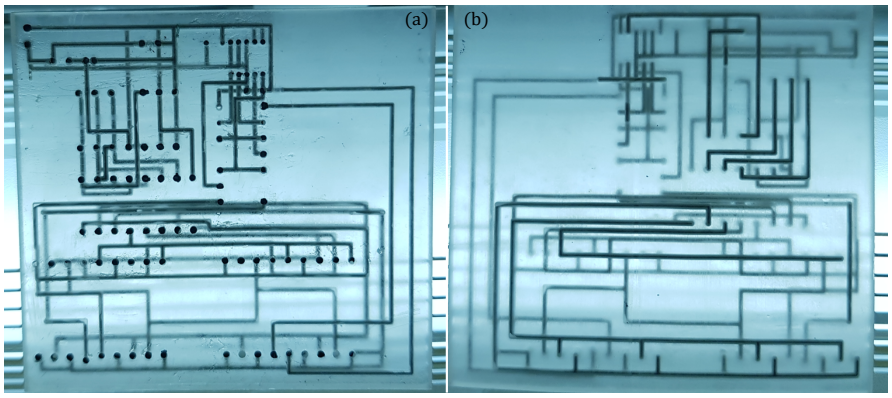


Figure 5.37: Photograph of the thermometer circuit fabricated with transparent material. (a) Top view, and (b) Bottom view.

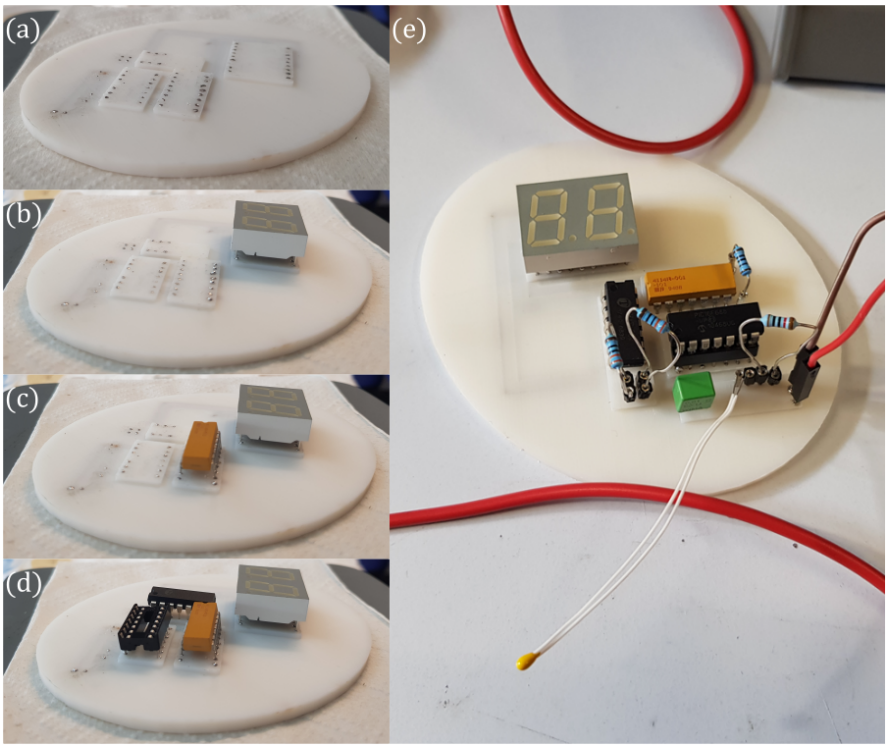


Figure 5.38: The thermometer circuit fabricated with HIPS placed on a hot plate as components are placed in their place. (a) Reheating the HIPS sample, (b) LED is placed, (c) Resistorarray is placed, (d) PNP array and microcontroller socket are placed, and (e) Final device connected with a +3 V power source.

After filling and photo shooting, an ohmmeter was used to test that the electrical tracks of the HIPS sample are connected as they should be. Then, the circuit is reheated on a hot plate so the metal melts and the components can be placed one by one as shown on Fig. 5.38.

The LED display, resistor array, PNP array and microcontroller could be placed quite easily. The smaller components with two pins were more difficult to put in, hence pin sockets were used for them.

The finished thermometer is connected with a +3 V power supply. When turned on, the thermometer measures the room temperature of 23^oC, but when the thermistor is held the temperature of the LED display is increased to 29^oC, showing the functionality of the circuit.

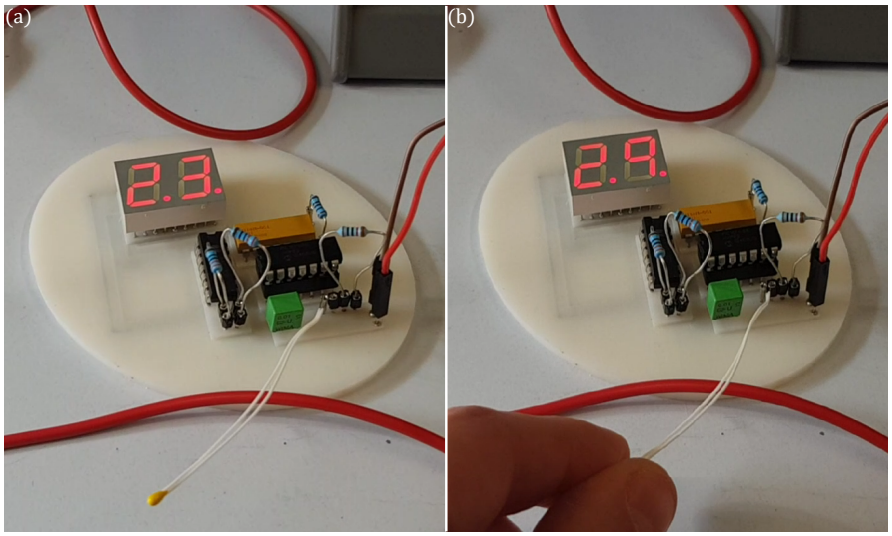


Figure 5.39: HIPS thermometer (a) At room temperature, and (b) When thermistor is held.

This chapter focuses on the development of a novel fabrication method based on liquid metal injection for the realization of 3D conductive structures. Following an investigation of various dielectric materials used in FDM and a range of low-melting alloys, it is concluded that the combination of HIPS and Field's metal has great potential for the fabrication of devices to be used in high frequency electronics. Furthermore, we demonstrate that Field's metal holds great promise to be incorporated into standard FDM apparatus, with the creation of a custom-made filament loaded on a commercially available 3D pen. Although in our setup there are limitations in the fabrication resolution, namely the minimum design diameter of fabricated paths that could be reliably reproduced is 0.8 mm, we believe that such limitations can be overcome by using a nozzle of a smaller diameter. We provide a reliable measurement of the conductivity of Field's metal, which, to the best of our knowledge, was lacking from the literature. The spiral resonators fabricated exhibited high quality factors. It is shown that both their resonance frequency and quality factor can be tuned, either by using a different dielectric material or by varying the number of turns. The XCT scan revealed corrugations in the metal paths of filled spirals, contributing to higher losses and thus limiting their performance. We believe that these corrugations would get minimized if a nozzle of a smaller diameter is used. The coupling between spirals in a planar arrangement was investigated and it was shown that when the spirals are placed in such a way so that their sprue holes are facing each other, the total coupling is reduced. This enables three different coupling coefficients to be present in a 3D cube made of such resonators: one axial coupling coefficient between spirals on opposite sides of the cube and two orthogonal coefficients between spirals on adjacent sides of the cube. The analytic model based on circuit theory and the extraction method used for the coupling coefficients were found to be not as accurate when studying the spiral resonators. One possible explanation is that the electrical size of the spirals is not significantly smaller than the wavelength at resonance and the currents are not homogeneous. Finally, it is demonstrated that a structure with a large number of paths can be realized with the fabrication of a thermometer device.

Chapter 6
Conclusions and future work

The fields of metamaterials and magnetoinductive waves have attracted significant research interest over the last two decades. The split ring resonator, a prime example of a building block for metamaterial structures, has been extensively studied in various discrete arrangements but studies on coalesced resonators have been limited. This thesis contributes to the investigation of the coupling mechanisms and dispersion characteristics of both discrete and coalesced resonators, offering novel ways of controlling the dispersion of magnetoinductive waves over a broad range of frequencies. At the same time, the thesis addresses the challenge of fabricating 3D metamaterials by developing a novel method based on the injection of Field's metal inside 3D printed dielectric moulds. Field's metal fabrication carries substantial technological potential, particularly in the field of additive manufacturing.

Chapter 1 offered an introduction to metamaterials and magnetoinductive waves, highlighting the issues this thesis addressed withing the framework of contemporary research. The importance of circuit theory in the analysis of magnetoinductive waves was discussed, as well as the significance of the coupling mechanisms between resonators. At the same time, the challenge of fabricating 3D conductive structures was explored, with an emphasis on fused deposition modelling. To address this issue, a novel method based on liquid metal injection of Field's metal inside 3D printed moulds was proposed.

Chapter 2 formulated an analytic model based on circuit theory suitable for the analysis of the coupling mechanisms between split ring resonators and of the propagation of magnetoinductive waves. While previously this model has been used only for discrete resonators [63], it was shown that the model is valid for coalesced resonators as well, using only the magnetic and electric couplings.

In **Chapter 3**, an optimised methodology of setting up numerical simulations in CST was developed. Using various excitation and measuring tools, it was shown that an experimental setup for measuring the resonance of a single split ring resonator can be reliably replicated

in CST, using a magnetic field loop antenna as an excitation and a magnetic field probe to record the magnetic field. The effects of various simulation parameters, such as the meshing and boundary conditions, on the resonance, quality factor and simulation time have been thoroughly analysed. It was demonstrated that these parameters can be optimised so that the simulations match the experimental results, without the need to setup more computationally demanding simulations, while enabling an adequate empirical fit for such experimental parameters.

Future research as an extension of this work include

- optimising the fitting process when more than one split ring resonator is simulated. The fitting process results in an excellent agreement when investigating a single split ring resonator. However, when more split ring resonators are added a frequency mismatch appears, where the simulated data slightly shift to higher frequencies compared to the experimental results. Our hypothesis is that, by adding more split ring resonators the simulated geometry is altered, which changes the meshing and, subsequently, the resonance frequency. It would be interesting to investigate this and potentially lay down a set of conditions to eliminate the observed frequency mismatch.

- a methodical fitting of the simulation parameters across different frequency regimes. From the structures studied, it appears that for the same split ring resonator geometry the fitted mesh needs to be finer as the frequency increases, but more samples are needed to draw reliable conclusions. An empirical relation showing how the fitting parameters change with frequency would allow the user to set up a reliable simulation faster.

- verifying whether the fitting process can be reliably applied to 2D and 3D structures. Once fitted, the simulation can be used to study the behaviour of planar arrays of split ring resonators, paving the way for numerical support during rapid prototyping studies.

In **Chapter 4** the coupling mechanisms and dispersion characteristics of discrete and coalesced split ring resonators with different number of gaps were investigated, with the goal of developing novel ways of dispersion control. Although arrangements of discrete split ring

resonators have been extensively studied in the past, configurations of coalesced split ring resonators have been largely ignored by the literature. The chapter aims to close this gap, by performing the first, to the best of our knowledge, thorough comparative study of both discrete and coalesced structures. The complex coupling coefficients were extracted separately using the analytic method of Chapter 2. By performing a detailed parametric study on split ring resonators in discrete and coalesced arrangements, while varying the number of gaps and the capacitance values, it was demonstrated that, for coalesced resonators with their shared side capacitively loaded, the electric coupling increased dramatically in magnitude, resulting in the total coupling coefficient to switch to positive values. It was shown that the imaginary parts of the coupling coefficients were significantly smaller than the real parts, thus confirming that retardation in all structures is negligible. While the values of the electric and magnetic coupling coefficients retrieved from experimental and numerical data differ slightly, the agreement for the total coupling coefficient is remarkably good. By running simulations on coalesced circular resonators it was confirmed that the mutual capacitance K is approximately equal to the capacitance of the shared side. It was demonstrated that a more practical approach to coupling and dispersion control can be achieved by tuning the capacitance of the shared sides. In particular, the total coupling coefficient switching to positive values has been confirmed for resonator arrays, which showed a switch from a backward to a forward magnetoinductive wave propagation. In all cases, the experimental, numerical and analytic data were shown to be in excellent agreement with each other. By moving to higher frequencies it was shown that the switching behaviour indeed occurred over a broad range of frequencies. Even though our investigations were expanded to the GHz regime, retardation effects remained weak enough, due to the electrical size of the split ring resonators being approximately one quarter of the wavelength at resonance, thus justifying the use of the analytical model for at least a qualitative prediction of the structure parameters required for the controlled switch between backward and forward wave regimes.

In the future, this work can be expanded upon to

- study coalesced split ring resonators of different unit cells and orientations. In the square

resonators studied here it was shown that when coalesced, the most important factor determining the type of magnetoinductive wave that can propagate on the structure is whether the shared side has a gap or not. Using different shapes would allow the resonators to be coalesced in more directions. Furthermore, a diatomic chain of resonators, where the unit cell consists of two split ring resonators, could feature both discrete and coalesced elements, thus having both negative and positive total couplings present at the same time. It would also be interesting to investigate the coupling of coalesced resonators rotated relative to each other. Would the mutual capacitance K be roughly equal to the capacitance of the shared side at different angles?

- investigate 2D and 3D structures. In two and three dimensions the potential for coalescing along one or more axes offers a new degree of flexibility to the designer. For example a structure where coupling was positive in the x-axis and negative in the y-axis could be designed. Such a mesh would support forward waves in the x direction and backward waves in the y direction whilst still being essentially planar.

- create a functional variable capacitor array. In practice, the capacitance on the shared side could be controlled with liquid crystals which are capable of changing the capacitance in response to voltage or temperature. This poses the challenge of creating a design to incorporate low-loss liquid crystals within the structure. Such devices could be used in applications where wave control is important. At the same time, they could be used as environment sensors, by retrieving the temperature from the bandpass type and size, or switches, where wave propagation is switched off when the temperature reaches a certain value. It would be interesting to investigate capacitance variations in specific gaps of the resonators, to create similar or different effects of dispersion control.

In **Chapter 5** the Field's metal fabrication method was characterized and used to fabricate spiral resonators, with the goal of addressing the challenges of fabricating 3D conductive structures. Field's metal low melting point of 65^{o}C was shown to be thermally compatible with many filament used in fused deposition modelling. It was shown that creating buried microchannels which are subsequently filled with liquid Field's metal, is a viable method of

creating conductive structures inside a dielectric medium. The filling process was performed with a custom-made Field's metal filament loaded on a commercially available 3D pen. This showed great potential for Field's metal fabrication to be incorporated into standard fused deposition modelling apparatus. It was shown that the printed path diameter is slightly smaller than the designed path diameter. In our setup using high impact polystyrene, the paths were printed with a circular cross-section, with the smallest designed path diameter that could be reliably reproduced being 0.8 mm. Vertical paths were shown to be more susceptible to clogging, as their printed diameter got smaller as the height of the path increased. This was also confirmed by the resistance measurements, where vertical turns did not result in a decrease to the measured path resistance, as was the case for horizontal paths. This diameter decrease was compensated by making vertical paths conical. It was demonstrated that the sprue holes could be printed as close as 1.27 mm without touching, while the paths themselves could be as close as 0.1 mm while remaining electrically isolated. Even though the quality factor of the Field's metal coalesced split ring resonators was found to be lower than the printed circuit board counterparts, the arrays showed the expected forward magnetoinductive wave propagation. Utilizing the 3D fabrication capabilities of the method, spiral resonators with high quality factors were fabricated. It was shown that their resonance can be tuned by using dielectric materials with suitable ε_r and $\tan\delta$, or by adjusting the number of turns in the spiral. The X-ray computer tomography scan showed that the metal has conformed to the shape of the paths, although it carried conjugations which increased the losses and reduced the performance. A 3D metamaterial cube constructed using the spiral resonators was subsequently used to investigate the different types of coupling present in the structure. Finally, it was demonstrated that the method can be used to realize 3D circuits with the fabrication of a thermometer device.

In the future our findings could be further developed by

- automating the fabrication process, aiming to incorporate the Field's metal filling to standard fused deposition modelling apparatus. Even though the dielectric substrate is fabricated automatically, the filling of the microchannels is performed manually. How-

ever, the creation of a Field's metal filament which can be loaded on a commercially available 3D pen is demonstrated. When heated, the Field's metal filament turns liquid and not viscous, unlike most fused deposition modelling filaments. The task of creating a fused deposition modelling machine that can use the Field's metal filament would require a fair bit of programming and flow rate characterization.

- expanding the range of available dielectrics and conducting a thorough characterization for each one. The dielectric material of the substrate is crucial for Field's metal devices. Not only it affects the performance of fabricated devices, but it also determines the quality and diameter of the printed microchannels because some materials are harder to print than others. Due to the rapid growth of fused deposition modelling technologies, new filaments with advanced properties are constantly developed, which will improve the method's capabilities in general.

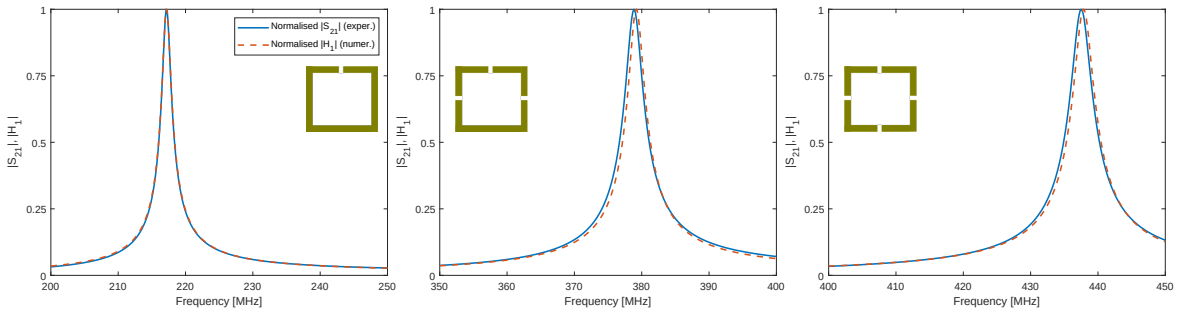
- investigating the use of Field's metal in 3D environmentally friendly devices. The thermometer circuit showcased that 3D devices can be fabricated with Field's metal. Furthermore, once the device has run its life, it can be reheated to melt the metal which can be removed and recycled, while the dielectric can be made from a recyclable or compostable material. This paves the path for completely recyclable devices to be used in the future.

.

Appendix A
Higher frequency results

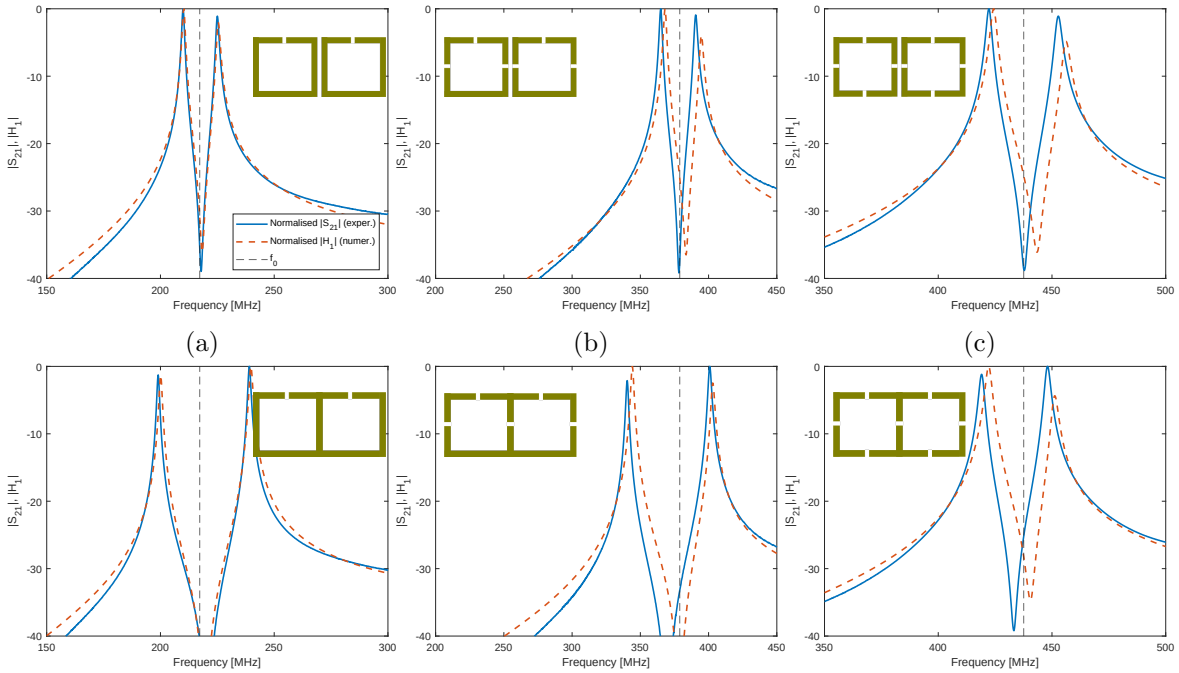
Appendix A shows the detailed results on unit cells, dimers and arrays with 10 pF and 1 pF samples soldered into the gaps. The analytic model, numerical data and experimental measurements are compared. These results support the main findings of Chapter 4, where a more concise version of the results that better fit the story of Chapter 4 was presented.

1 10 pF samples



(a) (b) (c)

Figure A.1: Normalised experimental $|S_{21}|$ (solid blue line) and numerical $|H_1|$ (dashed red line) measurements for the (a) One-gap, (b) Three-gap, and (c) Four-gap unit cells.



(a) (b) (c)

(d) (e) (f)

Figure A.2: Normalised experimental $|S_{21}|$ (solid blue line) and numerical $|H_1|$ (dashed red line) measurements for dimer samples. (a)-(c) Discrete, and (d)-(f) Coalesced dimers. The grey dashed line shows the resonance of the unit cell.

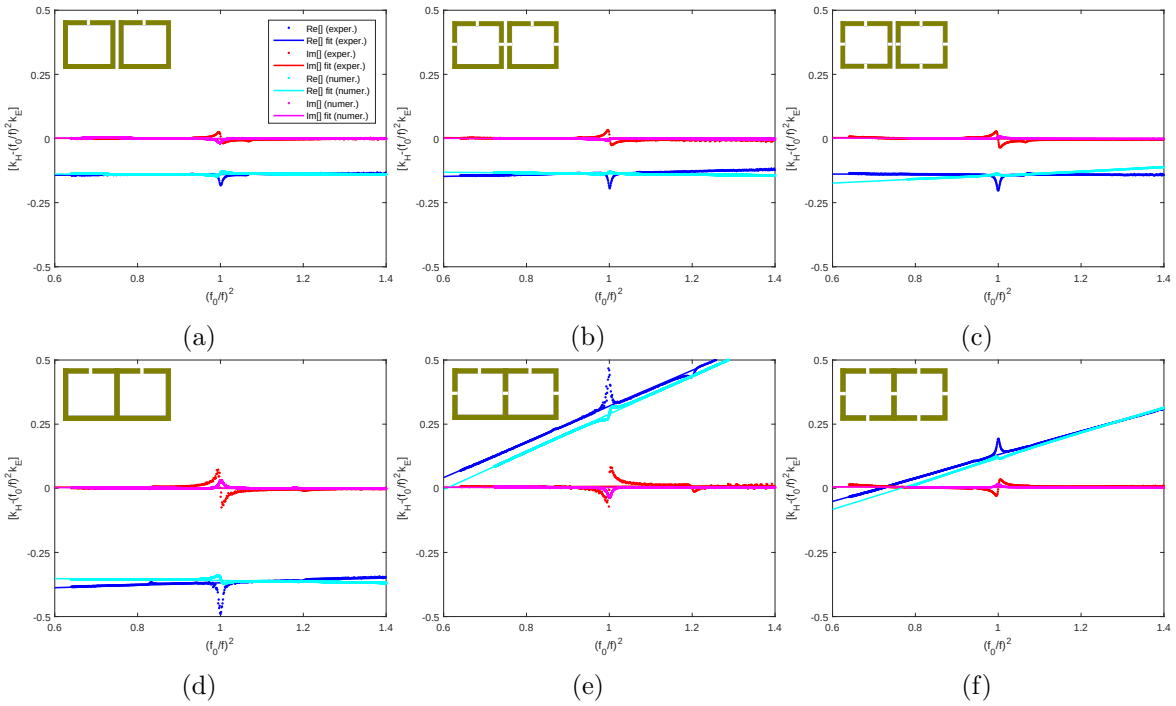


Figure A.3: Real (blue and cyan) and imaginary (red and pink) parts of EQUATION for experimental and numerical data for (a)-(c) Discrete, and (d)-(f) Coalesced dimers. The linear fit is also shown.

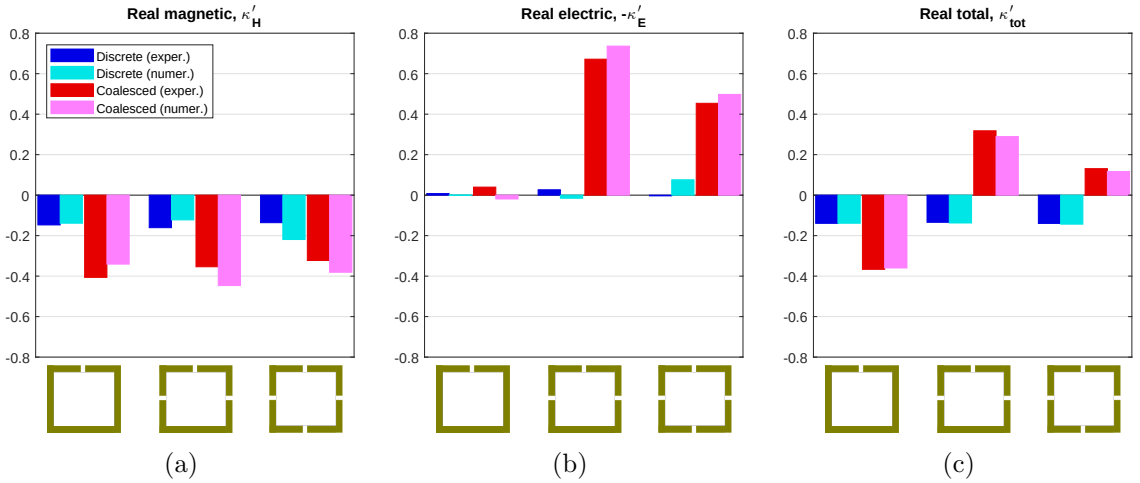


Figure A.4: Real parts of the (a) Magnetic, (b) Electric, and (c) Total coupling coefficients for the discrete and coalesced dimers. The values of discrete resonators are shown with blue (experimental) and cyan (numerical), while the values of coalesced resonators are shown with red (experimental) and pink (numerical).

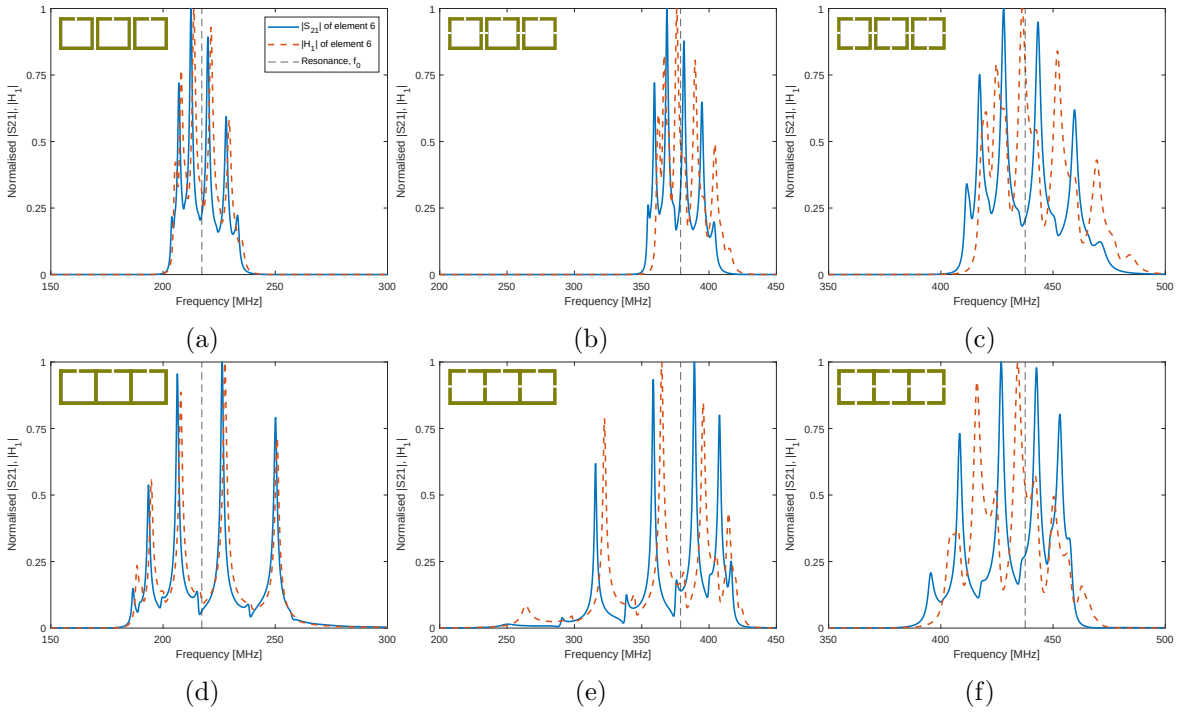


Figure A.5: Normalised experimental S_{21} (solid blue line) and numerical $|H|$ (dashed red line) measurements of the 6^{th} element in the 11 element array. (a)-(c) Discrete, and (d)-(f) Coalesced.

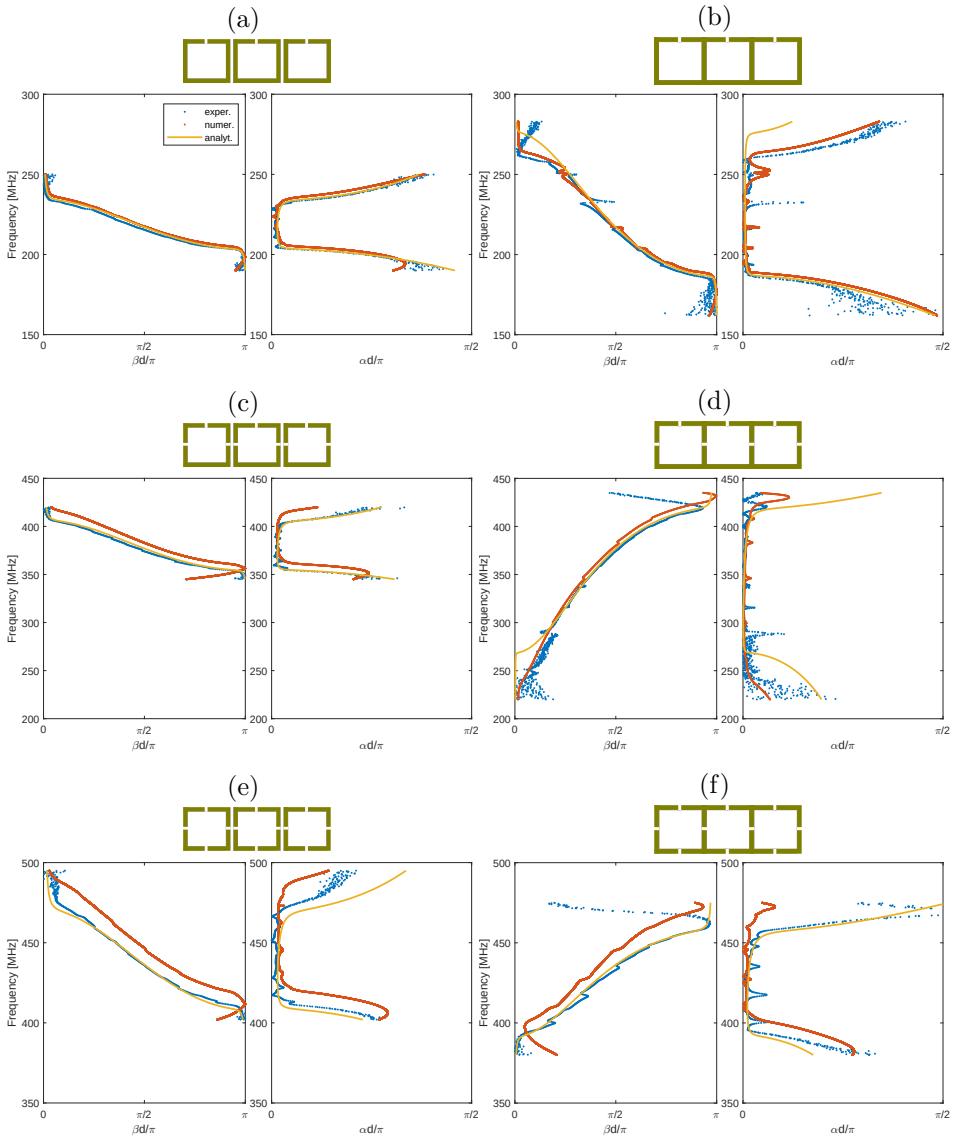
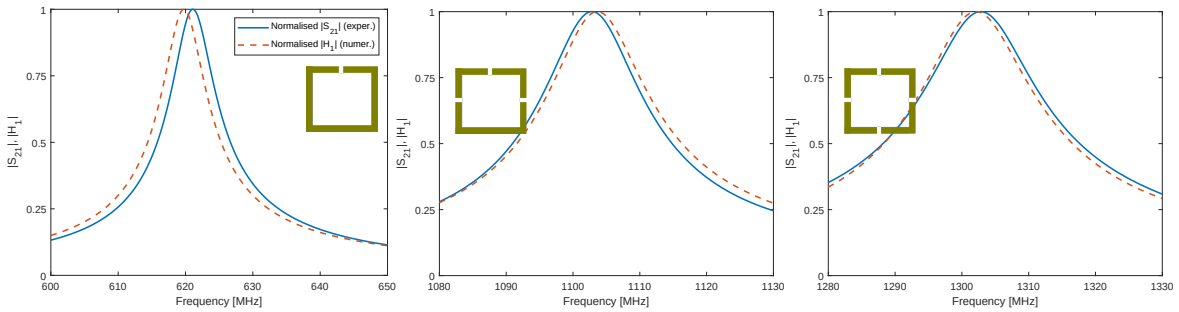


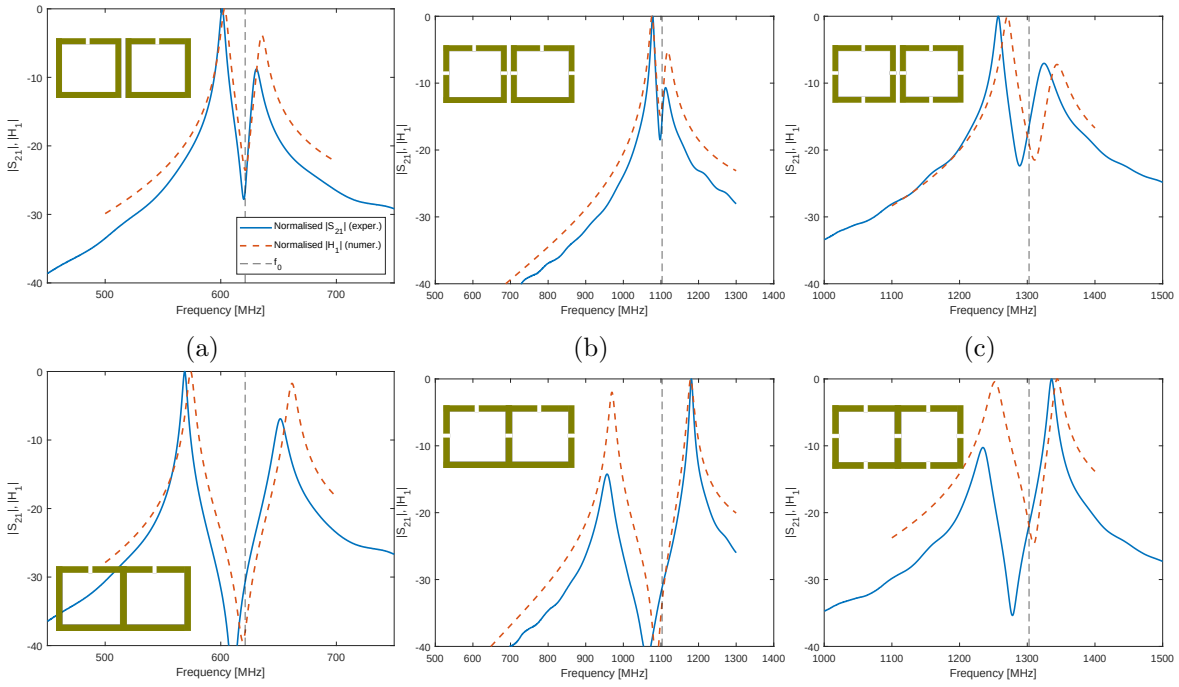
Figure A.6: Dispersion and attenuation for the (a), (b) One-gap, (c),(d) Three-gap, and (e), (f) Four-gap arrays. The experimental (blue dots) and simulation (red dots) data were calculated from the currents of three consecutive elements. The analytic model (yellow line) includes losses and retardation.

2 1 pF samples



(a) (b) (c)

Figure A.7: Normalised experimental $|S_{21}|$ (solid blue line) and numerical $|H_1|$ (dashed red line) measurements for the (a) One-gap, (b) Three-gap, and (c) Four-gap unit cells.



(a) (b) (c)

(d) (e) (f)

Figure A.8: Normalised experimental $|S_{21}|$ (solid blue line) and numerical $|H_1|$ dashed red line) measurements for dimer samples. (a)-(c) Discrete, and (d)-(f) Coalesced dimers. The grey dashed line shows the resonance of the unit cell.

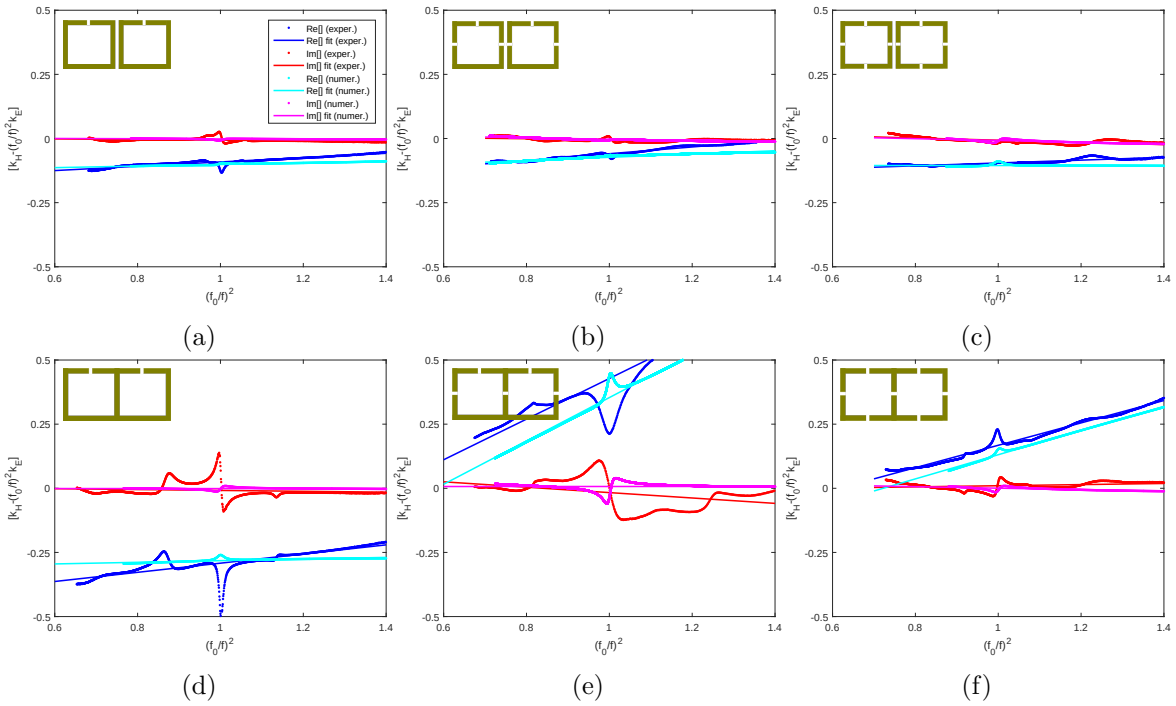


Figure A.9: Real (blue and cyan) and imaginary (red and pink) parts of EQUATION for experimental and numerical data for (a)-(c) Discrete, and (d)-(f) Coalesced dimers. The linear fit is also shown.

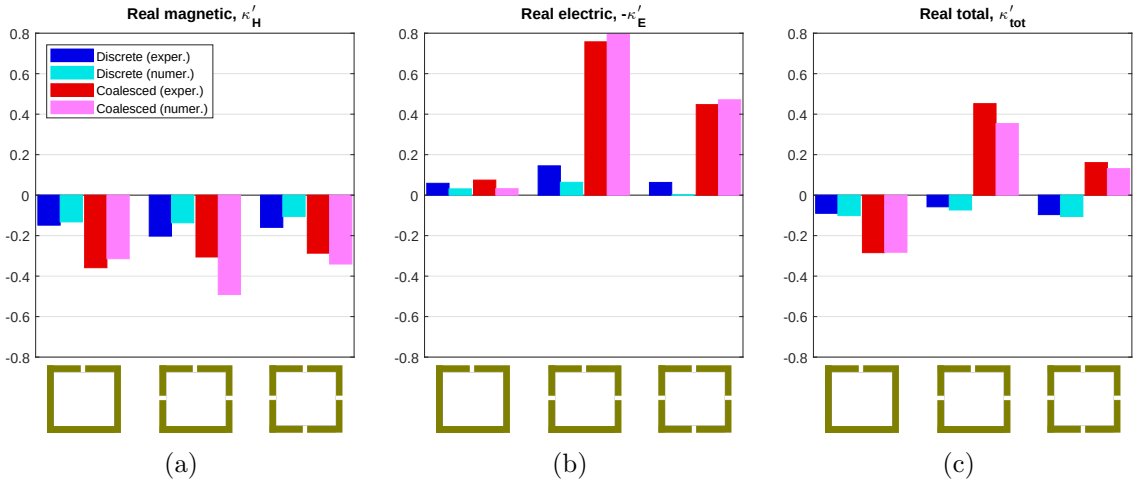


Figure A.10: Real parts of the (a) Magnetic, (b) Electric, and (c) Total coupling coefficients for the discrete and coalesced dimers. The values of discrete resonators are shown with blue (experimental) and cyan (numerical), while the values of coalesced resonators are shown with red (experimental) and pink (numerical).

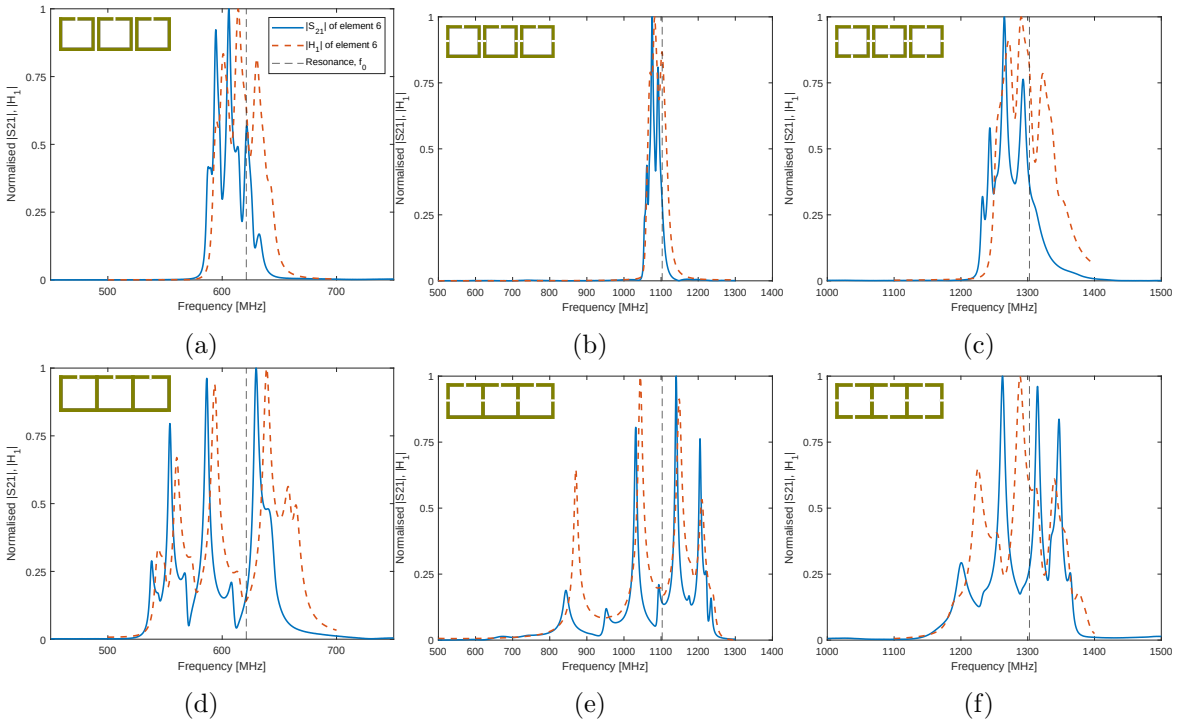


Figure A.11: Normalised experimental S_{21} (solid blue line) and numerical $|H|$ (dashed red line) measurements of the 6^{th} element in the 11 element array. (a)-(c) Discrete, and (d)-(f) Coalesced.

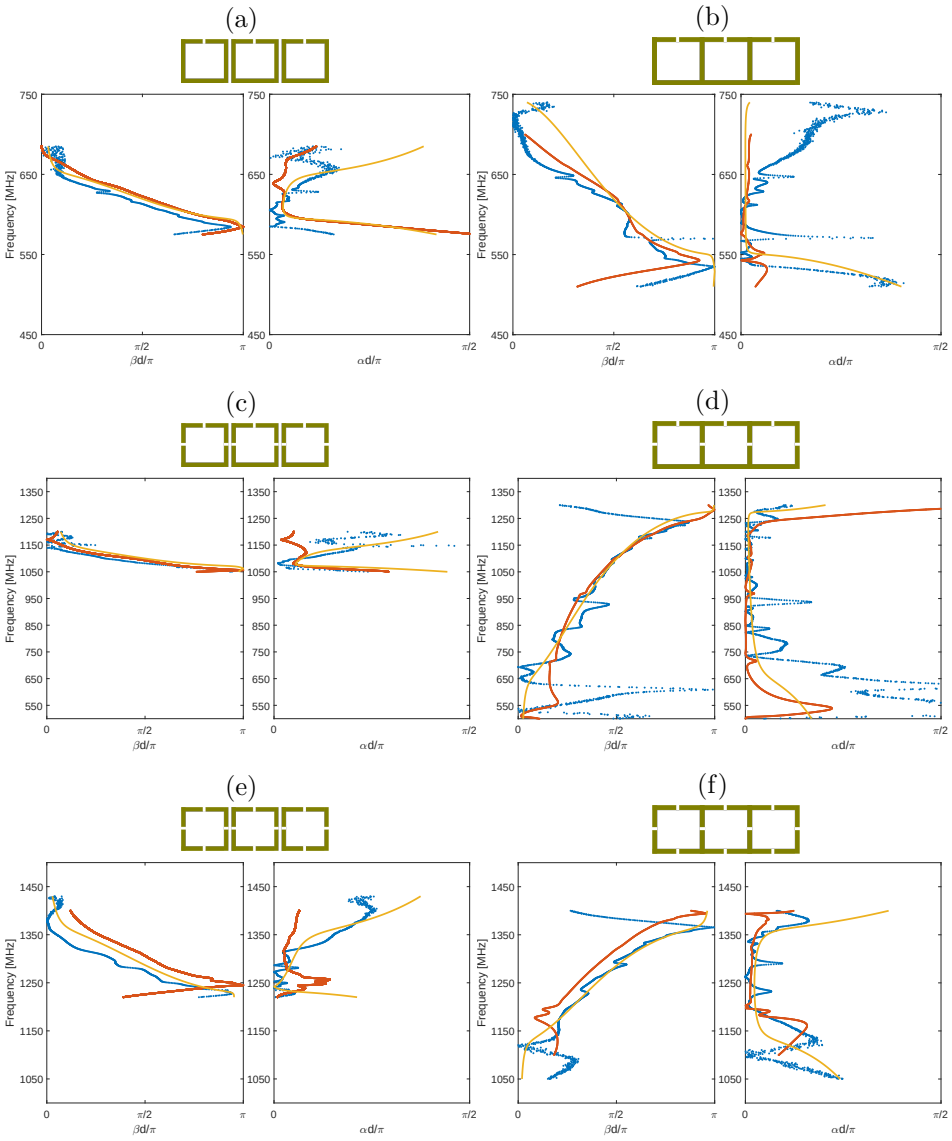


Figure A.12: Dispersion and attenuation for the (a), (b) One-gap, (c),(d) Three-gap, and (e), (f) Four-gap arrays. The experimental (blue dots) and simulation (red dots) data were calculated from the currents of three consecutive elements. The analytic model (yellow line) includes losses and retardation.

References

[1] M. Kadic, G. W. Milton, M. Hecke, et al. "3D metamaterials". *Nat. Rev. Phys.* 1, 198 (2019).

[2] S. Xiao, T. Wang, T. Liu, et al. "Active metamaterials and metadevices: a review". *J. Phys. D: Appl. Phys.* 53, 503002 (2020).

[3] Z. Wang, C. Luan, G. Liao, et al. "Progress in auxetic mechanical metamaterials: structures, characteristics, manufacturing methods, and applications". *Adv. Eng. Mater.* 22, 2000312 (2020).

[4] H. M. A. Kolken and A. A. Zadpoor. "Auxetic mechanical metamaterials". *RSC Adv.* 7, 5111 (2017).

[5] T. Bückmann, M. Thiel, R. Schittny, et al. "An elasto-mechanical unfeelability cloak made of pentamode metamaterials". *Nat. Commun.* 5, 4130 (2014).

[6] Y. Chen, X. Liu, and G. Hu. "Latticed pentamode acoustic cloak". *Sci. Rep.* 5, 15745 (2015).

[7] R. Gatt and J. N. Grima. "Negative compressibility". *Phys. Stat. sol. - Rapid. Res. Lett.* 2, 236 (2008).

[8] Z. G. Nicolaou and A. E. Motter. "Mechanical metamaterials with negative compressibility transitions". *Nat. Mater.* 11, 608 (2012).

[9] L. Wu, B. Li, and J. Zhou. "Isotropic negative thermal expansion metamaterials". *ACS Appl. Mater. Interfaces* 8, 17721 (2016).

[10] Q. Wang, J. A. Jackson, Q. Ge, et al. "Lightweight mechanical metamaterials with tunable negative thermal expansion". *Phys. Rev. Lett.* 117, 175901 (2016).

[11] O. Sakai. "Transition between positive and negative permittivity in field-dependent metamaterial". *J. Appl. Phys.* 109, 084914 (2011).

[12] A. Sarkhel, D. Mitra, S. Paul, et al. "A compact meta-atom for dual band negative permittivity metamaterial". *Microw. Opt. Technol. Lett.* 57, 1152 (2015).

[13] A. R. Diaz and O. Sigmund. "A topology optimization method for design of negative permeability metamaterials". *Struct. Multidiscipl. Optim.* 41, 163 (2010).

[14] S. Hrabar, J. Bartolic, and Z. Sipus. "Waveguide miniaturization using uniaxial negative permeability metamaterial". *IEEE Trans. Antennas Propag.* 53, 110 (2010).

[15] D. R. Smith, W. J. Padilla, D. C. Vier, et al. "Composite medium with simultaneously negative permeability and permittivity". *Phys. Rev. Lett.* 84, 4184 (2000).

[16] W. J. Padilla, D. N. Basov, and D. R. Smith. "Negative refractive index metamaterials". *Mater. Today* 9, 28 (2006).

[17] N. I. Landy, S. Sajuyigbe, J. J. Mock, et al. "Perfect metamaterial absorber". *Phys. Rev. Lett.* 100, 207402 (2008).

[18] G. Duan, J. Schalch, X. Zhao, et al. "Identifying the perfect absorption of metamaterial absorbers". *Phys. Rev. B* 97, 035128 (2018).

[19] W. Cai, U. K. Chettiar, A. V. Kildishev, et al. "Optical cloaking with metamaterials". *Nat. Photonics* 1, 224 (2007).

[20] I. I. Smolyaninov, V. N. Smolyaninova, and A. V. Kildishev. "Anisotropic metamaterials emulated by tapered waveguides: application to optical cloaking". *Phys. Rev. Lett.* 102, 213901 (2009).

[21] H. Lamb. "On group-velocity". *Proc. London Math. Soc.* 1, 473 (1904).

[22] L. I. Mandelstam. "Group velocity in a crystal lattice". *Zh. Eksp. Teor. Fiz.* 15, 475 (1945).

[23] V. E. Pafomov. "Transition radiation and Cerenkenov radiation". *Zh. Eksp. Teor. Fiz.* 36 (1959).

[24] V. M. Agranovich and V. L. Ginzburg. "Spatial dispersion in crystal optics and the theory of excitons". *Interscience Publishers,* London, (1966).

[25] V. G. Veselago. "The electrodynamics of substances with simultanesously negative values of ε and μ". *Sov. Phys. Usp.* 10, 509 (1968).

[26] J. B. Pendry, A. J. Holden, W. J. Stewart, et al. "Extremely low frequency plasmons in metallic mesostructures". *Phys. Rev. Lett.* 76, 4773 (1996).

[27] J. B. Pendry, A. J. Holden, D. J. Robbins, et al. "Low frequency plasmons in thin-wire structures". *J. Condens. Matter Phys.* 10, 4785 (1998).

[28] F. G. Brockman, P. H. Dowling, and W. G. Steneck. "Dimensional effects resulting from a high dielectric constant found in a ferromagnetic ferrite". *Phys. Rev.* 77, 85 (1950).

[29] J. B. Pendry, A. J. Holden, D. J. Robbins, et al. "Magnetism from conductors and enhanced nonlinear phenomena". *IEEE Trans. Microw. Theory Tech.* 47, 2075 (1999).

[30] E. Shamonina, V. A. Kalinin, K. H. Ringhofer, et al. "Magnetoinductive waves in one, two, and three dimensions". *J. Appl. Phys.* 92, 6252 (2002).

[31] M. C. K. Wiltshire, E. Shamonina, I. R. Young, et al. "Dispersion characteristics of magneto-inductive waves: comparison between theory and experiment". *Electron. Lett.* 39, 215 (2003).

[32] O. Sydoruk, M. Shamonin, A. Radkovskaya, et al. "Mechanism of subwavelength imaging with bilayered magnetic metamaterials: theory and experiment". *J. Appl. Phys.* 101, 073903 (2007).

[33] E. Shamonina, V. A. Kalinin, K. H. Ringhofer, et al. "Imaging, compression and poynting vector streamlines for negative permittivity materials". *Electron. Lett.* 37, 1243 (2001).

[34] J. Yan, C. J. Stevens, and E. Shamonina. "A metamaterial position sensor based on magnetoinductive waves". *IEEE Open J. Antennas and Propag.* 2, 259 (2021).

[35] D. Dhayaa, A. Radkovskaya, J. Yan, et al. "Metamaterials for sensing conductive objects using time-domain reflectometry of magnetoinductive waves". *16th International Congress on Artificial Materials for Novel Wave Phenomena (Metamaterials)* 125 (2022).

[36] G. Dima, A. Radkovskaya, C. J. Stevens, et al. "Full-range contactless conductivity detection". *16th International Congress on Artificial Materials for Novel Wave Phenomena (Metamaterials)* X128 (2022).

[37] J. Feis, L. Solymar, and E. Shamonina. "Wireless links via coupled topological edge states". *16th International Congress on Artificial Materials for Novel Wave Phenomena (Metamaterials)* 142 (2022).

[38] J. Feis, C. J. Stevens, and E. Shamonina. "Wireless power transfer through asymmetric topological edge states in diatomic chains of coupled meta-atoms". *Appl. Phys. Lett.* 117, 134106 (2020).

[39] R. R. A. Syms, E. Shamonina, and L. Solymar. "Magneto-inductive waveguide devices". *IEE Proc. Microw. Antennas Propag.* 153, 111 (2006).

[40] A. Radkovskaya, O. Sydoruk, M. Shamonin, et al. "Experimental study of a bi-periodic magnetoinductive waveguide: comparison with theory". *IET Microw. Antenna Propag.* 1, 80 (2007).

[41] M. Beruete, F. Falcone, M. J. Freire, et al. "Electroinductive waves in chains of complementary metamaterial elements". *Appl. Phys. Lett.* 88, 083503 (2006).

[42] A. Hohenau, J. R. Krenn, G. Schider, et al. "Optical near-field of multipolar plasmons of rod-shaped gold nanoparticles". *Europhys. Lett.* 69, 538 (2005).

[43] J. D. Baena, J. Bonache, F. Martin, et al. "Equivalent-circuit models for split-ring resonators and complementary split-ring resonators coupled to planar transmission lines". *IEEE T. Microw. Theory* 53, 1451 (2005).

[44] O. Sydoruk, E. Tatartschuk, E. Shamonina, et al. "Analytical formulation for the resonant frequency of split rings". *J. Appl. Phys.* 105, 014903 (2009).

[45] K. Aydin, I. Bulu, K. Guven, et al. "Investigation of magnetic resonances for different split-ring resonator parameters and designs". *New J. Phys.* 7, 168 (2005).

[46] N. Katsarakis, G. Konstantinidis, A. Kostopoulos, et al. "Magnetic response of split-ring resonators in the far-infrared frequency regime". *Opt. Lett.* 30, 1348 (2005).

[47] J. Zhou, T. Koschny, M. Kafesaki, et al. "Saturation of the magnetic response of split-ring resonators at optical frequencies". *Phys. Rev. Lett.* 95, 223902 (2005).

[48] R. Marqués, F. Medina, and R. Rafii-El-Idrissi. "Role of bianisotropy in negative, permeability and left-handed metamaterials". *Phys. Rev. B* 65, 144440 (2002).

[49] F. Mariotte, S. A. Tretyakov, and B. Sauviac. "Isotropic chiral composite modeling: comparison between analytical, numerical, and experimental results". *Microw. Opt. Technol. Lett.* 7, 861 (1994).

[50] R. R. A. Syms, E. Shamonina, V. Kalinin, et al. "A theory of metamaterials based on periodically loaded transmission lines: Interaction between magnetoinductive and electromagnetic waves". *J. Appl. Phys.* 97, 064909 (2005).

[51] E. Shamonina. "Magnetoinductive polaritons: hybrid modes of metamaterials with interelement coupling". *Phys. Rev. B* 85, 155146 (2012).

[52] F. Hesmer, E. Tatartschuk, O. Zhuromskyy, et al. "Coupling mechanisms for split ring resonators: theory and experiment". *Phys. Status Solidi B* 244, 1170 (2007).

[53] A. Vallecchi, S. Chu, L. Solymar, et al. "Coupling between coils in the presence of conducting medium". *IET Microw. Antennas Propag.* 13, 55 (2019).

[54] A. Chen, A. Kodigala, T. Lepetit, et al. "Multipoles of even/odd split-ring resonators". *Photonics* 2, 883 (2015).

[55] E. Tatartschuk, N. Gneiding, F. Hesmer, et al. "Mapping inter-element coupling in metamaterials: scaling down to infrared". *J. Appl. Phys.* 111, 094904 (2012).

[56] J. Yan, A. Radkovskaya, L. Solymar, et al. "Switchable unidirectional waves on mono- and diatomic metamaterials". *Sci. Rep.* 12, 16845 (2022).

[57] A. Radkovskaya, M. Shamonin, C. J. Stevens, et al. "An experimental study of the properties of magnetoinductive waves in the presence of retardation". *J. Magn. Mater.* 300, 29 (2006).

[58] A. Radkovskaya, M. Shamonin, C. J. Stevens, et al. "Resonant frequencies of a combination of split rings: experimental, analytical and numerical study". *Microw. Opt. Technol. Lett.* 46, 473 (2005).

[59] C. V. Dodd and W. E. Deeds. "Analytical solutions to eddy-current probe-coil problems". *J. Appl. Phys.* 39, 2829 (1968).

[60] P. Petrov, A. P. Hibbins, and J. R. Sambles. "Near-field electromagnetic coupling between helices". *J. Phys. D Appl. Phys.* 54, 445108 (2021).

[61] V. Lomanets, O. Zhuromskyy, G. Onishchukov, et al. "Electrical circuit model of arrays of resonant elements". *Phys. Rev. B* 85, 125110 (2012).

[62] N. Gneiding, O. Zhuromskyy, E. Shamonina, et al. "Circuit model optimization of a nano split ring resonator dimer antenna operating in infrared spectral range". *J. Appl. Phys.* 116, 164311 (2014).

[63] N. Feth, M. Konig, M. Husnik, et al. "Electromagnetic interaction of split-ring resonators: the role of separation and relative orientation". *Opt. Express* 18, 6545 (2010).

[64] I. Al-Naib, E. Hebestreit, C. Rockstuhl, et al. "Conductive coupling of split ring resonators: a path to THz metamaterials with ultrasharp resonances". *Phys. Rev. Lett.* 112, 183903 (2014).

[65] T. Zheng, Z. Xiao, M. Chen, et al. "Ultra-broadband electromagnetically induced transparency in metamaterial based on conductive coupling". *Plasmonics* 17, 717 (2022).

[66] N. Liu, S. Kaiser, and H. Giessen. "Magnetoinductive and electroinductive coupling in plasmonic metamaterial molecules". *Adv. Mater.* 20, 4521 (2008).

[67] C. J. Stevens, Y. Li, and C. W. T. Chan. "Forward magneto-inductive wave propagation in planar magnetically coupled capacitor grids". *J. Electromagnet. Wave.* 29, 753 (2015).

[68] Y. Li, C. W. T. Chan, and C. J. Stevens. "Capacitor-connected grids as one-dimensional UWB data transfer channels". *7th International Congress on Advanced Electromagnetic Materials in Microwaves and Optics* 19 (2013).

[69] Y. Li and C. J. Stevens. "Terminal optimization for wireless power transfer with capacitor-connected grids metamaterial waveguides". *9th International Congress on Advanced Electromagnetic Materials in Microwaves and Optics* 337 (2015).

[70] A. Radkovskaya, O. Sydoruk, E. Tatartschuk, et al. "Dimer and polymer metamaterials with alternating electric and magnetic coupling". *Phys. Rev. B* 84, 125121 (2011).

[71] O. Sydoruk, A. Radkovskaya, O. Zhuromskyy, et al. "Tailoring the near-field guiding properties of magnetic metamaterials with two resonant elements per unit cell". *Phys. Rev. B* 73, 224406 (2006).

[72] S. S. Bukhari, J. Vardaxoglou, and W. Whittow. "A metasurfaces review: definitions and applications". *Appl. Sci.* 9, 2727 (2019).

[73] T. W. Ebbesen, H. J. Lezec, H. F. Ghaemi, et al. "Extraordinary optical transmission through sub-wavelength hole arrays". *nature* 391, 667 (1998).

[74] J. A. Porto, F. J. Garcia-Vidal, and J. B. Pendry. "Transmission resonances on metallic gratings with very narrow slits". *Phys. Rev. Lett.* 83, 2845 (1999).

[75] P. N. Stavrinou and L. Solymar. "The propagation of electromagnetic power through subwavelength slits in a metallic grating". *Opt. Commun.* 206, 217 (2002).

[76] P. N. Stavrinou and L. Solymar. "Pulse delay and propagation through subwavelength metallic slits". *Phys. Rev. E* 68, 066604 (2003).

[77] M. Londoño, A. Sayanskiy, J. L. Araque-Quijano, et al. "Broadband huygens' metasurface based on hybrid resonances". *Phys. Rev. Appl.* 10, 034026 (2018).

[78] C. W. T. Chan and C. J Stevens. "Two-dimensional magneto-inductive wave data structures". *5th European Conference on Antennas and Propagation (EUCAP)* 1071 (2011).

[79] J. D. Baena, L. Jelinek, and R. Marqués. "Towards a systematic design of isotropic bulk magnetic metamaterials using the cubic point groups of symmetry". *Phys. Rev. B* 76, 245115 (2007).

[80] J. D. Baena, L. Jelinek, R. Marqués, et al. "Electrically small isotropic three-dimensional magnetic resonators for metamaterial design". *Appl. Phys. Lett.* 88, 134108 (2006).

[81] R. Marqués, L. Jelinek, M. J. Freire, et al. "Bulk metamaterials made of resonant rings". *Proc. of the IEEE* 99, 1660 (2011).

[82] J. D. Baena, L. Jelinek, R. Marqués, et al. "Isotropic frequency selective surfaces made of cubic resonators". *Appl. Phys. Lett.* 91, 191105 (2007).

[83] D. Popescu, A. Zapciu, C. Amza, et al. "FDM process parameters influence over the mechanical properties of polymer specimens: a review". *Polym. Test.* 69, 157 (2018).

[84] S. Zhang, C. C. Njoku, W. G. Whittow, et al. "Novel 3D printed synthetic dielectric substrates". *Microw. Opt. Technol. Lett.* 57, 2344 (2015).

[85] M. Pagac, J. Hajnys, Q. P. Ma, et al. "A Review of vat photopolymerization technology: materials, applications, challenges, and future trends of 3D printing". *Polymers* 13, 598 (2021).

[86] C. L. Liu, Q. Du, H. Zhou, et al. "Effect of the polystyrene particle size on dielectric and piezoelectric properties of PZT piezoelectric ceramics via vat photopolymerization (VPP)". *Addit. Manuf.* 78, 103857 (2023).

[87] A. Malas, D. Isakov, K. Couling, et al. "Fabrication of high permittivity resin composite for vat photopolymerization 3D printing: Morphology, thermal, dynamic mechanical and dielectric properties". *Materials* 12, 3818 (2019).

[88] Y. Zhang, G. Shi, J. Qin, et al. "Recent progress of direct ink writing of electronic components for advanced wearable devices". *ACS Appl. Electron. Mater.* 1, 1718 (2019).

[89] S. Kim, Y. Kawahara, A. Georgiadis, et al. "Low-cost inkjet-printed fully passive RFID tags using metamaterial-inspired antennas for capacitive sensing applications". *IEEE MTT-S International Microwave Symposium Digest (MTT)* 1 (2013).

[90] W. G. Whittow, A. Chauraya, J. C. Vardaxoglou, et al. "Inkjet-printed microstrip patch antennas realized on textile for wearable applications". *IEEE Antennas Wirel. Propag.* 13, 71 (2014).

[91] D. Jahn, R. Eckstein, L. M. Schneider, et al. "Digital aerosol jet printing for the fabrication of terahertz metamaterials". *Adv. Mater. Technol.* 3, 1700236 (2018).

[92] R. B. Kristiawan, F. Imaduddin, D. Ariawan, et al. "A review on the fused deposition modeling (FDM) 3D printing: filament processing, materials, and printing parameters". *Open Eng.* 11, 639 (2021).

[93] N. Zohdi, S. Tareq, and C. Yang. "Investigation on mechanical anisotropy of high impact polystyrene fabricated via fused deposition modelling". 4, 7 (2019).

[94] N. Chiotellis, S. Zhang, Y. C. Vardaxoglou, et al. "X wave radiator implemented with 3-D printed metamaterials". *IEEE Trans. Antennas Propag.* 68, 5478 (2020).

[95] P. Mahouti, M. A. Belen, F. Günes, et al. "Design and realization of multilayered cylindrical dielectric lens antenna using 3D printing technology". *Microw. Opt. Technol. Lett.* 61, 1400 (2019).

[96] Y. Wu, D. Isakov, and P. S. Grant. "Fabrication of composite filaments with high dielectric permittivity for fused deposition 3D printing". *Materials* 10, 1218 (2017).

[97] A. Vallecchi, C. J. Stevens, and E. Shamonina. "3D coupled resonators for enhanced filter design". *12th European Conference on Antennas and Propagation* 128 (2018).

[98] A. Vallecchi, A. Radkovskaya, L. Li, et al. "Superdirective dimers of coupled self-resonant split ring resonators: analytical modelling and numerical and experimental validation". *Sci. Rep.* 10, 274 (2020).

[99] S. Roy, M. B. Qureshi, S. Asif, et al. "A model for 3D-printed microstrip transmission lines using conductive electrifi filament". *IEEE International Symposium on Antennas and Propagation I& USNC/URSI National Radio Science Meeting* 1099 (2017).

[100] Y. Xie, S. Ye, C. Reyes, et al. "Microwave metamaterials made by fused deposition 3D printing of a highly conductive copper-based filament". *Appl. Phys. Lett.* 110, 181903 (2017).

[101] P. F. Flowers, C. Reyes, S. Ye, et al. "3D printing electronic components and circuits with conductive thermoplastic filament". *Addit. Manuf.* 18, 156 (2017).

[102] D. Mitra, R. Striker, J. Cleveland, et al. "A 3D printed microstrip patch antenna using electrifi filament for in-space manufacturing". *United States National Committee of URSI National Radio Science Meeting (USNC-URSI NRSM)* 216 (2021).

[103] S. Y. Wu, C. Yang, W. Hsu, et al. "3D-printed microelectronics for integrated circuitry and passive wireless sensors". *Microsyst. Nanoeng.* 1, 15013 (2015).

[104] V. T. Bharambe, J. Ma, M. D. Dickey, et al. "Planar, multifunctional 3D printed antennas using liquid metal parasitics". *IEEE Access* 7, 134245 (2019).

[105] G. L. Goh, S. Agarwala, and W. Y. Yong. "3D printing of microfludic sensor for soft robots: a preliminary study in design and fabrication". *Proceedings of the 2nd International Conference on Progress in Additive Manufacturing* 177 (2016).

[106] B. D. Wiltshire and M. H. Zarifi. "3-D printing microfluidic channels with embedded planar microwave resonators for RFID and liquid detection". *IEEE Microw. Wirel. Compon. Lett.* 29, 65 (2019).

[107] M. H. Too, K. F. Leong, C. K. Chua, et al. "Investigation of 3D non-random porous structures by fused deposition modelling". *Int. J. Adv. Manuf. Technol.* 19, 217 (2002).

[108] G. L. Goh, S. Agarwala, G. D. Goh, et al. "Additively manufactured multi-material free-form structure with printed electronics". *Int. J. Adv. Manuf. Technol.* 94, 1309 (2018).

[109] I. B. Corral, A. Bagheri, A. D. Fernández, et al. "Influence of infill and nozzle diameter on porosity of FDM printed parts with rectilinear grid pattern". *Procedia Manuf.* 41, 288 (2019).

[110] K. Y. Chan, X. Li, and R. Ramer. "Investigation of liquid metal and FDM 3D printed microwave devices". *International Semiconductor Conference* 93 (2018).

[111] Y. Z. Yu, J. R. Lu, and J. Liu. "3D printing for functional electronics by injection and package of liquid metals into channels of mechanical structures". *Mater. Des.* 122, 80 (2017).

[112] V. Bharambe, D. P. Parekh, C. Ladd, et al. "Vacuum-filling of liquid metals for 3D printed RF antennas". *Addit. Manuf.* 18, 221 (2017).

[113] C. Votzke, U. Daalkhaijav, Y. Mengüç, et al. "3D-printed liquid metal interconnects for stretchable electronics". *IEEE Sens. J.* 19, 3832 (2019).

[114] M. A. H. Khondoker, A. Ostashek, and D. Sameoto. "Direct 3D printing of stretchable circuits via liquid metal co-extrusion within thermoplastic filaments". *Adv. Eng. Mater.* 21, 1900060 (2019).

[115] T. V. Neumann and M. D. Dickey. "Liquid metal direct write and 3D printing: A review". *Adv. Mater. Technol.* 5, 2000070 (2020).

[116] A. Lipchitz, T. Imbert, and G. D. Harvel. "Investigation of fluid dynamic properties of liquid Field's metal". 56062, V002T11A008 (2013).

[117] A. Lipchitz, G. Harvel, and T. Sunagawa. "Thermophysical characteristics of liquid metal In-Bi-Sn eutectic (Field's metal) as a similarity coolant". *J. Nucl. Eng. Radiat.* 8, 031301 (2022).

[118] E. Sirjani, P. J. Cragg, and M. K. Dymond. "Glass transition temperatures, melting temperatures, water contact angles and dimensional precision of simple fused deposition model 3D prints and 3D printed channels constructed from a range of commercially available filaments". *Chem. Data Collect.* 22, 100244 (2019).

[119] C. A. Balanis. "Antenna theory: Analysis and design". *John Wiley & Sons,* New York, (2016).

[120] R. A. Serway and J. W. Jewett. "Physics for scientists and engineers". *Brooks Cole,* Los Angeles, (2010).

[121] A. Radkovskaya and E. Shamonina. "Band structures of mono-and diatomic metamaterials with inter-element coupling". *7th International Congress on Advanced Electromagnetic Materials in Microwaves and Optics*. Vol. 79. 2013.

[122] C. J. Stevens, I. Spanos, A. Vallechi, et al. "3D printing of functional metal and dielectric composite meta-atoms". *Small* 18, 2105368 (2022).

[123] M. Trojanowska-Tomczak, R. Steller, J. Janukiewicz, et al. “Conductive composites of PVC and wood’s metal with interpenetrating network structure”. *J. Appl. Polym. Sci.* 129, 3536 (2013).

[124] A. Mohammadi, T. L. Buckner, B. Yang, et al. “Effect of filler aspect ratio on stiffness and conductivity in phase-changing particulate composites”. *Adv. Mater. Technol.* 7, 2100920 (2022).

[125] N. Kazem, T. Hellebrekers, and C. Majidi. “Soft multifunctional composites and emulsions with liquid metals”. *Adv. Mater.* 29, 1605985 (2017).

[126] I. Spanos, C. J. Stevens, A. Vallechi, et al. “Fabricating 3D metamaterials via field’s metal Injection”. *21st Microwave Mediterranean Symposium (MMS)* 1 (2022).